Electrodeposition and Properties of Fe-Based Magnetic Alloys

A Thesis

Presented to

the faculty of the School of Engineering and Applied Science

University of Virginia

---

in partial fulfillment

of the requirements for the degree

Master of Science

by

Name

Siyuan Ge

Month degree is awarded August

Year 2015

APPROVAL SHEET

The thesis

is submitted in partial fulfillment of the requirements

for the degree of

Master of Science

Siyuan Ge

AUTHOR *signature*

The thesis has been read and approved by the examining committee:

Giovanni Zangari

Advisor

William C. Johnson

James T. Burns

Accepted for the School of Engineering and Applied Science:

James H. Aylor

Dean, School of Engineering and Applied Science

Month degree is awarded August

Year 2015

Print Form

Abstract

The goal of this work was to apply and extend a citrate-glycine complex of ferric ions based alkaline solution to generate a range of Fe-based alloy electrodeposits and nanostructures that could not be obtained otherwise. From a series of electrochemical experiments and characterization performed, electrolytes producing uniform Fe-based alloys with desired magnetic properties were achieved and reported. Systematic studies were carried out on binary (FeNi and FePt) and ternary (FeNiPt) iron group alloys relating their structure, magnetic properties with composition, thickness and annealing conditions.

Fabrication of $L1_0$-FePt nanodot arrays for bit patterned media (BPM) by electrodeposition from an alkaline solution was described, with an ultimate goal to achieve isolated bits of size ~10nm. In this thesis, a nanoimprinting technique was employed to form patterned substrate with 150nm pitch by collaborating with colleagues at Waseda University, Japan. Deposition and annealing conditions for FePt nanopatterns were studied and optimized. In particular, a patterned $Fe_{48}Pt_{52}$ (55nm) with a high coercivity of around 8.2kOe was formed by electrodeposition with subsequent heat treatment, demonstrating the capability of electrochemical processes to produce high performance FePt ferromagnetic nanodot arrays.

Electrodeposition of Fe-Ni-Pt thin films for applications in heat-assisted magnetic recording (HAMR) was also studied. An electrolyte based on the citrate-glycine complexes of ferric ions for the deposition process was investigated and optimized to generate a series of homogeneous $Fe_xNi_{50-x}Pt_{50}$ ($0<x<30$) thin films. Anomalous deposition phenomenon was observed and described for different deposition baths. Magnetic properties dependence on Ni content and annealing temperatures were analyzed and discussed. We reported a $Fe_{42}Ni_{12}Pt_{46}$ thin film with a coercivity of 8.8kOe after annealing at 700^{o}C and its temperature dependence of magnetic properties, which turned out to be suitable for the writing performance of recording media.

As a soft magnetic material, permalloy ($Fe_{19}Ni_{81}$) found many applications in areas such as magnetic recording heads or magnetic field sensors. Electrodeposition from an alkaline solution was applied for the first time to obtain permalloy or Pt-doped permalloy thin film alloys with coercivities lower than 10Oe. Pt addition to the permalloy is expected to enhance the damping effect and fasten magnetization switching, resulting in higher speed or data rates for the magnetic recording. The anomalous deposition phenomenon was observed and discussed. From the same solution, equiatomic FeNi thin films were also obtained, followed by heat treatment to explore the possibility to form tetragonal $L1_0$-FeNi in laboratory conditions.

Acknowledgement

I would first like to thank my advisor, Dr. Giovanni Zangari, for sharing his knowledge, experience and scientific mind, introducing me to the research area of magnetic materials and electrodeposition, as well as providing support and guidance throughout these years. I am deeply grateful for all the patience and opportunities he has given me.

I would also like to acknowledge continuous help and advice from Richard White and Michal Sabat at the Nanoscale Materials Characterization Facility (NMCF), VSM maintenance from Barry Baber (MSE) as well as all the faculty members and students in the Center for Electrochemical Science and Engineering (CESE) and the department. In particular, discussions with Dr. Soffa in the area of magnetism are greatly appreciated.

The financial support from National Science Foundation through Grant No. 1207351 and prepatterned substrates provided by Professor Homma's group at Waseda University are gratefully acknowledged; both made all the projects and thesis possible. And I am thankful to my dissertation committee members Dr. William Johnson and Dr. James Burns for their time, help and all the effort.

Most of all, I would like to thank my parents Mr. Zongfa Ge and Mrs. Xiaojuan Huang for all the love and inspiration. No matter what kind of decision I made, you have always fully supported me and motivated me. This thesis would never be possible without you two being the source of tremendous encouragement.

Also I would like to thank my friends for sharing smiles and happy moments when times were good and joyful, as well as providing deep listening and suggestion when times seemed to be rough and hard. In particular, thanks to Yuhan, Xiaoyu, Zhao and Xiaopu for making my time here enjoyable and full of memories.

Finally, I would like to thank all the members in our group, especially Lok-kun, who I can always discuss with and helped solve numerous small problems in my research.

Table of Contents

Abstract .... **i**

Acknowledgements .... **iii**

Table of Contents .... **v**

List of Tables... **viii**

List of Figures... **x**

List of Symbols……………………………………………………………………………... **xix**

1 Introduction **1**

1.1. Electrodeposition…... 1

1.1.1. Electrode potential…... 1

1.1.2. Electrochemical cell………………………………………………………... 3

1.1.3. Kinetics and mechanism of electrodeposition….. 5

1.1.4. Understanding electrodeposition at atomic level... 9

1.1.5. Electrodeposition of alloys.. 12

1.2. Magnetic materials and magnetism…... 15

1.2.1. Introduction to magnetism….. 15

1.2.2. Magnetic Anisotropy.. 21

1.2.3. Basics of magnetic recording…... 23

1.2.4. Longitudinal recording and perpendicular recording………………………….. 25

1.2.5. Magnetic materials for recording media….. 28

1.2.6. Bit patterned media and heat-assisted magnetic recording media…................. 29

1.2.7. History and properties of permanent magnet…………………………............32

1.3. Thin film characterization techniques…... 33

1.3.1. X-ray diffraction…... 33

1.3.2. Vibrating Sample Magnetometer.. 35

1.3.3. Scanning Electron Microscopy.. 36

1.3.4. Surface analysis…... 39

1.4. Overview of bit-patterned media (BPM) and recent research in FePt nanodots............ 42

1.5. Overview of HAMR technology and recent research in FeNiPt................................... 46

1.6. Overview of electrodeposited permalloy and Pt-doped permalloy……………………. 48

1.7. Overview of recent research in rare-earth free $L1_0$-FeNi alloys……………………….. 49

2. The experimental set-up………………………………………………………………….. 55

2.1. Preparation of pre-patterned substrates for FePt nanodot arrays………………………. 55

2.2. Sample preparation for electrodeposition……………………………………………… 56

2.3. Three-electrode setup: vertical and parallel…………………………………………… 57

2.4. Preparation of $Pt(NH_3)_2(NO_2)_2$, known as Pt-p-salt…………………………………… 58

2.5. Solutions for electrodeposition: FePt nanodot arrays, Ni-doped FePt, permalloy & equiatomic FeNi and Pt-doped FeNi…………………………………………………... 60

2.5.1. Solution for electrodeposited FePt nanodot arrays…………………………... 60

2.5.2. Solution development for electrodeposition of Ni-doped FePt……………… 61

2.5.3. Solution for electrodeposition of permally and equiatomic FeNi…………… 61

2.5.4. Solution for electrodeposition of Pt-doped permalloy………………………. 61

2.6. Characterization methods……………………………………………………………… 62

3. Synthesis and characterization of FePt nanodot arrays for BPM.................................. 63

3.1. Characterization of $Fe_{45}Pt_{55}$ nanodot arrays with a height of 80nm…………………... 63

3.2. Deposition of FePt nanodot arrays for a short time.. 74

3.3. Deposition of FePt nanodot arrays for a long time.. 82

4. Synthesis and characterization of FeNiPt alloy for potential application in HAMR....... 97

4.1. Electrolyte exploration for FeNiPt deposition.. 97

4.2. Structure and magnetic properties of $Fe_{50-x}Ni_xPt_{50}$ thin films...................................... 111

5. Electrodeposition and magnetic properties of FeNi/FeNiPt alloys (high permeability permalloy, Pt-doped permalloy and equatomic FeNi).. 133

4.1. Experimental design and preliminary results for $Fe_{19}Ni_{81}$ and Pt-doped $Fe_{19}Ni_{81}$....... 133

4.2. Properties of equiatomic FeNi... 141

6. Conclusion………………………………………………………………………………151

References……………………………………………………………………………….. 153

List of Tables

Table 1.1 Common magnetic terms, units and conversion factor……………………………….19

Table 1.2 Comparison of magnetic materials with high anisotropy…………………………….29

Table 2.1 Recipe of FePt plating bath……………………………………………………...60

Table 2.2 Make-up of the Fe-Ni electrolyte…………………………………………………..61

Table 3.1 Three FePt nanodot array samples deposited at -1.39V vs. MSE with varying deposition time……………………………………………………………...…………75

Table 3.2 Properties of FePt nanodot arrays with different heights……………………………..81

Table 3.3 Properties of FePt nanodot arrays (sample E1 and E2) with different heights……….82

Table 3.4 Deposition conditions, composition and thickness of two FePt nanodot arrays (sample D1 and D2)………………………………………………………………………………….90

Table 4.1 Make-up of the Fe-Ni-Pt electrolyte (Pt-p-salt: 10mM)…………………………...97

Table 4.2 Deposition conditions for films with a composition of Fe50-xNixPt50 (0<x<30)….101

Table 4.3 Make-up of the Fe-Ni-Pt electrolyte (Pt-p-salt: 15mM)…………………………….105

Table 4.4 Make-up of the Fe-Ni-Pt electrolyte (Pt-p-salt: 15mM, $NiSO_4$: 15mM, $Fe_2(SO_4)_3$: 5, 10, 15, 20mM)……………………………………………………………………………..106

Table 4.5 Comparison of FeNiPt films depositied at various potentials from different solution…………………………………………………………………………………….107

Table 4.6 Make-up of the Fe-Ni-Pt electrolyte (Pt-p-salt: 15mM, $NiSO_4$: 15mM, $Fe_2(SO_4)_3$: 25, 30)……………………………………………………………………………………108

Table 4.7 Composition of FeNiPt films deposited at various potentials from solution with 30mM ferric sulfate……………………………………………………………………………….109

Table 4.8 Lattice parameters of $Fe_{27}Ni_{20}Pt_{53}$ (100nm) after annealing at 450°C, 550°C and 650°C for 1h……………………………………………………………………………………113

Table 4.9 Comparison of lattice parameter from fcc(111) peak in XRD with that from Vegard's law………………………………………………………………………………………122

Table 4.10 Composition influence on the magnetic properties of FeNiPt thin films………......123

Table 4.11 Deposition conditions for FeNiPt thin films with a thickness of 80nm……………124

Table 4.12 Oxygen content in the FeNiPt thin films with a thickness of 80nm……………….125

Table 4.13 Comparison of properties of FeNiPt thin films with a thickness of 80nm…………126

Table 5.1 Characterization of Pt-doped permalloy deposited from -1.45V~-1.54V…………...137

Table 5.2 Comparison of three FeNi thin film samples………………………………………..142

Table 5.3 As-deposited FeNi with a deposition time of 45min………………………………..142

List of Figures

Figure 1.1 Formation of metal-solution interphase……………………………………..……......2

Figure 1.2 Measurement of electrode potential of zinc electrode (Zn^{2+}/Zn). ……………………3

Figure 1.3 Schematic view of the commercially two-electrode setup in an electrochemical cell (extracted from Metrohm Autolab Application Note)…………………………………………4

Figure 1.4 Schematic view of the three-electrode setup (extracted from Metrohm Autolab Application Note)……………………………………………………………………………….5

Figure 1.5 Variation of the concentration of the reactant during non-steady-state electrolysis…………………..……………………………………………………………….8

Figure 1.6 Schematic representation of the structure of a water molecule, shown as dipole…...10

Figure 1.7 Schematics of the electrodeposition process……………………………………...11

Figure 1.8 An ideal polarization curve for the electrodeposition of the binary alloy results from the sum of pure metal (A and B) polarization curves…………………………………………13

Figure 1.9 Illustration of diamagnetic behavior: magnetic response to an external field………16

Figure 1.10 Alignment of magnetic moments in paramagnetic materials (i.e., Na, Al) with and without an external field………………………………………………………………………17

Figure 1.11 Alignment of magnetic moments in ferromagnetic materials with and without an external field……………………………………………………………………………..…18

Figure 1.12 Magnetic hysteresis loop for a ferromagnet: magnetization M as a function of the magnetic field strength H……………………………………………………………………...19

Figure 1.13 Ferrimagnetism……………………………………………………………..20

Figure 1.14 A comparison of different types of magnetism…………………………………….21

Figure 1.15 Mixed Anisotropy………………………………………………………….…….23

Figure 1.16 Top view of a 36 GB, 10,000 RPM, IBM SCSI server hard disk, with its top cover removed. (The IBM Ultrastar 36ZX)……………………………………………………………..24

Figure 1.17 A schematic of a longitudinal magnetic recording system (left) and a typical longitudinal recording head (right)……………………………………………………………26

Figure 1.18 Schematic diagram of a perpendicular recording system and a perpendicular recording head……………………………………………………………………………28

Figure 1.19 Diagram indicating the increase of recording density…………………………...…30

Figure 1.20 Concept of bit patterned media (image via nist.gov)………………………………31

Figure 1.21 A sketch illustrating the HAMR writing process…………………………………..32

Figure 1.22 (BH)$_{max}$ as a function of the average selling price per kilogram for the four major commercial magnets in US, 2012…………………………………………………………..33

Figure 1.23 Bragg-Brentano geometry of an x-ray diffractometer……………………………...35

Figure 1.24 Schematic of a vibrating sample magnetometer……………………………………36

Figure 1.25 Signals generated from electron beam – specimen interactions……………………37

Figure 1.26 The amount of secondary electrons generated depends on the surface…………….38

Figure 1.27 Drawing of the basic principle of Atomic Force Microscopy (AFM)……………...40

Figure 1.28 Images of a continuous medium with an average grain pitch of 5.5nm (left); a bit-patterned medium with a dot pitch of 13nm (right)…………………………………………43

Figure 1.29 Fe-Pt phase diagram……………………………………………………………..45

Figure 1.30 Crystal structures of fcc and fct phase FePt (ball-and-stick models, source: University of Alabama……………………………………………………………………...45

Figure 1.31 A Fe-Ni-Pt ternary phase diagrams at 600°C, the L1$_0$ stable regions are marked….48

Figure 1.32 Left: Fe-Ni phase diagram calculated by Cacciamani and Dinsdale in 2009; right: Fe-Ni phase diagram provided by Reuter et al. (1989)………………………………………..54

Figure 2.1 Fabrication process of a pre-patterned substrate……………………………………55

Figure 2.2 (a) different geometries of a working electrode; (b) detailed drawing of a working electrode used in this thesis…………………………………………………………………56

Figure 2.3 The vertical configuration of three-electrode setup for FePt electrodeposition……..58

Figure 2.4 The parallel configuration of three-electrode setup…………………………………58

Figure 2.5 A commercial jacket beaker with a volume of 250mL……………………………...59

Figure 3.1 Plan-view SEM images of FePt sample D (as-deposited, 450^{o}C, 650^{o}C) at 30kX….63

Figure 3.2 Plan-view SEM images of FePt sample D (as-deposited, 450^{o}C, 650^{o}C) at 50kX.…63

Figure 3.3 Cross-sectional SEM images of FePt sample D after 650^{o}C annealing....………..…64

Figure 3.4 AFM image of sample $Fe_{45}Pt_{55}$ after 650^{o}C annealing for 1h (courtsey of Marcel Mibus)…………………………………………………………………………………65

Figure 3.5 Hysteresis loops of as-deposited $Fe_{45}Pt_{55}$ patterned sample………………………66

Figure 3.6 Hysteresis loops of $Fe_{45}Pt_{55}$ nanodot arrays after 450^{o}C annealing……..…………..66

Figure 3.7 Hysteresis loops of $Fe_{45}Pt_{55}$ nanodot arrays after 550^{o}C annealing………..………..67

Figure 3.8 Hysteresis loops of $Fe_{45}Pt_{55}$ nanodot arrays after 650^{o}C annealing…………………67

Figure 3.9 Hysteresis loops for patterned $Fe_{45}Pt_{55}$ in the in-plane direction at different temperatures...…………………………………………………………………………68

Figure 3.10 Hysteresis loops for patterned $Fe_{45}Pt_{55}$ in the out-of-plane directions at different temperatures……………………………………………………………………..……….69

Figure 3.11 XRD pattern for as-deposited and annealed $Fe_{45}Pt_{55}$ nanodot arrays...…………….70

Figure 3.12 Mr/Ms of $Fe_{45}Pt_{55}$ at different annealing temperatures in both in-plane and out-of-plane directions…………………………………………………………….……………..71

Figure 3. 13 Hysteresis loops for $Fe_{45}Pt_{55}$ nanodot arrays at various angles……………………71

Figure 3. 14 Normalized hysteresis loops for $Fe_{45}Pt_{55}$ nanodot arrays at various angles…...…..72

Figure 3. 15 Detailed view of the first quadrant part of selected hysteresis loops of $Fe_{45}Pt_{55}$ nanodot arrays at different angles φ……………………………………………………………...73

Figure 3. 16 Angular variation of the magnetization at remanence compared with [Mr(0)/Ms]cos φ………………………………………………………………………………………………74

Figure 3. 17 Cross-section image of FePt nanodot arrays (sample 8b: $Fe_{52}Pt_{48}$)...……………...75

Figure 3. 18 Tilted SEM images of FePt samples with a magnefication of 20kx………………76

Figure 3. 19 XRD pattern for $Fe_{52}Pt_{48}$ patterned arrays before and after 650°C annealing….......76

Figure 3. 20 Original hysteresis loop for $Fe_{52}Pt_{48}$ patterned arrays after 650°C annealing….......77

Figure 3. 21 Hysteresis loop for $Fe_{52}Pt_{48}$ patterned arrays after 650°C annealing………………78

Figure 3. 22 XRD pattern for $Fe_{52}Pt_{48}$ patterned arrays before and after 650°C annealing….......79

Figure 3. 23 Hysteresis loop for $Fe_{51}Pt_{49}$ patterned arrays after 650°C annealing………………80

Figure 3. 24 XRD pattern for $Fe_{51}Pt_{49}$ patterned arrays before and after 650°C annealing….......80

Figure 3. 25 Hysteresis loop for $Fe_{51}Pt_{49}$ patterned arrays after 650°C annealing……………....81

Figure 3. 26 Plain view of as-deposited patterned FePt samples (E1 and E2)………………….83

Figure 3. 27 Plain view and 45° tilted SEM images of 400°C annealed samples…………...…..83

Figure 3. 28 Plain view and 45° tilted SEM images of 750°C annealed samples…………….…83

Figure 3. 29 XRD pattern for as-deposited and annealed FePt sample E1……………………...84

Figure 3. 30 Hysteresis loops for as-deposited and annealed FePt sample E1………………….85

Figure 3. 31 Dependence of Hc on the annealing temperature for FePt sample E1…………….87

Figure 3. 32 XRD pattern for as-deposited and annealed FePt sample E2……………………...88

Figure 3. 33 Hysteresis loops for as-deposited and annealed FePt sample E2…….……………89

Figure 3. 34 Plain view of as-deposited FePt sample D1 with a magnefication of 20kx (insert is a 100kx)……………………………………………………………………………………91

Figure 3. 35 Plain view of as-deposited FePt sample D2 with a magnefication of 20kx (insert is a 100kx)……………………………………………………………………………………91

Figure 3. 36 Current density vs. deposition time for FePt sampe D1 and D2…………………..92

Figure 3. 37 SEM image (left) and tilted SEM image (right, tilt angle 60o) of 800^{o}C annealed Fe46Pt54…………………………………………………………………………………92

Figure 3. 38 XRD pattern for sample $Fe_{46}Pt_{54}$ before and after 850^{o}C annealing……….……...93

Figure 3. 39 Hysteresis loops for sample $Fe_{46}Pt_{54}$ before and after 850^{o}C annealing…….……94

Figure 3. 40 SEM image (left) and tilted SEM image (right, tilt angle 60^{o}) of 800^{o}C annealed $Fe_{48}Pt_{52}$ (D2)………………………………………………………………………..94

Figure 3. 41 Mapping of patterned $Fe_{48}Pt_{52}$…………………………………………….....95

Figure 3. 42 XRD pattern for sample $Fe_{48}Pt_{52}$ before and after 850^{o}C annealing…………..…...95

Figure 3. 43 Hysteresis loops for sample $Fe_{48}Pt_{52}$ before and after 850^{o}C annealing……….….96

Figure 4. 1 Composition vs. potential for FeNiPt alloy thin films deposited from solutions with 2mM $NiSO_4$……………………………………………………………………………...98

Figure 4. 2 Composition vs. potential for FeNiPt alloy thin films deposited from solutions with various $NiSO_4$ concentrations……………………………………………………………...99

Figure 4. 3 Growth rate of $Fe_{25}Ni_{25}Pt_{50}$ thin film on the Ni^{2+} concentration in electrolytes……………………………………………………………………………...101

Figure 4. 4 Dependence of (Ni + Pt)/Fe ratio in deposited films on the Ni^{2+} concentration and applied potentials in electrolytes……………….……………………………………………….102

Figure 4. 5 Comparison of the (Fe/Ni) in electrolyte and that in the as-deposited films………103

Figure 4. 6 Composition vs. potential for FeNiPt alloy thin films (Pt-p-salt: 15mM, $NiSO_4$: 5, 10, 15, 25mM)……………………………………………………………………………………105

Figure 4. 7 Composition vs. potential for FeNiPt alloy (Pt-p-salt: 15mM; $NiSO_4$: 15mM, ferric sulfate: 5, 10, 15, 20mM)……………………………………………………………………….107

Figure 4. 8 Composition of films deposited at various potentials from solutions with 25mM and 30mM Ferric sulfate…………………………………………………………………………….109

Figure 4. 9 Comparison of the (Fe/Ni) in electrolyte with that in the as-deposited films……..110

Figure 4. 10 Magnetization decreases with the increase of Ni content in 10nm FeNiPt films...111

Figure 4. 11 Coercivity dependence on the Ni content in 10nm FeNiPt films………………...112

Figure 4. 12 XRD pattern of 100nm $Fe_{27}Ni_{20}Pt_{53}$ before and after annealing…………………113

Figure 4. 13 Hysteresis loops of 100nm $Fe_{27}Ni_{20}Pt_{53}$ in in-plane direction before and after annealing……………………………………………………………………………………..114

Figure 4. 14 Hysteresis loops of 100nm $Fe_{27}Ni_{20}Pt_{53}$ in out-of-plane direction before and after annealing…………………………………………………………………….………….114

Figure 4. 15 Thickness of FeNiPt films under investigation of SEM………………………….116

Figure 4. 16 Left: XRD (before/after 650°C, 1h); right: Hysteresis loops for film $Fe_{38}Ni_{7}Pt_{55}$ after 650°C annealing…………………………………………………………………………...116

Figure 4. 17 Left: XRD (before/after 650°C, 1h); right: Hysteresis loops for film $Fe_{38}Ni_{8}Pt_{54}$ after 650°C annealing…………………………………………………………………………...117

Figure 4. 18 Left: XRD (before/after 650ºC, 1h); right: Hysteresis loops for film $Fe_{39}Ni_{11}Pt_{50}$ after 650ºC annealing……………………..……………………………………………………117

Figure 4. 19 XRD for film $Fe_{39}Ni_{12}Pt_{49}$ before/after 650ºC, 1h…………………..…………...118

Figure 4. 20 Hysteresis loops of film $Fe_{39}Ni_{12}Pt_{49}$ measured after 650ºC annealing (left) and 700ºC annealing (right)…………………...……………………………………………………….118

Figure 4. 21 Left: XRD (before/after 650ºC, 1h); right: Hysteresis loops for film $Fe_{40}Ni_{13}Pt_{47}$ after 650ºC annealing……………………..……………………………………………………119

Figure 4. 22 Left: XRD (before/after 650ºC, 1h); right: Hysteresis loops for film $Fe_{43}Ni_{13}Pt_{44}$ after 650ºC annealing…………………………………………………………………………...120

Figure 4. 23 XRD for film $Fe_{42}Ni_{12}Pt_{46}$ before and after 650ºC annealing…………………....121

Figure 4. 24 Hysteresis loops for film $Fe_{42}Ni_{12}Pt_{46}$ after 650ºC annealing for 1h (left); 700ºC annealing for 1h (right)……………………………………………………………………………121

Figure 4. 25 Relationship between Fe/Pt ratio and coercivity in FeNiPt films..………………124

Figure 4. 26 Deposition rate for a set of FeNiPt deposition…………………………………...125

Figure 4. 27 SEI images of the same series of FeNiPt thin films which show relatively low porosity…………………………………………………………………………………………125

Figure 4. 28 XRD for as-deposited/650ºC/700ºC annealed $Fe_{30}Ni_{8}Pt_{62}$ film (left); film thickness measured by profilometer (right)……………………………………………………………….126

Figure 4. 29 Cross-sectional SEM images of four distinct FeNiPt films showing compact morphology and verifying the film thicknesses……………………………………………...127

Figure 4. 30 Hysteresis loops for film $Fe_{30}Ni_{8}Pt_{62}$ after 650ºC and 700ºC annealing, respectively……………………………………………………………………………………..127

Figure 4. 31 XRD for as-deposited/650ºC/700ºC annealed $Fe_{32}Ni_{11}Pt_{57}$ film (left); film thickness measured by profilometer (right)……………………………………………………………….128

Figure 4. 32 Hysteresis loops for film $Fe_{32}Ni_{11}Pt_{57}$ after 650ºC and 700ºC annealing, respectively……………………………………………………………………………………..128

Figure 4. 33 XRD for as-deposited/650ºC/700ºC annealed $Fe_{30}Ni_{13}Pt_{57}$ film (left); film thickness measured by profilometer (right)……………………………………………………………….128

Figure 4. 34 Hysteresis loops for film $Fe_{30}Ni_{13}Pt_{57}$ after 650ºC and 700ºC annealing, respectively……………………………………………………………………………………..129

Figure 4. 35 XRD for as-deposited/650ºC/700ºC annealed $Fe_{39}Ni_{11}Pt_{50}$ film (left); film thickness measured by profilometer (right)……………………………………………………………….129

Figure 4. 36 Hysteresis loops for film $Fe_{39}Ni_{11}Pt_{50}$ after 650°C and 700°C annealing, respectively……………………………………………………………………………..129

Figure 4. 37 Coercivity dependence on Fe/Pt ratio given Ni content is roughly around 10%...130

Figure 4. 38 XRD patterns for FeNiPt thin film annealed at 700°C for 1h……………...…….131

Figure 4. 39 M-H loops for $Fe_{39}Ni_{11}Pt_{50}$ (80nm) at different temperatures (courtsey of Linqiang Luo)……………………………………………………………………………………..132

Figure 4. 40 Temperature dependence of normalized magnetization and coercivity for $Fe_{39}Ni_{11}Pt_{50}$ with our group (left), $[Fe(0.38nm)/Ni(0.04nm)/Pt(0.4nm)]_{13}$ from Yan et al (right)……………………………………………………………………………...………132

Figure 5. 1 Composition of FeNi alloys for solutions with varying Ni^{2+}/Fe^{3+}……….……….133

Figure 5. 2 Comparison of the (Ni/Fe) in electrolyte and that in the as-deposited films…..….134

Figure 5. 3 Composition of Pt-doped permalloy from solution: 4mM Fe^{3+}+64mM Ni^{2+}+1mM Pt-p-salt…………………………………………………………………..………………..135

Figure 5. 4 Composition dependence of Pt-doped permalloy on deposition time when applied potential is -1.6 V vs. MSE……………………………....………………………………136

Figure 5. 5 Composition of Pt-doped permalloy films deposited from a cell with parallel configuration…………………………………………………………………………………136

Figure 5. 6 Deposition rate for Pt-doped permalloy films within the deposition potential range (-1.45~-1.54V vs. MSE)…………………………………………………………….….137

Figure 5. 7 Magnetization curves for Pt-doped permalloy deposited at -1.54V……………….138

Figure 5. 8 Magnetization curves for Pt-doped permalloy deposited at -1.53V……………….139

Figure 5. 9 Magnetization curves for Pt-doped permalloy deposited at -1.52V……………….139

Figure 5. 10 Magnetization curves for Pt-doped permalloy deposited at -1.47V…...…………140

Figure 5. 11 Magnetization curves for Pt-doped permalloy deposited at -1.45V………...……140

Figure 5. 12 FeNi and FeNiPt deposition from a parallel cell configuration……………..…….141

Figure 5. 13 Composition dependence on applied potential for FeNi electrodeposition………142

Figure 5. 14 Cross-section images for the as-deposited FeNi samples………………………...143

Figure 5. 15 XRD patterns for three as-deposited FeNi thin films…......……………………..144

Figure 5. 16 XRD patterns for three FeNi thin films annealed at 400°C for 1h………………..……………………………………………………………………….…...…144

Figure 5. 17 VSM for $Fe_{49}Ni_{51}$ deposited at -1.440V vs. MSE………………………...……145

Figure 5. 18 VSM for $Fe_{49}Ni_{51}$ deposited at -1.443V vs. MSE……………………………..…145

Figure 5. 19 VSM for $Fe_{55}Ni_{45}$ deposited at -1.446V vs. MSE ……………………………….146

Figure 5. 20 Cross-section of $Fe_{49}Ni_{51}$ sample under SEM…………………………...…….146

Figure 5. 21 Magnetization curves for as-deposited $Fe_{49}Ni_{51}$ with different applied field ranges (left: -20kOe~20kOe, right: 4kOe~4kOe)…………………………...…………………….147

Figure 5. 22 Magnetization curves for as-deposited $Fe_{55}Ni_{49}$ (left) and $Fe_{56}Ni_{44}$ (right) thin films with applied field: -4kOe~4kOe …………………………………………...…….…….147

Figure 5. 23 XRD patterns for the as-deposited FeNi thin films with a thickness of 500nm…………………………………………………………………………….…….148

Figure 5. 24 XRD patterns for $Fe_{51}Ni_{49}$ before and after annealing at different temperatures ……………………………………………………...…………….…….148

Figure 5. 25 In-plane magnetization curves before and after annealing…………...….…….149

Figure 5. 26 Out-of-plane magnetization curves before and after annealing…………….…….150

List of Symbols

ad-atoms	adsorbed atom
a_{H}^{+}	activity of hydrogen ion
ARC	anti-reflective coating
B	magnetic induction or bit length
BPM	bit-patterned media
C_{H}^{+}	concentration of hydrogen ion
CE	counter electrode
D	diffusion coefficient or the grain size
dB	decibel
D_{ch}	density of channel
E	anisotropy energy
E^{o}_{zn}	standard electrode potential of Zinc
F	Faraday's constant (96480C)
FCC	face centered cubic
FCT	face centered tetragonal
G	gauss, unit of magnetic induction
H	applied magnetic field
HAMR	heat-assisted magnetic recording
H_c	coercivity
HDD	hard drive disk
H_k	the anisotropy field
i	current density
i_L	limiting current density
K_u	uniaxial magnetic anisotropy energy
LC	luggin capillary
M	metal or magnetization
m	magnetic moment
M_r	remanence
Ms	saturation magnetization
NHE	normal hydrogen electrode
OCP	open circuit potential
Oe	oersted, unit of magnetic field
R	gas constant: 8.3143 J/k/mol
RE	reference electrode
S	surface area of the electrode
SHE	standard hydrogen electrode
SNR	signal-to-noise
T	temperature
Tc	Curie temperature
UV-NIL	UV nanoimprint lithography
V	the grain volume
WE	working electrode
Z	atomic number
γ	domain wall energy

δ	thickness of the diffusion layer
δ_w	domain wall width
η	overpotential or backscattered yield
χ	susceptibility
$(BH)_{max}$	maximum energy product

1. Introduction

1.1. Electrodeposition

1.1.1. Electrode potential

A metal M consists essentically of metallic ions (M^{z+}) located at lattice sites and the valence electrons that bind them together. When such metal is immersed in an aqueous solution of its own salt, there will be an exchange of the ion M^{z+} at the metal-solution interface. One of two processes may occur: either more M^{z+} ions leave the crystal lattice of the metal to the solution, resulting in a negatively charged metal (Eq. 1.1), or more M^{z+} ions in the solution adsorb on the metal electrode, making the metal positively charged (Eq. 1.2):

$$M -> M^{z+} + ze^{-} \quad \text{(Oxidation, loss of electrons)} \qquad \textbf{Eq. 1. 1}$$

$$M^{Z+} + ze^{-} -> M \quad \text{(Reduction, gain of electrons)} \qquad \textbf{Eq. 1. 2}$$

where z is the number of electrons involved in the reaction.

As a consequence, a potential difference is set up between the metal and the solution, and this persists as long as the charge is allowed to remain on the metal; this typically occurs at open circuit. After a certain period of time, a dynamic equilibrium is established within the system:

$$M^{Z+} + ze^{-} \Leftrightarrow M \qquad \textbf{Eq. 1. 3}$$

with the number of M^{z+} ions entering the crystal lattice, and the number of M^{z+} ions leaving the crystal lattice per unit time becoming equal (see **Fig. 1.1**):

$$\overrightarrow{n} = \overleftarrow{n} \qquad \textbf{Eq. 1. 4}$$

At equilibrium, the potential difference between the metal and solution becomes a constant value, which measures of the tendency of a metallic electrode to lose or gain electrons.

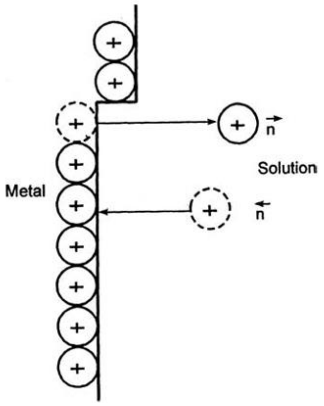

Figure 1. 1 Formation of metal-solution interphase; equilibrium state[8]: $\vec{n} = \overleftarrow{n}$

The above quantity is not yet the electrode potential. In order to measure the value of a single electrode potential (potential difference between the metal and the surrounding solution of its own salt), one must connect the electrode under study to another electrode and thus form an electrochemical cell. In other words, it is impossible to measure the absolute value of a single electrode potential, but one can determine its relative value by using a standard hydrogen electrode (SHE, E=0.000V, a_{H^+}=1) or normal hydrogen electrode (NHE, E ≈ 0.000V, C_{H^+}=1) as a reference.

For example, coupling a Zn electrode (dipped in 1M $ZnSO_4$) with SHE, the resulting voltmeter reading would directly give the value of the Zn electrode potential (**Fig. 1.2**). In this case, the zinc electrode acts as anode, so the measured value, 0.76V is its oxidation potential. This means that the reduction potential of a zinc electrode is -0.76V, which is called the standard electrode potential of Zinc (denoted E^0_{zn}). The standard electrode potential of other electrodes can be obtained in a similar way.

We now consider the potential of the M^{z+}/M electrode as a function of the activity of metallic ions in the solution, according to the Nernst equation:

$$E = E^0 + \frac{RT}{zF} \ln a(M^{z+}) \qquad \text{Eq 1. 5}$$

Where R, T, F are the gas constant (8.3143 J/k/mol), absolute temperature (K) and Faraday's constant (96480 C), z the valence change in the redox reaction, and *a* the activity of the metallic ions, respectively. When the activity of M^{Z+} in the solution is equal to 1, then, $E = E^0$.

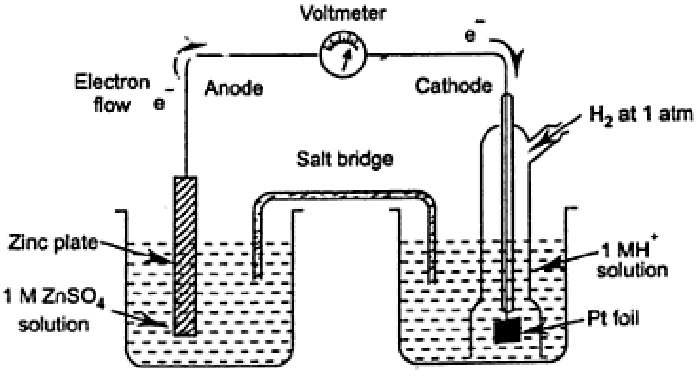

Figure 1. 2 Measurement of electrode potential of zinc electrode (Zn2+/Zn). Here Zn electrode acts as anode, so electrode potential of Zn is given a negative sign. Figure extracted from "Engineering Chemistry"[1]

If numerical values are substituted for R and F, T is fixed at 298K, and base 10 logarithm is used instead of base e, the Nernst equation can be expressed (in Volt) as:

$$E = E^0 + \frac{0.059}{n} \ln a(M^{z+}) \qquad \text{Eq 1. 6}$$

1.1.2. Electrochemical cell

The electrochemical cell in an electrodeposition experiment usually consists of two or three electrodes, with the most basic form of the cell being the two-electrode setup (**Fig 1.3**). In a cell with a two-electrode arrangement, the electrode under investigation is called the working electrode (WE), and the electrode needed to close the electrical circuit is the counter electrode (CE). In this configuration, only the overall cell voltage can be monitored; this includes the contributions from the CE/electrolyte interface and the electrolyte itself (potential drop: iR) in addition to that from the WE/electrolyte and does not allow to monitor the voltage drop at the WE interface. The two-electrode configuration is therefore used when precise control of the potential drop across WE electrochemical interface is not critical and the behavior of the whole cell is under study. For example, it can be used to investigate electrolyte properties such as the conductivity.

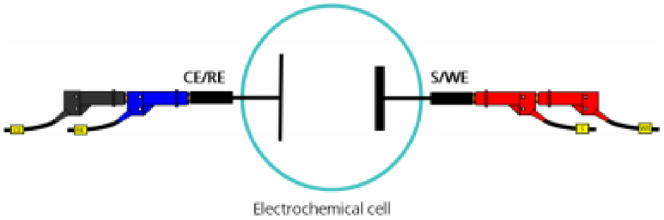

Figure 1. 3 Schematic view of the commercially two-electrode setup in an electrochemical cell. To avoid ohmic losses in high current applications, it is recommended to connect the Sense (S) and reference electrode (RE) leads directly to the cell, as indicated above[2].

When electrodeposition processes are performed, usually the experimenter is only interested in the reactions taking place at the working electrode. To have precise control of the potential across the WE/electrolyte or under conditions when electrolyte contains poorly conducting organic solvents where iR drop is considerable, a three-electrode setup is used. A typical three-electrode cell is shown in **Fig 1.4**. In this case, the current flows between the CE and the WE. A third electrode (the reference electrode, RE) is kept in close proximity of the WE by using a Luggin capillary (LC), and used to determine the potential across the electrochemical interface accurately. Since a negligible current is drawn through the reference electrode, a constant potential value of the reference electrode can be maintained.

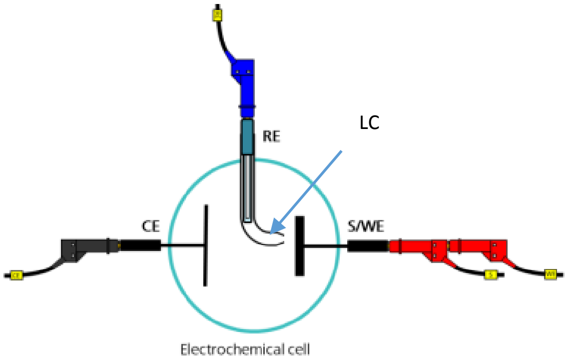

Figure 1. 4 Schematic view of the three electrode setup (extracted from Metrohm Autolab Application Note[2])

1.1.3. Kinetics and mechanism of electrodeposition

At dynamic equilibrium, the rate of metal ions being reduced and those atoms being oxidized must be equal and no net change in the system should occur. In order to perform metal electrodeposition at the cathode, i.e. the process of metal ions being discharged and forming an adherent thin layer onto a substrate, the system must be moved away from the equilibrium condition. As a result, an external potential or current must be applied for electrode reactions to take place. When a current is flowing through an electrochemical cell, the operating potential of an electrode will differ from its equilibrium potential (also called open circuit potential, OCP). Assume E^0 is the equilibrium potential of the electrode, E(I) is the operating potential of the electrode, then the difference η between these two potentials is called overpotential, which is also referred to as polarization of the electrode:

$$\eta = E(I) - E$$ **Eq 1. 7**

The overpotential represents the extra energy needed to force the electrode reaction to take place at the required rate. η increases with increasing the current density. For large negative values of overpotentials ($\eta \geq 100$mV) and for one-electron reactions, the current density i (i=I/S, where S is the surface area of the electrode) increases exponentially with the overpotential η according to the equation:

$$i = -i_0 e^{-\alpha z f \eta}$$ **Eq 1. 8**

For large positive values of overpotential (anodic processes), we have instead:

$$i = i_0 e^{(1-\alpha) z f \eta}$$ **Eq 1. 9**

where i_0 is the exchange current density (i_0 = i when η = 0), α the transfer coefficient, F the Faraday constant, R the gas constant, T the absolute temperature, and f = F/RT.

These exponential relationships show that even small changes in η produce large changes in the current density. Taking the logarithm of Eqs. 8 and 9, one obtain the Tafel equation:

$$\eta = a \pm b \log |i|$$ **Eq 1. 10**

Where *a* and *b* are constants and |*i*| is the absolute value of the current density. The sign holds for anodic and cathodic processes, respectively. The theoretical value of the constant *a* for the cathodic process (a_c), is:

$$a_c = \frac{2.303RT}{\alpha z F} \log i_0$$ **Eq 1. 11**

And that of b_c is:

$$b_c = \frac{2.303RT}{\alpha zF} \qquad \text{Eq 1. 12}$$

The current-potential relationship for deposition process defined by Eqs. 1.8, 1.9 and 1.10 is valid assuming that the rates of both the cathodic and anodic processes are determined by the charge transfer (Eq. 1.3) process at the metal surface. Under this circumstance, ion depletion in the near-electrode layer is negligible, and the overpotential is purely of an electrochemical nature[3]. At high overpotentials, however, the rate of deposition reaction is limited by mass transport of M^{z+} ions to the electrode, and the maximum current density, which is also known as the limiting current density is given by:

$$i_L = \frac{nFD}{\delta} c_b \qquad \text{Eq 1. 13}$$

where n is the number of electrons involved in the reaction, F the Faraday costant, D the diffusion coefficient of the depositing species M^{z+}, C_b the bulk concentration of ions in the solution, and δ the diffusion layer thickness.

Three mechanisms contribute to mass transport: diffusion (movement of species under the influence of a concentration gradient), convection (stirring or hydrodynamic transport) and migration (movement of a charged body under influence of an electric field). For neutral species like dissolved oxygen and for low concentration of reacting ionic species in a high conductivity supporting electrolyte, the contribution of migration is negligible. Transport then occurs only by diffusion and convection; in particular the diffusion process is frequently described by the Nernst diffusion layer model, whereby the electrolyte volume is divided into two regions: near the electrode surface, convection is negligible and transport occurs by diffusion only; in the bulk electrolyte instead, convection homogenizes electrolyte composition and no diffusion takes place.

Since mass transport of reactants and products is now slow compared to the charge transfer process, a concentration gradient develops between electrode surface and the bulk solution[4]: the concentration of reactants M^{z+} diminishes and that of products increases closer to the interface. The diffusion layer thickness δ defined by the Nernst diffusion layer model is then illustrated in **Fig 1.5**. This model assumes that the concentration of M^{z+} ions has a bulk concentration c_b at a distance δ from the electrode surface, and then falls off linearly to zero at the electrode surface since M^{z+} ions are reduced as soon as they reach the surface of the electrode. At distances greater than δ, the concentration of the reactant M^{z+} equals that in the bulk, stirring is efficient, and M^{z+} ions must diffuse through the diffusion layer to reach the electrode surface.

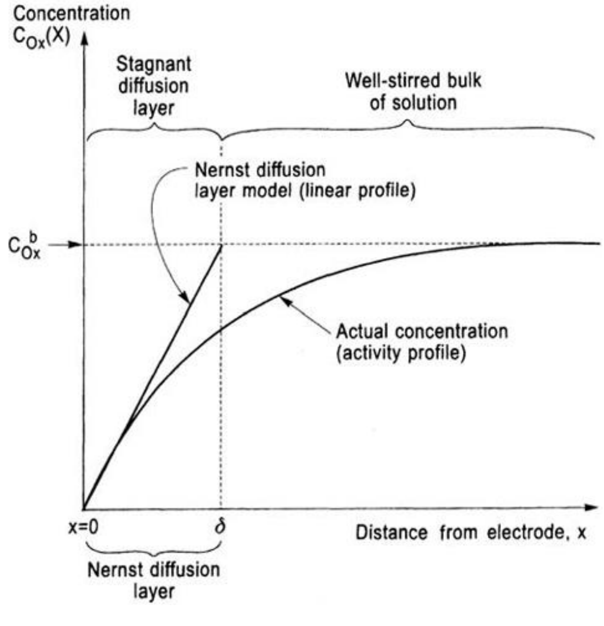

Figure 1. 5 Variation of the concentration of the reactant during non-steady-state electrolysis; C_{Ox}^{b} is the concentration in the bulk; C_{ox}^{s} is the concentration at the surface. (extracted from Modern Electroplating, 5th edition)

At the limiting current density, electrodeposition occurs under diffusion control because the depletion of metallic ions at the cathode-solution interface becomes a more important controlling influence than the applied potential. When a current density larger than the limiting current is applied, some new electrode reaction other than the reduction of M^{z+} ions must take place to utilize the excess electrons; these reactions often include the decomposition of the solvent. In aqueous solutions for example hydrogen evolution may occur.

The limiting current density is of great practical importance in electrodeposition since the type and quality of metal deposits depend on the relative values of the deposition current and the limiting current. It is well known that electrodeposition under limiting current conditions leads to dendritic or powdery deposits.

1.1.4. Understanding electrodeposition at the atomic level

Electrodeposition has recently become an advanced technology capable to produce both elemental metals and alloys atom by atom, forming sophisticated, controllable structures and tailored properties. The electrodeposition of metallic layers from aqueous solutions is based on the discharge of metal ions in the electrolyte at the cathodic surface (the substrate). The metal ions may be either supplied from metal salts in the solution, or are formed by the anodic dissolution of so-called sacrificial anodes, made of the same metal that is to be deposited at the cathode[5]. Metal ions in the solution never exist in a simple form. They are always surrounded by other molecules or ions, especially water molecules. A geometric structure of the water molecule is shown in **Fig 1.6**. The angle of 104.45°, formed between the two hydrogen-oxygen bonds results in a strong electric dipole moment within the water molecule. The electrostatic interaction between the positively charged metal ions and the electric dipole in the water molecules enables the hydration of metal ions, also known as solvated ions sheathed with a layer of water molecules, and denoted as $[M(H_2O)x]^{z+}$, where x is the number of surrounding water molecules. In fact, the metal ions can be surrounded by several layers of water molecules, with each layer being more loosely bound than the one inside it.

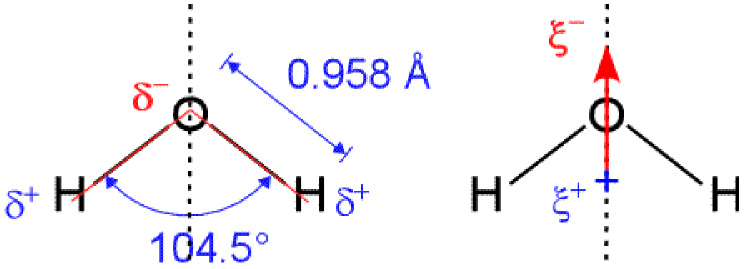

Figure 1. 6 Schematic representation of the structure of a water molecule, shown as dipole[6]

Metal ions accept electrons from the electrically conducting material at the cathode-solution interface, are reduced and then deposit onto the surface of the substrate. The electrons needed during this process are provided by an externally applied potential source. In practice, the electrodeposition process is more complex, involving a series of intermediate stages, including:

- Transport of the hydrated metal ions or complexes from bulk solution to the cathode.
- Stripping the hydration sheath from the metal ions at the cathode-solution interface.

- Charge transfer with formation of adsorbed atom (ad-atom) at the cathode surface.
- Formation of crystal nuclei by diffusion of the ad-atoms at the cathode surface.
- Formation of thermodynamically stable crystal nuclei to form a metallic layer.

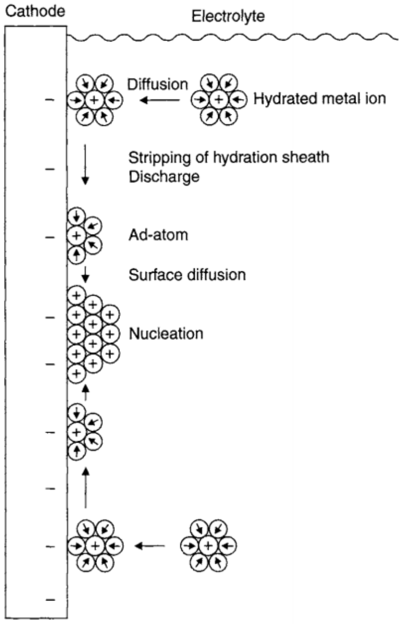

Figure 1. 7 Schematics of the electrodeposition process. From the electrode sides to its center: migration of hydrated metal ions to a cathode, surrender of the hydration sheath, formation of ad-atoms, and formation of crystal nulcei at the cathode surface. (extracted from "Electroplating: Basic Principles, Processes and Practice")[5]

These steps are shown together in **Fig 1.7**, with the understanding that this is a simplified depiction of the actual process.

As discussed before, transport of metal ions from the bulk solution to the cathode surface is primarily realized by convection, then diffusion. The discharge of ad-ions to generate ad-atoms occurs within the electrolyte double layer, which is spontaneously formed by a separation of charge between the metal surface (the substrate) and the electrolytic solution. Various models are available for the actual distribution of charge: the Helmholtz model assumes a separation of charge occurring right at the interface, the Gouy-Chapman model assumes a distribution of charge in the electrolyte dictated by electrostatic and thermal energy of the electrons, and finally the Stern-Graham model, which essentially integrates the former two. Though ad-ions lose most of their charge during the process of entering the electrolyte double layer, some residual charge may remain as well as the hydration sheath. After moving through the electrolytic double layer, the ions are adsorbed onto the surface of the substrate, where they form ad-atoms.

To finally form a coherent metal film, two more steps are needed, known as nucleation and growth, or as a whole “electrocrystallization”. Nucleation results from the surface diffusion of ad-atoms on the surface, which contact each other and eventually form a stable nucleus where the increase in energy due to the formation of interfaces is balanced by the decrease in energy originated by solid state bonding. The growth process begins once the nuclei have reached a critical size by taking up further ad-atoms.

1.1.5. Electrodeposition of alloys

Electrodeposition of alloys was first developed in the 1840s, almost at the same time as single metal deposition. With properties superior to those of single metal electroplates, alloy deposits have witnessed an ever-increasing attention, recognized by a number of scientific and technical publications. An alloy electrodeposition process usually requires an electrolyte with two or more reducible metal ions, a conductive substrate, a power supply, and a container to hold the electrolyte and electrodes[7]. Besides, reproducibility in mixing the electrolyte, controlling the cell geometry and preparation of the substrate are necessary to develop a consistent and reliable process.

A polarization curve for the electrodeposition of alloy AB is shown in **Fig. 1.8**. In this ideal system, the reduction of the two metal ions occurs independently and deposition current for alloy AB is the sum of the pure metal partial currents of A and B. Referring to **Fig. 1.8**, deposition begins when the substrate potential is brought negative of the Nernst equilibrium potential for A, denoted E_A^{eq}. Within a specific potential window, only A is deposited. When the applied potential becomes more negative than the equilibrium potential for B, denoted E_B^{eq}, then codeposition begins. The composition of the resulting alloy can be determined from Faraday's law. In alloy deposition, the equilibrium potential of metals A and B should not be far apart, otherwise the two elements could nucleate separately, hindering alloy formation. One way to bring the two potentials closer in order to achieve codeposition is to complex the metals with suitable complexing agents.

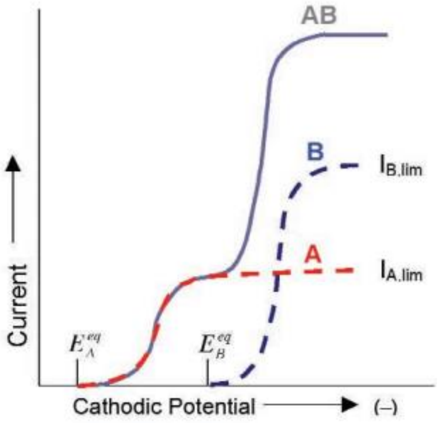

Figure 1. 8 An ideal polarization curve for the electrodeposition of the binary alloy results from the sum of pure metal (A and B) polarization curves[7]

Certain details of the polarization curves may explain why surface preparation and electrolyte agitation are important. For the region where the partial current of species A or B increases exponentially with the potential going more negative, the partial current is determined by charge transfer between the conductive substrate and the metal ions in the solution. Charge transfer is highly dependent on the nature of the substrate. As a result, careful preparation and cleaning of the substrate is essential if either species A or B is reduced under charge transfer limitation. When the potential becomes more negative, instead of charge transfer, mass transfer becomes the limiting process, and the mass transfer limited current is the maximum current that a system can achieve. This current is proportional to the precursor ion concentration, diffusivity as well as how strongly the electrolyte is agitated. In most cases of alloy electrodeposition, both charge transfer and mass transfer are important processes, therefore, both surface preparation and mixing conditions should be carefully controlled to get reproducible results. Moreover, the influence of electrolyte resistance between the substrate and counter electrode should be recognized, since the arrangement of the two electrodes may change the cell potential and affect the distribution of the current (current follows the path of least resistance through the electrolyte)[7].

The deposition of metals and alloys is also accompanied by hydrogen evolution as a consequence of solvent decomposition, which has a significant effect on the polarization and the composition of the deposited alloy. If a significant amount of hydrogen is evolved, the potential of the cathode during the alloy deposition may be mainly determined by the hydrogen evolution reaction and finally result in a poor efficiency for alloy deposition.

For the last two decades, the production of various types of iron alloy plating has been one of the most important developments in the metal finishing industry. For example, iron-nickel alloy plating has been widely studied for applications in decorative coating, macroscopic and microscopic sensors, actuators, and magnetic recording heads. Practically all iron is plated from acidic solutions of Fe(II) salts containing ferrous sulfate, ferrous chloride, or a mixture of the two. In these solutions, the presence of iron in the Fe(III) state is undesirable because it lowers the cathode efficiency for depositing the metal and cause deposits to be brittle, stressed, and pitted[8]. However, it is known that Fe^{2+} ions are easily oxidized to Fe^{3+} at the anode during electroplating or by oxygen in air[9]. Recently, several groups studied the possibility of depositing Fe-Zn[10], Fe-Mo[11], Fe-Pt[12] from a ferric bath with the pH ranging from 1.5 to 4.5. In these baths, iron is reduced mostly from ferric complexes, rather than ferrous ions, indicating that a solution containing a ferric salt can be an alternative electrolyte to sulfate or chloride baths. More recently, an alkaline solution based on citrate-glycine complexation of Fe^{3+} and Pt-p-salt complex was reported[13]. In the alkaline environment, the combination of citrate and glycine provide enhanced complexation of ferric ions, thus avoiding oxide/hydroxide precipitation, leading to a large decrease of oxygen content in the as-deposited FePt alloys.

1.2. Magnetic materials and magnetism

1.2.1. Introduction to magnetism

The origin of magnetism lies in the spin and orbital motions of electrons in solids, and how electrons interact with each other. Based on how materials respond to magnetic fields, the magnetic behavior of materials can be divided into five categories: diamagnetism, paramagnetism, ferromagnetism, ferrimagnetism and antiferromagnetism.

While the first two types (diamagnetism and paramagnetism) exhibit no magnetic ordering, the last three groups (ferromagnetism, ferrimagnetism and antiferromagnetism) show long-range magnetic order below a critical temperature.

A. Diamagnetism

Diamagnetism is a fundamental property of all materials, though its effect is usually very weak due to the non-cooperative behavior of orbiting electrons when exposed to a magnetic field. For diamagnetic materials (i.e., Cu, He), all the electrons of the atoms are paired up and show no net magnetic moment. However, when exposed to a field, a negative magnetization is produced and thus the susceptibility (χ=M/H) is negative and small. Another characteristic behavior of diamagnetic materials is that the susceptibility is independent of temperature (**Fig 1.9**).

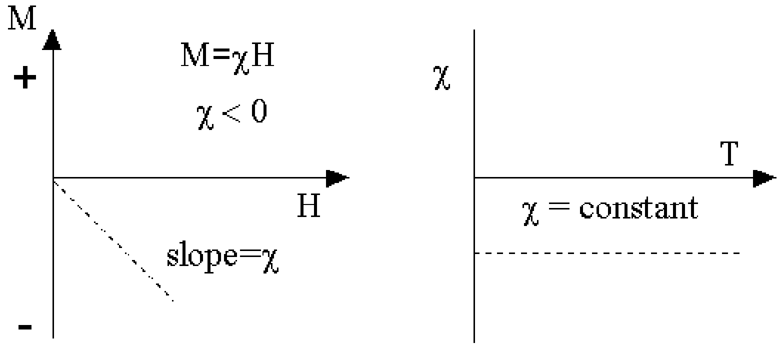

Figure 1. 9 Illustration of diamagnetic behavior: magnetic response to an external field (left); susceptibility of diamagnetic materials is temperature independent (right)[14].

B. Paramagnetism

In this class of materials, the atoms or ions comprising the material have a net magnetic moment due to unpaired electrons in partially filled orbitals. In the presence of a field, the magnetic moments can be partially aligned, or even be saturated when the field is very strong, due to the Zeeman energy that accounts for the potential energy of a magnetic moment in an external field. However, the individual magnetic moments do not interact magnetically. After removing the external field, the alignment of the moments will be random and the net magnetization will be zero (**Fig 1.10**).

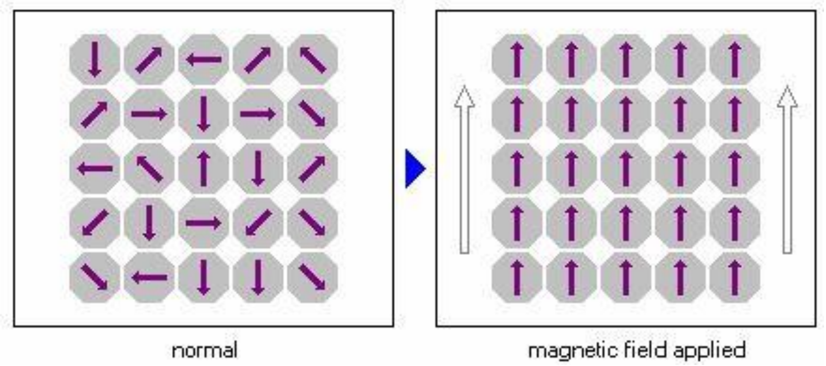

Figure 1. 10 Alignment of magnetic moments in paramagnetic materials (i.e., Na, Al) with and without an external field (extracted from the madsci.org)

C. Ferromagnetism

From an application standpoint, ferromagnetism is the most important type of magnetism. In ferromagnetic materials (i.e., Fe, Co, Ni), the magnetic moments of neighboring atoms are strongly coupled together and respond to external fields. These interactions are produced by electronic exchange forces (a quantum mechanical phenomenon due to the relative orientation of the spins of two electrons) and result in a parallel or antiparallel alignment of atomic moments. Unlike paramagnetic materials, ferromagnetic materials show hysteresis, because of their non-zero remanence at zero field.

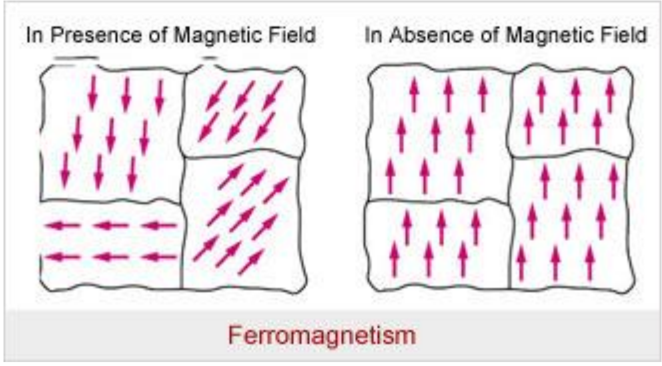

Figure 1. 11 Alignment of magnetic moments in ferromagnetic materials with and without an external field (extracted from the magnetic guide.com)

A magnetic hysteresis loop can be expressed in terms of B(H) or M(H) curves, with M(H) curve better reflecting the intrinsic properties of magnetic materials. **Fig 1.12** is a typical hysteresis loop showing the irreversible, nonlinear response of a ferromagnet to a magnetic field in the form of a M(H) curve, which reflects the arrangement of magnetization within ferromagnetic domains. Magnetic domains are small regions that can be magnetized independently of adjacent regions, whose size or granularity can have an important bearing on magnetization process. The material follows a non-linear magnetization curve when magnetized from a zero field value. When the field is sufficiently large, the material is saturated and all the magnetic moments are aligned parallel to the direction of the external field. Due to the mutual atom-atom interaction, the saturation field is much lower than that in paramagnets. After removing the field, part of the alignment will be retained: the material has become magnetized, and the magnetization at zero field is called remanence (M_r). To demagnetize the material, heat or an opposing magnetic field is required; the value of the opposing field is named coercivity (H_c), which measures the level of difficulty to magnetize a magnetic material.

To demagnetize a material using magnetic fields, a cyclic field with decreasing amplitude over time must be applied.

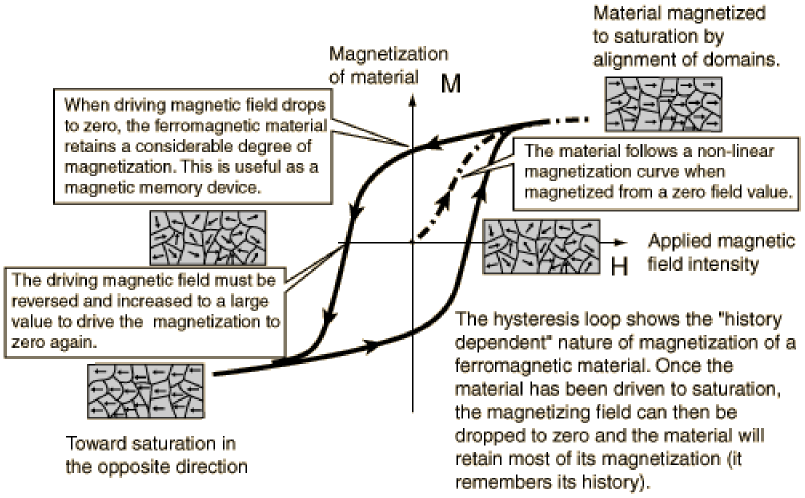

Figure 1. 12 Magnetic hystersis loop for a ferromagnet: magnetization M as a function of the magnetic field strength H. The relationship between magnetization and domain configuration is sketched as well[15]

In the SI system, $B=\mu_0(H+M)$, where $\mu_0=4\pi\times10^{-7}N/A^2$, so M and H have the same unit: A/m. In the CGS system, $B=H+4\pi M$, so B, H and M should have the same unit, however, different names are given to these quantities[16]: Gauss (G) as the unit for B, Oersterd (Oe) for H and emu/cm^3 for M. A unit conversion table between SI and CGS units is given:

Magnetic Term	Symbol	SI unit	CGS unit	Conversion factor
magnetic induction	B	Tesla (T)	Gauss (G)	$1T=10^4G$
magnetic moment	m	Am^2	Emu	1 Am^2=10^{3}emu
magnetization (volume)	M	A/m	emu/cm^3	1 A/m=10^{-3} emu/cm^3
mass magnetization	σ •	Am^2/kg	emu/g	1 Am^2/kg = 1 emu/g
magnetic field	H	A/m	Oersted (Oe)	1A/m=4 $\pi/10^3$ Oe

Table 1. 1 Common magnetic terms, units and conversion factor.

Note: if the graph axis is labeled H(Oe), it may be easier to change it to μ_0H, because then, for example, 1000Oe converts to 0.1T[17].

One factor strongly affecting the shape of M-H curve is magnetic anisotropy, which simply means that the magnetic properties depend on the direction along which they are measured[16]. A discussion of magnetic anisotropy will be provided later in this chapter.

D. Ferrimagnetism

Similar to ferromagnetism, ferrimagnetism exhibits all the hallmarks of ferromagnetic behavior: spontaneous magnetization, Curie temperature, hysteresis and remanence. However, ferrimagnetism has a different magnetic ordering than ferromagnetism: the crystal structure of these materials consists of two sublattices where magnetic moments are opposite to each other but with different magnitude, resulting in a net magnetization (**Fig 1.13**). The most important ferrimagnetic substances are certain oxides of iron and transition/main group metals, called ferrites.

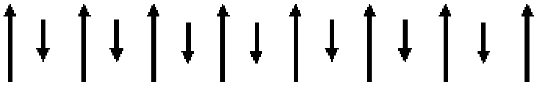

Figure 1. 13 Ferrimagnetism

E. Antiferromagnetism

Similarly to ferrimagnetic materials, the magnetic moments in antiferromagnetic materials tend to be aligned anti-parallel to their adjacent moments. The difference is that the net magnetization of antiferromagnetic materials is zero. Typical antiferromagnetic materials are ionic compounds, such as oxides. **Fig 1.14** shows the comparison of different types of magnetism.

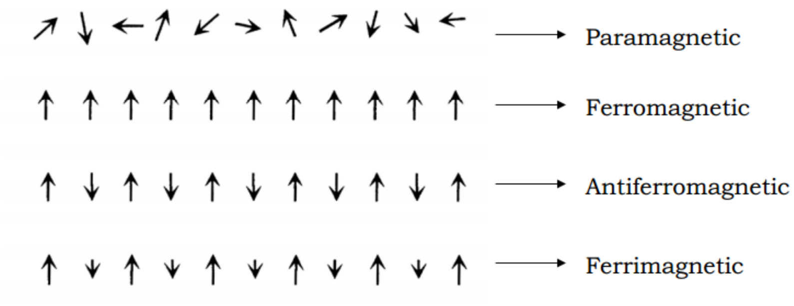

Figure 1. 14 A comparison of different types of magnetism.

1.2.2. Magnetic Anisotropy

Magnetic anisotropy is an important concept of practical interest, adopted in the design of most commercial magnetic materials. Essentially, this term means that the magnetic properties depend on the direction of measurement; magnetic anisotropy can be generated by distinct features, as follows:

1. Magnetocrystalline anisotropy (in short: crystal anisotropy)
2. Shape Anisotropy
3. Stress Anisotropy
4. Induced Anisotropy
5. Exchange Anisotropy

Among all these categories, only crystal anisotropy is intrinsic to the material, and only crystal and shape anisotropy will be discussed here. Crystal anisotropy can be regarded as a force tending to hold the magnetization in certain crystallographic direction in a crystal[16]. When an external field is applied, it has to work against the anisotropy force to turn the magnetization vector away from an easy magnetization direction, which is the direction of spontaneous magnetization in its demagnetized state.

When considering a polycrystalline thin film material without any preferential grain orientation, there is no crystal anisotropy but shape anisotropy may be observed. Shape anisotropy is originated by the shape of the magnetic material, with the magnetization preferentially oriented along the longer dimension. In thin film specimen in particular, it will be easier to magnetize the film along the in-plane direction (the long axis) than out-of-plane direction (the short axis).

In a real situation, often more types of anisotropies are present. For the materials investigated in this work (FePt, FeNiPt and FeNi), the discussion will be limited to uniaxial anisotropies of two different physical origins: crystal and shape anisotropy. Given an equatomic FePt thin film specimen with tetragonal ($L1_0$) structure and perpendicular anisotropy as an example, the out-of-plane direction (OB direction in **Fig 1.15**) represents the easy axis of crystal anisotropy and the in-plane direction (OA direction) represents the easy axis of shape anisotropy. Since the various uniaxial anisotropy energies components are given in the form:

energy = (constant)·$\sin^2$(angle between M and easy axis)[16]

we have:

Crystal anisotropy energy: $E_c = K_c \sin^2(90^o - \theta)$ **Eq 1. 14**

Shape anisotropy energy: $E_s = K_s \sin^2\theta$ **Eq 1. 15**

Total anisotropy energy: $E = E_c + E_s = K_c \cos^2\theta + K_s \sin^2\theta$ **Eq 1. 16**

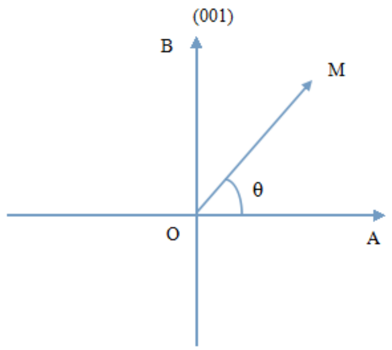

Figure 1. 15 Mixed Anisotropy

Minimization of the total energy results in the direction of easiest magnetization being not along an intermediate axis lying between OA and OB, but instead along one of them - along OA if the shape anisotropy is stronger, or along OB if crystal anisotropy is stronger.

1.2.3. Basics of Magnetic Recording

Magnetic recording has been with us for over a century and it is still evolving very rapidly. This technology was first demonstrated in principle by Valdemar Poulsen in his “telegraphones” as early as 1898, in which, magnetic wires were used as the magnetic recording medium, which moved past a recording head to record and read the signal[18]. With the introduction of magnetic tape and hard disk drive, magnetic recording technology has made significant progress in the past decades. Magnetically recorded data are now almost all digital. Data are mainly stored on hard disks that are used for mass memory in computers. A typical hard disk drive is shown in **Fig 1.16**. Tape recording remains a place for archival storage of vast quantities of digital data, as well as for low-end consumer applications[19].

Figure 1. 16 Top view of a 36 GB, 10,000 RPM, IBM SCSI server hard disk, with its top cover removed. (The IBM Ultrastar 36ZX, note the height of the drive and the 10 stacked platters)

Regardless of whether it is done on disk or tape, magnetic recording stores information onto a moving magnetic medium. The information is coded into the current passing through a miniature electromagnet – the write head. The field produced by the write head must be sufficient to switch the magnetization of the medium, which is usually a thin film composed of tiny, crystalline, single-domain grains or "particles". Digital information is written in elongated patches of width w and length l, with $w/l \approx 5$, on a disc or on a tape. A single bit is recorded in the magnetization of N particles in the patch. For a good signal-to-noise ratio (SNR), the individual grains should be small and more or less magnetically decoupled from adjacent grains. Since SNR is of order 10 log N; if a value of 30dB is required, N has to be around 1000.

Signal-to-noise ratio is a measure of signal strength relative to background noise. If the incoming signal strength in microvolts is Vs, the noise level in microvolts is Vn, then the signal-to-noise ratio in decibels (dB) is given by:

$$SNR = 20 \cdot \lg(V_S / V_n)$$ **Eq 1. 17**

If Vs equals V_n, then SNR is zero, in this situation, the signal is unreadable. Ideally, V_s is significantly larger than Vn, so that SNR is positive, say V_s equals 10 μV and V_n equals to 1 μV, then SNR is 20dB, which results in the signal being clearly readable.

In magnetic recording, to read back data on HDDs, a read head must be able to identify the difference between the signal produced by a patch magnetized in one direction (1s) and the opposite direction (0s). The relationship between SNR and the features of the bit is given below[20]:

$$SNR = \frac{D_{ch} B^2 W}{2\pi D^3}$$ **Eq 1. 18**

Where D_{ch}=PW50/T[21] (PW50: the pulse width at 50% of the pulse amplitude, also known as full width at half maximum; T: sampling clock period), an effective measure of the density of channel, B is the bit length, which is comprised of a collection of uniformly magnetized smaller crystalline grains, W is the track width, and D the grain size. From the equation, it is clear that small grain sizes are preferred for magnetic recording media.

1.2.4. Longitudinal recording vs. perpendicular recording

In magnetic recording systems, two recording modes can be implemented: longitudinal and perpendicular. Prior to 2005, when perpendicular recording was introduced in hard disks, most magnetic recording was longitudinal. In longitudinal recording, the media grains are oriented in the plane of the magnetic thin films and a longitudinal recording head is designed to create a maximum longitudinal magnetic field component (**Fig 1.17**). When the write current I_w that contains the information to be stored is applied to a coil, it creates a magnetic flux Φ which runs through the soft magnetic core. The core has a gap as shown. Due to the flux conservation law, the total flux through the core and the gap should be the same. The flux then changes the state of magnetization of the magnetic media immediately under the head, as can be seen clearly in **Fig 1.17**.[22]

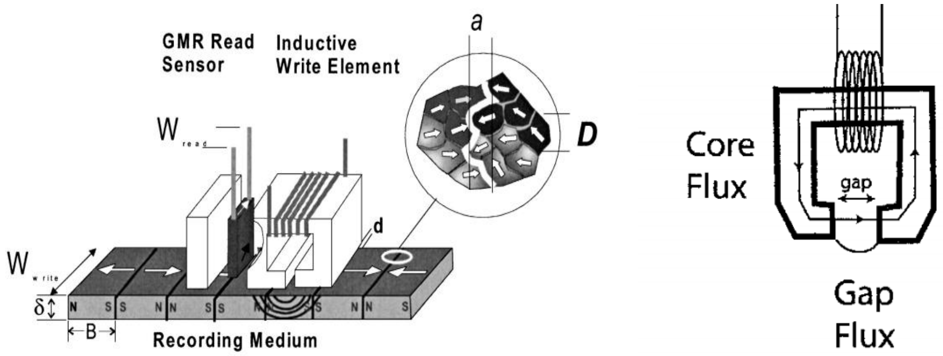

Figure 1. 17 A schematic of a longitudinal magnetic recording system (left) and a typical longitudinal recording head (right)[23]

At first, longitudinal recording was successfully introduced to achieve high areal densities in the industry while perpendicular recording was not considered, due mainly to problems in the fabrication of the head. However, the situation changed when it became clear that the potential of longitudinal media was about to be exhausted due to the superparamagnetic limit[24]; this phenomenon consists in the fact that when the grain size of the magnetic media materials continues to decrease, the grains become so small that the thermal energy alone can flip their magnetization direction and thus destroy the recorded information. This occurs approximately when thermal energy (k_BT) is competitive with the anisotropy energy of the grains (K_uV), where k_B is the Boltzmann constant, T is the absolute temperature, K_u is the uniaxial magnetic anisotropy per unit volume and V the grain volume. Normally, we consider that when $K_uV \geq 60k_BT$ (the coefficient is indicative and can change with varying stability requirement), the storage system is stable for around 10 years.

There are mainly two ways to extend the superparamagnetic limit and obtain higher storage densities: (i) by increasing the value of K_u or (ii) increase the volume of grains. By simply increasing the grain volume V without adopting new technologies, the superparamagnetic limit is extended at the expense of storage density. In contrast, use of perpendicular recording allows an increase in grain size in the perpendicular direction without affecting storage density. In parallel, metal alloys with higher anisotropy have been developed over time, allowing an increased resistance to demagnetization, permitting eventually higher areal densities of information.

Grains in the perpendicular magnetic media are grown in the vertical direction so that they have smaller in-plane diameter, resulting in lower media noise and additional room on a disk to pack more data, which eventually results in a higher storage density. In the perpendicular recording system (**Fig 1.18**), the vertical field is generated by a perpendicularly oriented write head. Different from the one used in longitudinal magnetic recording, the vertically oriented magnetic flux runs from the head pole into the magnetic media, then passes through the soft magnetic underlayer, which is made of high permeability materials and serves as the return path for the magnetic flux.

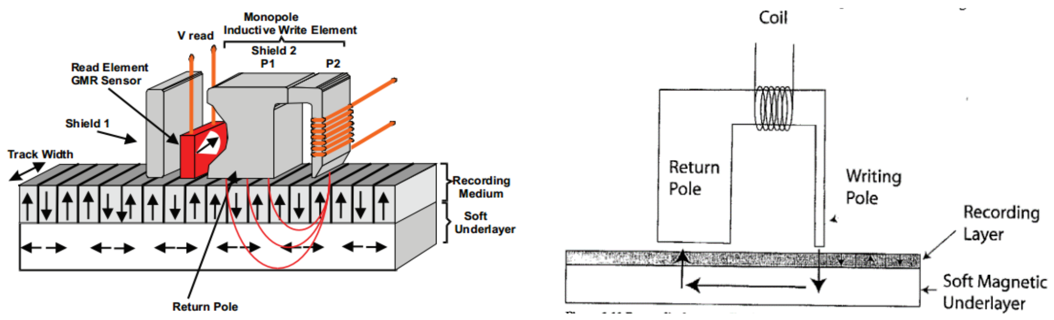

Figure 1. 18 Schematic diagram of a perpendicular recording system[25] and a perpendicular recording head[23]

Typically, the maximum fringing field in the longitudinal head is about $2\pi M_s$, while the maximum vertical field generated by the perpendicular head is doubled to $4\pi M_s$. As we know, a higher recording field has the ability to write magnetic media with higher coercivity H_c. This allows adoption of media with higher anisotropy in the perpendicular recording system, further decreasing grain size while maintaining thermal stability.

1.2.5. Magnetic materials for recording media

Magnetic materials for recording media are magnetically hard, having sufficient hysteresis to maintain a permanent record of the data, but not too hard as to impede remagnetization in the field produced by the write head. Digital information is encoded in the direction of magnetization of domains in the magnetic medium, therefore, a relatively square hysteresis loop and the control of the nucleation of reverse domains are desirable.

For many years, media materials consisted of dispersions of single-domain particles in a polymer matrix, with an easy axis parallel to the substrate, being therefore used in longitudinal recording systems. Commonly used materials were CrO_2 and needle-shaped γ-Fe_2O_3, sometimes doped with Co on the surface to increase the coercivity.

The commercial thin film media on hard disks are now generally CoPt-based alloys with high Co content (70-80 at%), hexagonal crystal structure and a coercivity of about 3kOe, with the easy axis along the c direction, and with Ta, Cr or B (nonmagnetic elements) added to induce adjacent grains to become magnetically decoupled and create a granular nanostructure. However, since these Co-Pt based alloys do not have very high anisotropy, their minimum stable particle size for thermal stability is around 10nm, which is too large a size for future high density recording. Therefore, there is a need for media with ultra-high anisotropy, which can be achieved for example in equiatomic Co-Pt or Fe-Pt based systems. **Table 1.2** is a list of magnetic materials with high anisotropy, where Ku is the uniaxial anisotropy, Ms the saturation magnetization, $H_k=2K_u/Ms$ the anisotropy field, Tc the Curie temperature, $\delta w=\pi(A/K_u)^{1/2}$ the domain wall width, $\gamma=4(AK_u)^{1/2}$ the domain wall energy, $Dc=1.4\ \gamma/M_S^2$ the single particle domain size and Dp the minimal stable grain size for 10 years.

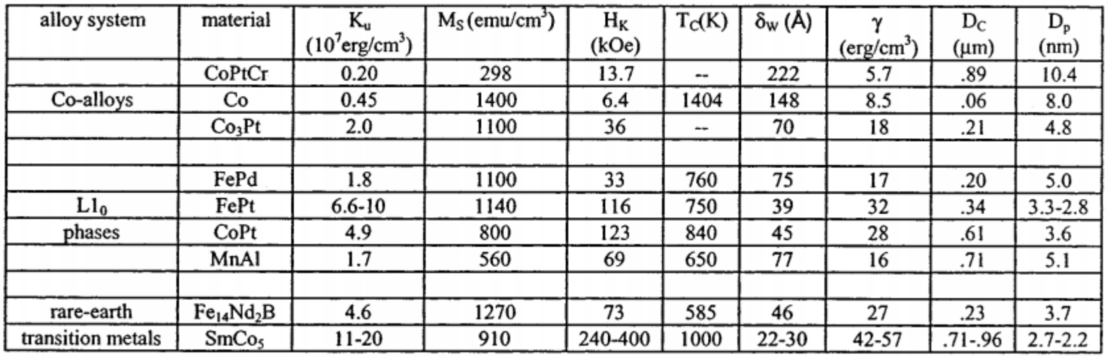

alloy system	material	K_u (10^7erg/cm^3)	M_S (emu/cm^3)	H_K (kOe)	T_C(K)	δ_W (Å)	γ (erg/cm^3)	D_C (μm)	D_p (nm)
	CoPtCr	0.20	298	13.7	--	222	5.7	.89	10.4
Co-alloys	Co	0.45	1400	6.4	1404	148	8.5	.06	8.0
	Co_3Pt	2.0	1100	36	--	70	18	.21	4.8
	FePd	1.8	1100	33	760	75	17	.20	5.0
$L1_0$	FePt	6.6-10	1140	116	750	39	32	.34	3.3-2.8
phases	CoPt	4.9	800	123	840	45	28	.61	3.6
	MnAl	1.7	560	69	650	77	16	.71	5.1
rare-earth	$Fe_{14}Nd_2B$	4.6	1270	73	585	46	27	.23	3.7
transition metals	$SmCo_5$	11-20	910	240-400	1000	22-30	42-57	.71-.96	2.7-2.2

Table 1. 2 Comparison of magnetic materials with high anisotropy[26]

1.2.6. Bit patterned media and heat-assisted magnetic recording media

As the areal density of the hard disk drive approaches 1 T bit/in^2, the recording media might not be stable enough when adjacent recording bits are too close to each other (see

Fig 1.19). To solve this problem, several alternative technologies have been proposed, including the bit-patterned media (BPM) and heat-assisted magnetic recording (HAMR).

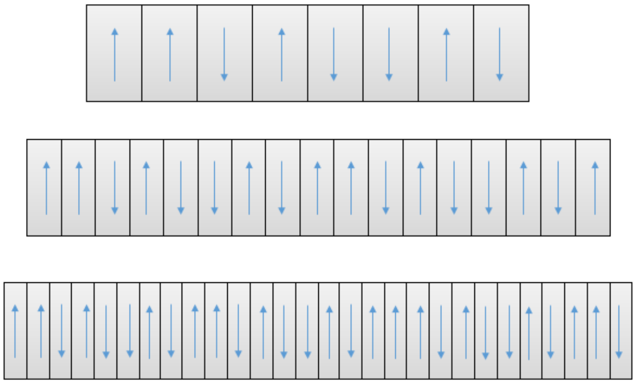

Figure 1. 19 Diagram indicating the increase of recording density (Guijun Li, Development of Recording Technology with FePt recording media and magnetic tunnel junction sensors with conetic alloy, PhD thesis, HKU, 2013)

Unlike conventional magnetic media, in which a bit consist a bunch of grains to maintain signal to noise ratio, a bit patterned medium (BPM) is patterned to form a dot array where each dot acts as a bit, which is exchange decoupled and can store information independently, avoiding demagnetizing fields from adjacent grains (**Fig 1.20**). Since the volume of a dot is much larger than a grain in conventional media, BPM is considered to be thermally more stable even with high areal density. Therefore, it has been considered as a promising candidate for future magnetic recording. To achieve 10 Tbit/in^2 areal density in BPM, the bit size is required to be around 8nm. In this condition, thermal fluctuation is even more important, and materials with very high magnetic anisotropy (for example, $L1_0$ FePt) would be needed to ensure the thermal stability of the individual bits.

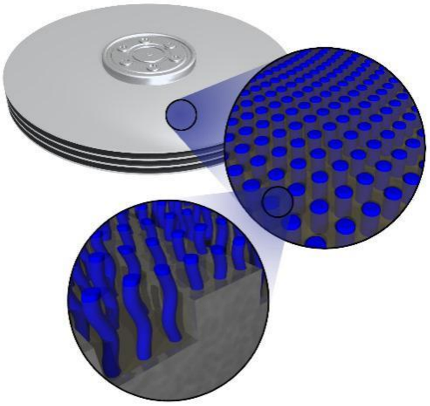

Figure 1. 20 Concept of bit patterned media (image via http://www.nist.gov/mml/msed/functional_polymer/templatedassembly.cfm)

Compared to the conventional recording technology, heat-assisted magnetic recording (HAMR) adopted a new degree of freedom: write temperature. During the writing process, the magnetic medium is temporarily heated to reduce the coercivity to a value lower than the available magnetic write field, thus orienting the bit magnetization. After writing, the heated region is rapidly cooled down to store the information. A diagram illustrating the HAMR writing process is shown in **Fig 1.21**, showing that a tightly focused laser beam is placed in front of the write head and used to heat the medium. The magnetic media for HAMR technology should demonstrate large anisotropy at room temperature, which can be sufficiently reduced during the heating process. Currently, FeNiPt is one of the most promising candidates for HAMR recording media.

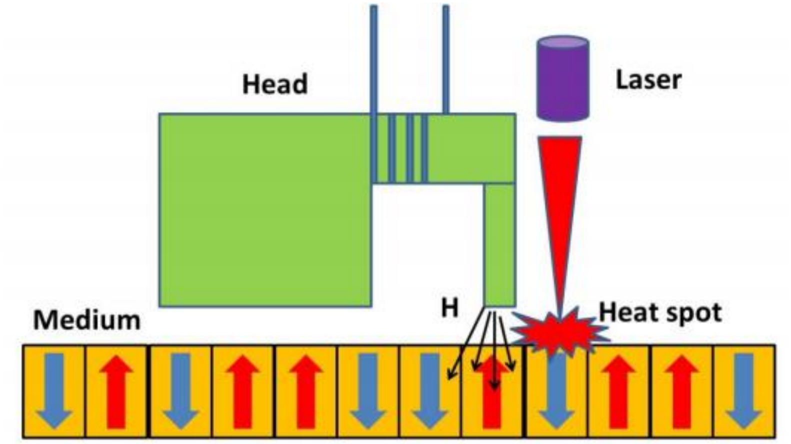

Figure 1. 21 A sketch illustrating the HAMR writing process[27]

1.2.7. History and magnetic properties of permanent magnet

Permanent magnets are hard magnetic materials. They display an extremely wide range of applications in our daily life, such as computers, motors, generators and medical device, with a purpose of providing a magnetic field in a particular volume of space[16]. They have an extremely long history that can be dated back to the so-called "lodestones" - the iron oxide Fe_3O_4, with only application in the compass, an instrument first described in Europe[28] but actually invented in China around 1000 A.D.[29] In 1931, a magnetic alloy based on Fe, Ni and Al ("Alni") was discovered by T. Mishima, starting the half-century-long development period of the highly successful Alnico family of magnets, which also contain cobalt in addition (up to 40%)[30]. Later, the consumption of Alnico has severely declined in the last decade due to the appearance of Co-free magnets that are either cheaper (ferrite, 1952) [31] or much better in terms of coercivity and energy product ($Nd_2Fe_{14}B$, 1983)[32], as well as the discovery of Sm-Co based magnets (1970) [30] which have an even higher Co contents, but make much better use of it compared to Alnico.

Fig 1.22 shows the manufacturing costs as a function of $(BH)_{max}$ for the current four major commercial permanent magnets (Alnico, ferrite, rare-earth based SmCo and $Nd_2Fe_{14}B$)[33]. Though most magnetic properties of the ferrites are rather modest, the fact that raw materials are cheap and abundant explains the enormous success of ferrite over all other permanent magnet types. In comparison, while the cost of raw materials can be relatively high, rare-earth magnets like $SmCo_5$ and $Nd_2Fe_{14}B$ display a much larger $(BH)_{max}$, in which the 3d transition metals, namely the strong magnetic Co or Fe provide high magnetization while the 4f electrons in the rare-earth component contribute an extremely strong magneto-crystalline anisotropy.

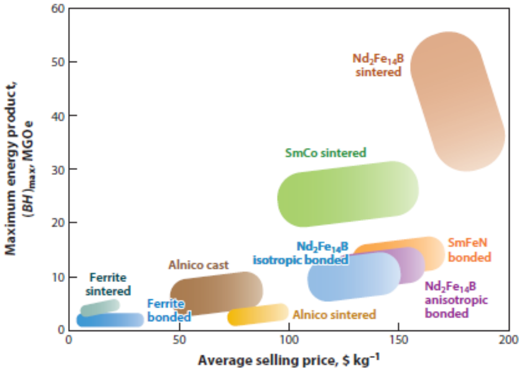

Figure 1. 22 $(BH)_{max}$ as a function of the average selling price per kilogram for the four major commercial magnets in US, 2012.[33]

1.3. Thin film characterization techniques

1.3.1. X-ray diffraction

X-ray diffraction (XRD) is a nondestructive technique used to characterize the crystal structure, grain size and the preferential orientation of a crystalline sample. Its working principle can be expressed by Bragg's law:

$$2d\,\sin\theta = n\lambda \qquad \textbf{Eq 1. 19}$$

Where *d* is the spacing between adjacent diffraction planes in the lattice, *θ* the angle between the incident x-rays and the diffraction plane, *n* the order of reflection, and λ the wave length of x-ray. The spacing of (hkl) planes can be calculated using equations such as those reported below (for hexagonal and orthorhombic system):

Hexagonal:

$$\frac{1}{d^2} = \frac{4}{3}\left(\frac{h^2 + hk + k^2}{a^2}\right) + \frac{l^2}{c^2}$$

Eq 1. 20

Orthorhombic:

$$\frac{1}{d^2} = \frac{h^2}{a^2} + \frac{k^2}{b^2} + \frac{l^2}{c^2}$$

Eq 1. 21

Knowledge of the d-spacing of {hkl} planes can thus be used for phase identification by comparing the XRD results with the power diffraction file (PDF) database.

The most commonly used X-ray source is Cu, with the wavelength of Cu Kα line being 1.5418 Å. In some other case, Co is used when dealing with materials that tend to absorb x-rays emitted by the Cu source, which makes the detected peak intensity quite low.

The most common configuration of an x-ray diffractometer is the so-called *θ*-2*θ* (Bragg-Brentano) geometry, which is shown in **Fig 1.22**. In this setup, only lattice planes parallel to the sample surface contribute to the XRD patterns. Therefore, for textured samples, only few families of reflections are observed. The *θ*-2*θ* scan is the basic configuration of an X-ray diffractometer; by changing its configuration, many other functions can be achieved. For example, x-ray reflectivity (XRR) can be used to measure the thickness of a thin film.

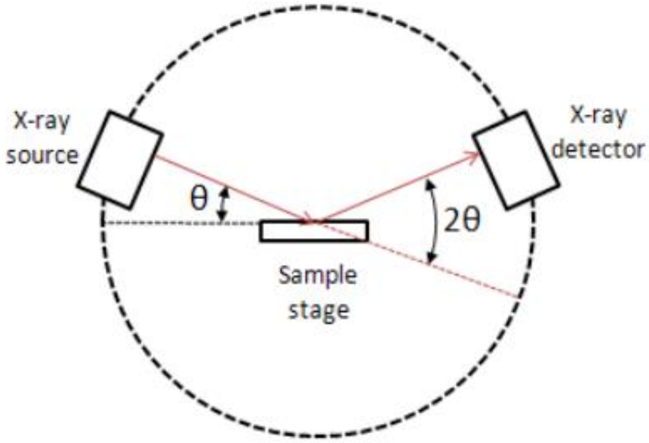

Figure 1. 23 Bragg-Brentano geometry of an x-ray diffractometer[34]

1.3.2. Magnetic measurement

A magnetometer is a basic tool to study magnetic materials. In this thesis, a vibrating sample magnetometer (VSM) is used to measure hysteresis loops, thus providing a variety of magnetic properties: saturation magnetization, coercivity, remanence, switching field distribution, and so on.

The working principle of a VSM is based on Faraday's law of induction. During the measurement, the sample is fixed to the sample rod and vibrates with a given frequency and amplitude (see **Fig 1.23**). The sample is centered between the two pole pieces of an electromagnet that generates a magnetic field of high homogeneity in order to uniformly magnetize the sample. Hence, the change in magnetic flux originating from the vertical movement of the sample induces a voltage in the stationary pickup coils that are mounted on the poles of the electromagnet. The induced voltage is proportional to the magnetic moment of the sample, which can be varied by changing the magnetic field produced by the electromagnet.

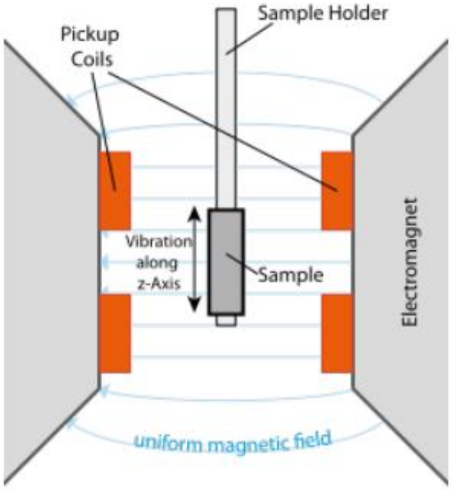

Figure 1. 24 Schematic of a vibrating sample magnetometer[35]

The measurement setup of a VSM is very sensitive even to very low magnetic moments down to the μ emu range. By dividing the measured saturation magnetic moment m of a sample by its volume (thickness × area), magnetization Ms can be calculated, which is an intrinsic property (other intrinsic properties include magnetic ordering temperature like Curie temperature T_c) and regarded as a constant for the material under study. Besides, the coercivity H_c, which is largely influenced by the microstructure and therefore is an extrinsic property, can also be obtained directly from the hysteresis loop. The extrinsic nature of coercivity is due to the fact that variations in domain structure and the motion of domain walls are highly sensitive to grain size and shape, the defect type and distributions, and the grain boundary structure[125].

1.3.3. Scanning Electron Microscopy

A scanning electron microscope (SEM) is a type of electron microscope that produces images of topographic features of a sample by scanning its surface with a highly focused electron beam. The magnification can be as high as 100,000X and spatial resolution better than 50 Å. The electron beam interacts with the specimen, generating a number of signals that can be detected (**Fig 1.24**).

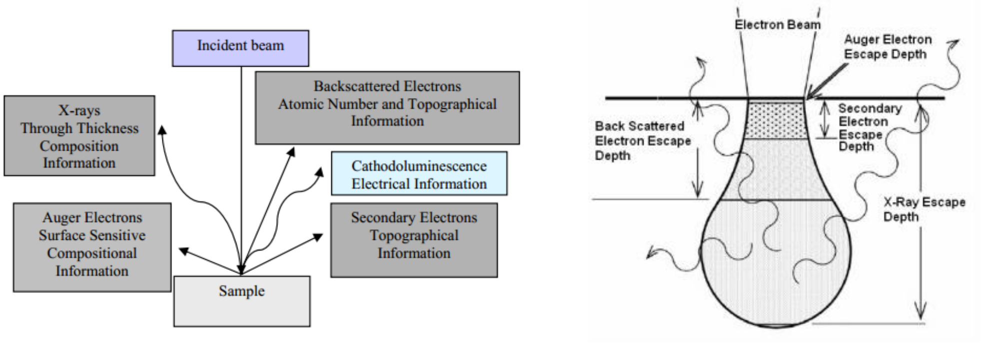

Figure 1. 25 Signals generated from electron beam – specimen interactions[36].

Each of these signals is produced with different efficiency, from a different volume, and carries different information about the specimen. The most common detected signal is that obtained by secondary electrons, which provide information about morphology and surface topography. The amount of secondary electrons generated depends on the angle between the surface and the electron beam, which explains the “edge effect” in the imaging contrast: more secondary electrons leave the sample at edges, resulting in higher brightness at these regions (**Fig 1.25**).

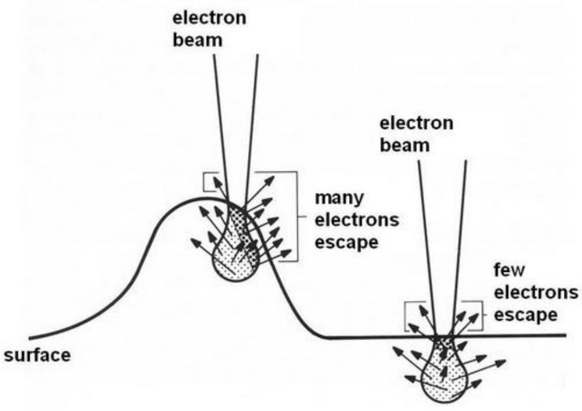

Figure 1. 26 The amount of secondary electrons generated depends on the surface[36]

Another important kind of signal is from backscattered electrons, which consists of incident electrons scattered through large angle (90^{o} or more). The ratio between the number of the backscattered electrons and the number of incident electrons is called the backscattered yield (η), which varies with the atomic number (Z) of the target element. For accelerating voltage above 5kV, the backscattered yield is almost independent of the energy of incident electrons and thus can be approximated by the function below:

$$\eta = -0.0254 + 0.016Z - 0.000186Z^{2} \quad \textbf{Eq 1. 22}$$

From equation 1.22, the yield is a function of Z only. Therefore, various elements in the specimen will appear with different brightness in a backscattered image, and the level of the contrast depends on the difference in the atomic number Z. The backscattered image therefore shows the distribution of different chemical phases in the sample. Because these electrons are emitted from a finite depth in the sample, the resolution of the image is not as good as that generated from secondary electrons.

A SEM is usually equipped with an energy dispersive X-ray (EDX) spectrometer to provide rapid semi-quantitative analysis of elemental composition with a sampling depth of 1-2 μm. In this technique, the interaction of the high energy beam with the sample results in characteristic X-rays that depend on the materials under examination. X-rays could be used to form spot, line or maps profiles, showing the elemental distribution in a sample surface. Keeping the electron beam stationary on a spot or a series of spots to generate spectra will help provide more localized elemental information while having the beam follow a line drawn on the sample image gives a plot of the relative proportions of previously identified elements along that spatial gradient. Compositional mapping further indicates the distribution and relative proportion of elements over the whole scanned area. The energy of the beam for these measurements is typically in the range of 10kV-20kV.

Limitations of the EDS analysis include a low (or none) instrument sensitivity for very light elements (H, He and Li), and the fact that the chemical state of the element may affect the accuracy in determining the composition. Therefore, this is certainly not a surface analysis technique. For better accuracy, methods like Rutherford backscattering spectrometry (RBS) and X-ray Photoelectron Spectroscopy (XPS) are recommended.

Besides, in conventional SEM, it’s hard to examine “wet” specimens such as coal, organic materials or materials that tend to decrepitate at low pressure[37]. However, when a “low vacuum” mode exists, many of these types of samples can be successfully characterized. For samples with insulating surface, an electrically conductive thin film, such as carbon, silver or platinum, must be sputtered onto the surface for studies in conventional SEM, unless the instrument is capable of operation in a low vacuum mode.

1.3.4. Surface Analysis

Surface roughness is an important property in thin film research as well as magnetic recording media. In a hard disk drive, the magnetic thin film must be exceptionally flat to prevent the writing head from colliding with the medium: the surface roughness of these films is normally less than 0.3 nm.

AFM, as a high-resolution imaging technique that produces precise topographic images of a sample, can ideally resolve features at the atomic level and is therefore a most common tool to characterize thin film surface. It has some significant advantages as an imaging tool when compared with complementary techniques such as optical and electron microscopes: by using a sharp tip to probe the surface through raster scanning, it can image the surface topography with extremely high magnifications, up to 1,000,000X. The measurements of an AFM are made in three dimensions: the horizontal X-Y plane and the vertical Z dimension (the height or depth of the surface features), with the resolution of Z-direction higher than X-Y plane.

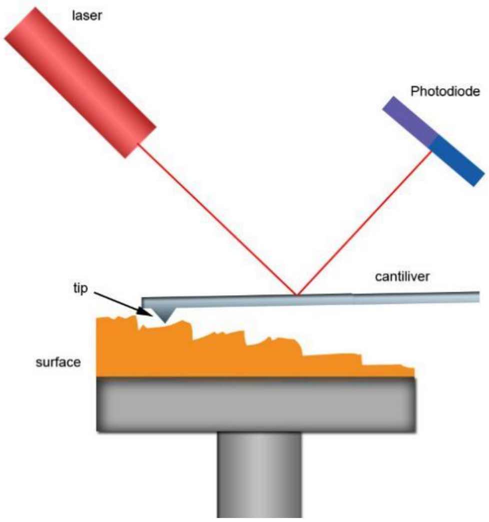

Figure 1. 27 Drawing of the basic principle of Atomic Force Microscopy (AFM)[38]

Typically, an AFM has two scanning modes with different cantilevers: contact mode and tapping mode. Contact mode is the most common method of operation in AFM and is used to obtain 3D topographical information of nanostructures and surfaces. In contact mode, the tip is attached to the end of a cantilever and is in perpetual contact with the sample. As the scanner gently traces the tip across the sample, the contact force causes the cantilever to bend and accommodate changes in topography. The bending is detected by means of a laser beam, which is reflected from the back side of the cantilever.

The problem of having high lateral forces between the cantilever and surface in contact mode can be solved by adopting the tapping mode, which has the tip touching the surface only for a short time. In the tapping mode, the cantilever is driven at its resonant frequency when the tip scans over the surface. As the oscillating cantilever begins to intermittently contact the surface, the cantilever oscillation is necessarily reduced due to energy loss caused by the tip contacting the surface. The reduction in oscillation amplitude is used to identify and measure surface features. The tapping mode is often used to image samples with structures that are weakly bound to the surface or samples that are soft (e.g. polymers).

Since there are many kinds of interactions between the probe and the sample, the AFM can detect information other than surface morphology by using a special probe. For example, the magnetic signal of recording media can be sensed by Magnetic force microscopy (MFM) based on the magnetic force interaction between the probe and the sample.

MFM makes it possible for example to map the domain wall structures of a magnetic thin film material; additionally, the change of domain wall structure and dynamic analysis of magnetic materials with perpendicular anisotropy can be achieved once an in-plane magnetic field is applied. The resolution of a normal MFM is around 10-100 nm; in the best condition this is good enough to observe the magnetic dots of bit patterned media.

1.4. Overview of bit-patterned media and recent research in FePt nanodots

As mentioned before, a main approach to extend the superparamagnetic limit of a magnetic medium to 1.5Tb/in^2 and beyond[39] is to increase the grain volume (V) while applying new technologies, in particular transitioning: from the multigrain, magnetically isolated bits to a single grain, exchange coupled magnetic dot, physically separated from the others. This is achieved by patterning the bits into single domain units on a hard disk drive (HDD), the resulting patterned recording medium consists thus of a regular array of magnetic elements (for example, nanodots), with each element designed to store one bit: if a change of magnetization direction is present, a signal is generated as “1”, then the absence of the change would represent the bit “0”. The magnetic element is either a single crystal or polycrystalline with exchange coupled grains so that the entire element may behave as a single magnetic domain. Each single domain is now much larger than the grains in the continuous media, and switches as an entire unit in a Stoner-Wolfarth manner[40], i.e., by magnetization rotation of single crystal grains, which means the magnetic energy K_uV is no longer governed by the grain volume, but rather by the bit volume.[41]

The comparison between continuous media and bit-patterned media (BPM) can be discussed with regard to two separated functions: writing and reading. For a continuous medium, each bit utilizes a number of grains and information can be written anywhere on the disk and later recovered; however, continuous media suffer from noise and fluctuations in the output signal due to the irregular shape and size of bits[42] (unlike the bit-patterned media, bits in continuous media are defined by the boundary between two oppositely magnetized regions of a thin film, instead of the physical location of a patterned element[43], see **Fig 1.27**). For bit-patterned media in contrast, it is necessary that the information be written at the correct location: imperfections in the media fabrication process, namely, misplaced bit island, can cause write errors due to improper synchronization with the write head. On the other hand, BPM has its advantages in the reading process - signal-to-noise ratio is significantly improved due to the ordering of magnetic bits.

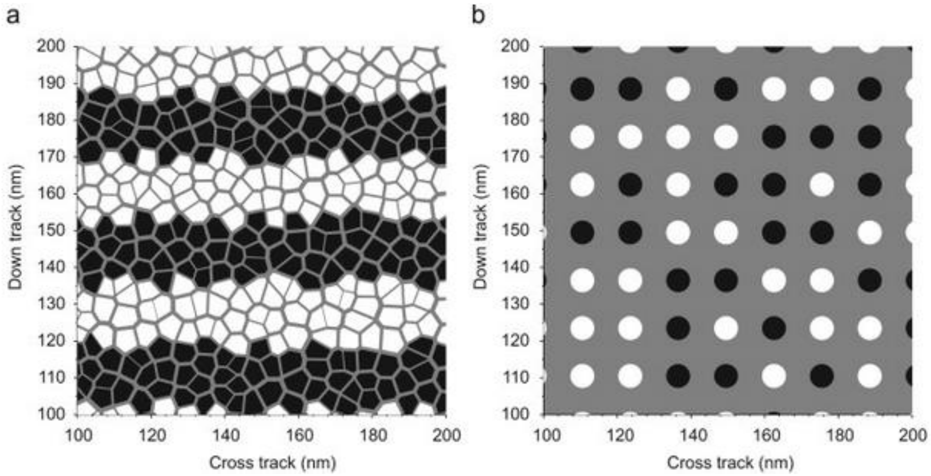

Figure 1. 28 Images of a continuous medium with an average grain pitch of 5.5nm (left); a bit-patterned medium with a dot pitch of 13nm (right)[42]

In 1999, C. A. Ross *et al*. reported arrays of cobalt or nickel pillars formed by electrodeposition through holes in a lithographically prepared anti-reflective coating (ARC) template[44], which may be removed with a wet organic cleaning process to obtain a better view of the resulting structure[45]. Nearly at the same time, large anisotropy materials such as $L1_0$ ordered (Co, Fe)(Pd, Pt) compounds[46,47,48] were intensively studied as the next generation high density recording media due to the 20-40 times higher K_u than hexagonal Co-based alloys[49]. $L1_0$-ordered FePt/CoPt material alloyed with a third non-magnetic element X (Cr[50], Cu, Ag, Ta, B) have been also proposed[51].

Ordered equiatomic FePt is studied here due to its potential of being an outstanding advanced magnetic recording material. From the Fe-Pt phase diagram[52] (**Fig 1.28**), FePt with composition ranging from $Fe_{45}Pt_{55}$ to $Fe_{65}Pt_{35}$ exhibit two phases in the solid state: the soft magnetic A1 phase and the hard magnetic $L1_0$ ordered phase. At higher temperature, the disordered A1 phase is more stable due to a larger entropy, resulting in a lower Gibbs free energy[53]. As a chemically disordered fcc phase, A1-FePt has a lattice parameter of a = 3.82Å, with Fe and Pt atoms statistically distributed on the cubic unit cell. In bulk form, the hard magnetic $L1_0$-FePt phase can be formed below its order-disorder transformation at 1300^{o}C according to the phase diagram. Its tetragonal unit cell is characterized by a periodical arrangement of the Fe and Pt atoms in alternating (002) planes with lattice parameters a = 3.853Å, c = 3.713Å[54]. The chemical ordering of the $L1_0$ phase gives rise to a strong uniaxial anisotropy along the stacking direction[55], which originates from the spin-orbit coupling of the 3d electrons of Fe and the 5d electrons of Pt.

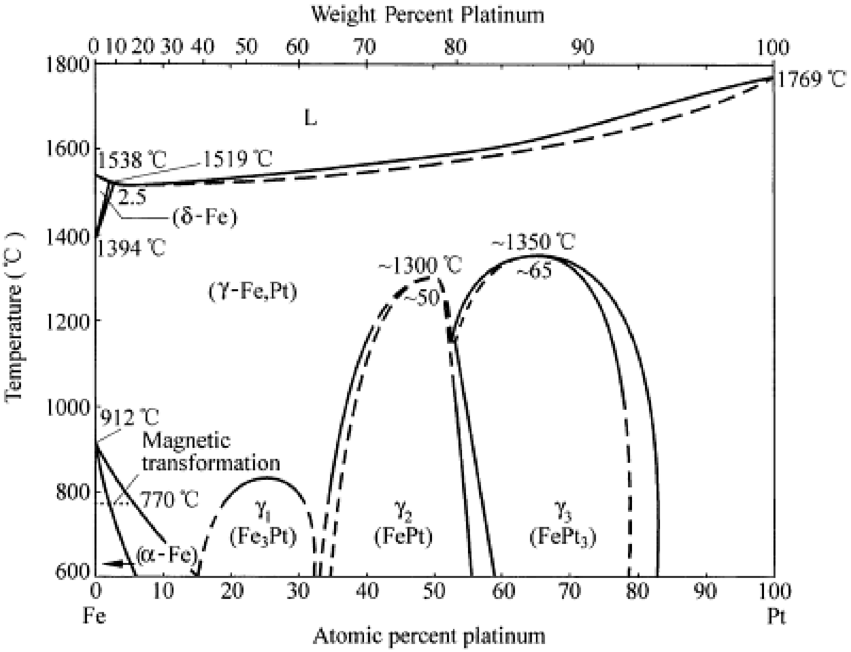

Figure 1. 29 Fe-Pt phase diagram[52]

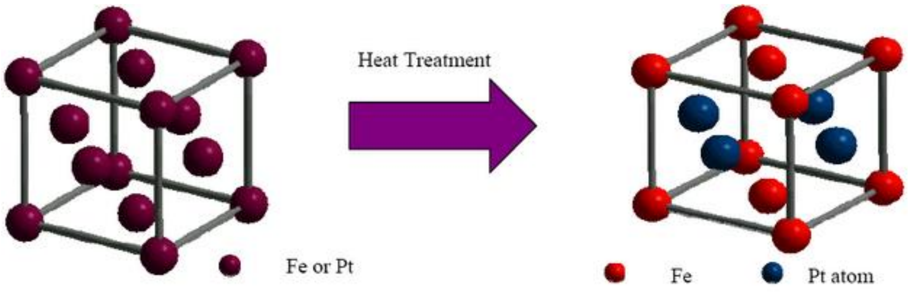

Figure 1. 30 Crystal structures of fcc and fct phase FePt (ball-and-stick models, source: University of Alabama[56])

In this thesis, patterned substrates with nanodot arrays were prepared by UV-nanoimprint lithography (UV-NIL) with high throughput. n-type Si(100) wafers coated with 80nm Ru were used as substrates; a 5nm Ta barrier layer was introduced as adhesion layer between the Si wafer and the Ru layer, preventing the interdiffusion and possibe reaction between

Ru and Si layers. It was reported that for a Ru (10nm)/Si sample annealed at 600^{o}C for 1min, the formation of Ru_2Si_3 in the film was confirmed in XRD[57]. Ru showing strong hcp (0002) orientation is chosen as diffusion barrier and serves as a seed layer for FePt electrodeposition. Besides, Ru is an inert metal with a lower electrical resistivity than that of Ta[58]. For the Ru layer, the thickness of 80nm is chosen here to ensure a columnar structure, favored for FePt electrodeposition. From Arunagitri *et al*[59], instead of being amorphous with a thickness of 5nm, the thicker Ru films (20nm) show a columnar microstructure oriented vertically with respect to Si substrate.

1.5. Overview of HAMR technology and recent research on FeNiPt

The magnetic hard disk drive (HDD) has been around for more than 50 years, but the demand for digital data storage fueled by the computer and internet revolutions over the past decades is still a strong driving force for HDDs to achieve higher areal density, larger capacities and faster performance[60]. While magnetic materials with higher anisotropy exist, their use are limited by the maximum magnetic field generated by the write head. To solve this problem, heat assisted magnetic recording (HAMR) has been proposed and is widely considered the most likely next generation HDD technology. HAMR uses magnetic materials with very high K_u by locally heating the medium with a well-focused laser beyond the Curie temperature T_C to lower its coercivity during the writing process, thus overcoming the limitations brought by the write field. Fully functional HDDs using HAMR technology have been showcased by Seagate[61], and a recent recording demonstration of 1 Tbit/in^2 is reported for HAMR recording[62].

The most promising high K_u materials for HAMR media are the $L1_0$ FePt-based thin films, including FeNiPt or FeCuPt, which provide sufficiently high K_u at reduced T_C and recording temperature. In this thesis, we study the deposition parameters of $Fe_{50-x}Ni_xPt_{50}$ ($0<x<30$) thin films, optimize the annealing conditions for significant magnetic hardening in those films, and study their potential for application in HAMR technology.

In 2002, Thiele *et al*[63] published an article regarding the temperature dependent magnetic properties of $L1_0$ $Fe_{55-x}Ni_xPt_{45}$ films, which makes FeNiPt system a highly recognized candidate for HAMR media. Magnetron co-sputtering method and MgO(100) substrate were adopted in Thiele's work to produce FeNiPt thin films. Strong temperature dependence of the anisotropy field was observed, resulting in a potentially large effective thermal field gradient, making these materials promising for HAMR application. Earlier in 1999, Li *et al*[64]. studied the magnetic behavior of intermetallic compounds FePtX (X=B, Ni) by method of magnetron sputtering and found that by adding B or Ni to FePt, the anisotropy, saturation magnetization and coercivity could be effectively reduced. In 1978, the approximate limits of the ordered phase in the Fe-Ni-Pt system at 600^{o}C were established by Stevens *et al*[65] (see **Fig 1.30**), and they were later cited in the research work of Barmak *el at*.,[66, 67] regarding the evaluation of Ni (1.6–21.5 at. %) and Cu doping on the A1 to $L1_0$ transformation in FePt films. Besides, in 2005, Yan *et al*.[68] synthesized Ni-doped $L1_0$ FePt films that were highly (001) textured and demonstrated a strong temperature dependence of coercivity and magnetization.

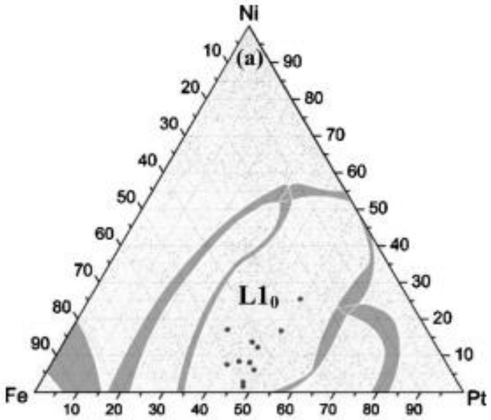

Figure 1. 31 A Fe-Ni-Pt ternary phase diagrams at 600°C, the L1$_0$ stable regions are marked[67].

Up to now, based on our knowledge, electrodeposition followed by a heat treatment remains an unexplored method for synthesizing L1$_0$ ordered FeNiPt thin films. Similar to FeNiCo alloy[69], composition of electrodeposited FeNiPt can be difficult to control due to the anomalous codeposition behavior, where there is a preferential deposition of the less noble metal. In addition, the large difference in redox potential between Pt and the 3d elements may hinder alloy formation. In Chapter 4, we discuss the development of electrolytes for FeNiPt electrodeposition and study the structure, ordering temperature, and magnetic properties of selected $Fe_xNi_{50-x}Pt_{50}$ (0<x<30) thin films.

1.6. Overview of electrodeposited permalloy $Fe_{19}Ni_{81}$ and Pt-doped $Fe_{19}Ni_{81}$ alloys

Originally, very thin permalloy laminations were used as magnetic recording head. Permalloy with a composition of $Ni_{81}Fe_{19}$ is an alloy with near-zero but negative magnetostriction[70], low anisotropy leading to a low coercivity (ideally below 1Oe), extremely high permeability (>10,000), reasonably high magnetization that can be easily made in thin-film form[16]. NiFe films have been prepared by methods such as sputtering[71], spray coating[72], electrodeposition[73], sol-gel[74] and laser ablation[75]. Among the above, electrodeposition is especially interesting due to its low cost and the ability to produce deposits with high quality. Electrodeposited $Ni_{81}Fe_{19}$ magnetic films are used in a wide range of magnetic device applications like recording heads and magnetic sensors. Numerous permalloy plating bath recipes and the roles of various additives have been investigated over the past decades[76], with a major emphasis on understanding the anomalous codeposition phenomena of Ni-Fe alloys. Here we focus on the development and characterization of a novel NiFe plating bath that could be better adapted to the codeposition with noble elements.

In this thesis, a new bath for the electrodeposition of homogeneous permalloy magnetic thin films has been developed and adjusted for Pt-doped permalloy deposition. At variance with a typical acidic permalloy electrodeposition bath, an alkaline solution is used. A large composition variation (>20%) is found by using vertical three-electrode setup for Pt-doped permalloy, and later changed to a horizontal configuration to improve the homogeneity. The effect of Ni^{2+}/Fe^{3+} ratio in the plating bath and applied field on deposit composition are explored via potentiostatic electrodeposition. Hysteresis loops for a series of samples are measured to access their magnetic properties such as coercivity, magnetization, etc.

1.7. Motivation and recent research in rare-earth free $L1_0$-FeNi materials

The choice of future permanent magnet material is mainly based on a balanced consideration of price and performance. We propose to explore a Fe-based rare-earth free magnet material that demonstrates performance much better than ferrite, and with properties equal or superior to $Nd_2Fe_{14}B$. While a large amount of Fe-based magnetic compounds show high Curie temperatures and large magnetizations that support permanent magnet behavior, their magnetic anisotropy tend to be low, which leads to a small coercivity. One strategy for introducing a strong magnetic anisotropy is to develop Fe-based materials with lower-symmetry crystal structures (typically tetragonal or hexagonal) that foster high magneto-crystalline anisotropy along a symmetry axis. In such low-symmetry crystal structures, the magnetic moment of the material may align perpendicular to the basal plane direction, providing two energy minima for the magnetization that defines the uniaxial magnetic anisotropy state.

Well-known Fe-based magnetic compounds exhibiting tetragonal structure are $L1_0$ -FePt/FePd, both demonstrating high magnetization and significant magneto-crystalline anisotropy necessary for future permanent magnet. These large anisotropy energies appear as the 4d/5d electrons of Pd or Pt participate in strong spin-orbit coupling to donate a large spin polarization, which is on the order of $0.5\mu_B$ per 4d/5d atom[33]. However, the cost of noble metal components, namely Pt and Pd, preclude their use as components in bulk permanent magnets for motors and generators and limit their application in thin-film-based devices like magnetic recording media. Similar $L1_0$ structure materials have been found in iron meteorites and named tetrataenite, also known as $L1_0$ -FeNi. The equiatomic composition FeNi, on the other hand, contains much less expensive and readily available constituents[77]. With the easy direction of magnetization lies along (001) direction, the anisotropy energy (E) of tetrataenite is approximately represented by Eq. 1.23[78],

$$E = K_1 sin^2\theta + K_2 sin^4\theta \qquad \text{Eq 1. 23}$$

Here, θ denotes the angle between the (001) direction and magnetization, anisotropy constants K_1 and K_2 are experimentally determined to be 3.2×10^6 erg/cc and 2.3×10^6 erg/cc by Néel et al. in 1964, which are remarkably large compared to disordered taenite of the same composition (K_1~10^4 erg/cc) [81]. Together with other attractive properties like nearly the same saturation magnetization M_S (1270 emu/cc)[79] as $Nd_2Fe_{14}B$, high Curie temperature T_c (~750°C [80]) and high corrosion resistance, this $L1_0$ –type FeNi demonstrates the potential of becoming an advanced permanent magnet. However, formation of $L1_0$ FeNi in the lab remains a great challenge due to the extremely low diffusion of Fe and Ni in the solid state below its order-disorder transition temperature.

In 1964, $L1_0$ -FeNi was initially synthesized by Paulevé and Néel through neutron irradiation in the presence of a magnetic field of 2.5kOe along the (100) axis at 295 °C [81]. They later estimated the order-disorder temperature to be 320°C, which was verified by Reuter *et al* [94] and is much lower than that in FePt (~1300°C), indicating that the ordering transformation in FeNi is kinetically limited on account of low atom mobility at low temperatures [77] (to better understand this limitation, it has been shown that the calculated diffusivity is around one atomic jump per 10,000 years according to Scorzelli *et al.* [82]). After that, few related publications were found over a decade till tetragonal FeNi was identified in nature in many stony, stony-iron, and iron-nickel meteorites in 1977[83]. Later in 1980, the tetragonal FeNi was optically confirmed by Clarke and Scott in as many as 59 meteorites and given the name “tetrataenite”[84]. While studies are carried out on a wide variety of meteoritic materials that contain tetrataenite (in particular, a series of papers published by Nagata *et al.*[85,86,87,88]), little effort was observed in synthesizing tetrataenite in the laboratory. With small amount of $L1_0$ –FeNi produced by electron irradiation[89,90], ion irradiation[91], mechanical alloying[92] and electroless plating[93], the preparation process and characterization methods of $L1_0$ -FeNi remain largely unexplored. In 2014, Kojima *et al.* reported that $L1_0$ -FeNi thin films prepared by alternate deposition of Fe and Ni monatomic layers showed a large magnetic anisotropy of 7.6×10^6 erg/cm^3 (95.48MGOe)[94]. Meanwhile, Lewis *et al.* published a series of papers covering work on permanent magnet materials[33, 95], characterization of tetrataenite extracted from NWA 6259 meteorite[96,**Error! Bookmark not defined.**] as well as $L1_0$ FeNi computational modeling[97]. These efforts brought $L1_0$ FeNi back as potential candidate for future permanent magnets. Here we propose to adopt electrodeposition to produce rare-earth free $L1_0$ -FeNi that exhibit equal or superior properties to $Nd_2Fe_{14}B$ for reasons below:

1). Synthesis of $L1_0$ FeNi by electroplating with subsequent heat treatment has not been reported to date in the literature, despite the fact that it is much faster (nearly ten times the deposition rate) and cheaper than electroless plating;

2). Electroplating is a simple, cost-effective method by which the stoichiometry of the FeNi alloy materials can be controlled through the applied potential;

3). Electroplating tends to produce either thin film or “bulk plate” materials with a nanocrystalline feature that is desired for generating a high coercivity.

We are particularly interested in developing a stable and low-cost electrolyte to generate FeNi alloys, investigating the ordering temperature in our Fe-Ni system, as well as characterizing corresponding magnetic properties

Before developing specific experiments, there are two more key problems to figure out: 1. What is the composition range of FeNi alloys that has the ability to demonstrate hardening after annealing; 2. at what kind of temperature should we anneal the samples. To answer these questions, further information from the Fe-Ni phase diagram is required. In 2006, Cacciamani *et al.* published a critically assessed Fe-Ni phase diagram[98] and later provided an updated version (**Fig 1.32a**) calculated based on preliminary results[99]. This phase diagram did not show phase relations below 200 °C due to the difficulty of achieving thermodynamic equilibrium at these relatively low temperatures. This diagram shows that the equilibrium $\gamma\text{-(Fe-Ni)}_{param} = \gamma\text{-(Fe-Ni)}_{ferrom} + \alpha\text{-Fe}$ occurs at about 415 °C and $\gamma\text{-(Fe-Ni)}_{ferrom}$ decomposes into $FeNi_3$ and α-Fe at around 345 °C. However, information about phases below 300°C is not clear, especially in consideration of the $L1_0$ phase. While Rossiter *et al.*[100] and Yang *et al.*[101] considered $L1_0$ -FeNi to be metastable, Reuter *et al*. reported it to be stable and proposed the Fe-Ni phase diagram based on meteoritic evidence and electron irradiation of laboratory FeNi alloys (**Fig 1.32b)**[102]. They observed a metastable asymmetrical miscibility gap below 390°C, which is caused by the presence of a tricritical point that is produced by magnetic interaction [82]. Dashed lines here show metastable extension of the miscibility gap from the tricritical point and the $L1_0$ phase is denoted as γ”, with a Ni content roughly around 46-56 wt. % (45-55% at. %) and a critical order-disorder temperature of 320 °C. Other phases are defined as follows: α is a low-Ni bcc phase, γ is fcc phase, γ_1 is a low-Ni paramagnetic fcc phase, γ_2 is a high-Ni ferromagnetic phase and γ' is ordered $FeNi_3$. Based on these two phase diagrams, we proposed to produce a series of as-plated FeNi alloys with Ni atomic percentage of 40%, 45%, 50%, 55% and 60%, and anneal them at temperatures of 280 °C, 320 °C and 360 °C to see whether $L1_0$ FeNi could be produced.

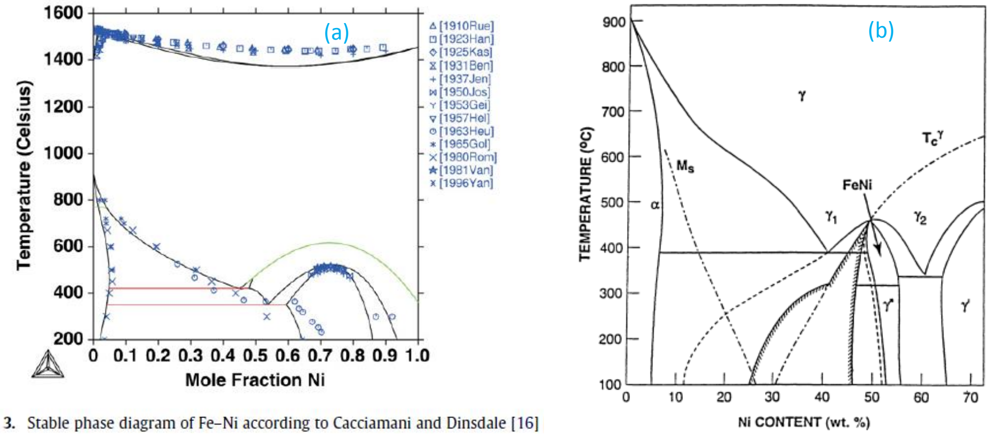

Fig. 3. Stable phase diagram of Fe–Ni according to Cacciamani and Dinsdale [16]

Figure 1. 32 Left: Fe-Ni phase diagram calculated by Cacciamani and Dinsdale in 2009; right: Fe-Ni phase diagram provided by Reuter et al. (1989)

2. The experimental set-up

2.1. Preparation of pre-patterned substrates for FePt nanodot arrays

When preparing the pre-patterned substrate for patterned media, UV-curable resin (TR-21, Toyo Gosei Co., Ltd.) was coated on the Ru-coated Si substrate and then patterned by pressing a quartz mold containing pillared structure with 150nm diameters and 150nm pitch between the pillars. The resin was then cured by UV radiation and the quartz mold was removed[103]. This part of work was done by Y. Maniwa and D. Nishiie from Professor T. Homma's group at Waseda University, Japan. Then, Ar + O_2 plasma was applied to remove residual resin at the bottom of the pores and then FePt was electrodeposited into the pores with varying thickness controlled by the applied potential and deposition time. The whole process is shown in **Fig 2.1**.

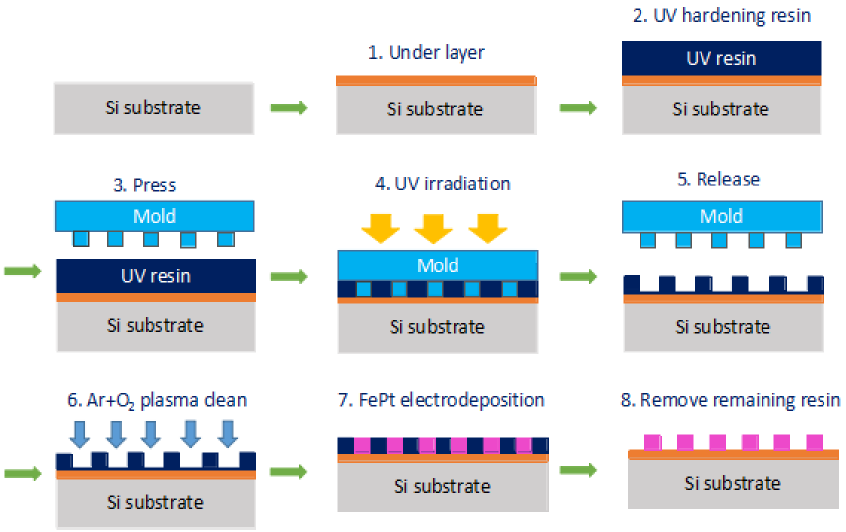

Fig 2. 1 Fabrication process of a pre-patterned substrate (courtesy of Professor T. Homma)

2.2. Sample preparation for electrodeposition

For electrodeposition of FePt nanodot arrays, pre-patterned substrates were used, otherwise, the electrodeposition process was conducted on 0.8×0.8cm^2 substrates cleaved from Si wafers, which had been previously sputtered with a (0002) oriented 80nm Ru layer on top of a 5nm Ta adhesion layer. A plate (spade) geometry for the electrode was adopted (**Fig 2.2a**), and ohmic contact was made through copper conductive tape (3M, 6.3mm W x 16.46m L, purchased from Ted Pella, Inc.) in order to connect the substrates and an aluminum bar on both sides. An adhesive tape (Kapton Polyimide Film, 3M, 25.4mm x 32.9m, purchased from Ted Pella, Inc.) was then used to mask off all the substrate except the area on which deposition was carried out and cover part of the aluminum bar that will be immersed into the solution. A simple schematic of the prepared sample for deposition is shown below in **Fig 2.2b**.

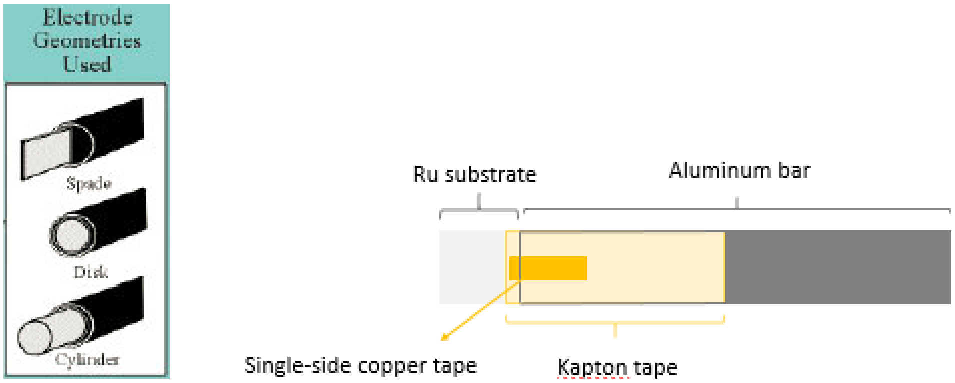

Fig 2. 2 (a) different geometries of a working electrode[104]; (b) detailed drawing of a working electrode used in this thesis

Before each experiment, the substrate was pretreated by rinsing with ultra-pure Milli-Q water (resistivity: 18.2 MΩ·cm at 25°C), dipped into a concentrated H_2SO_4 solution to remove the surface oxide, rinsed again with ultra-pure Milli-Q water to remove remaining H_2SO_4 solution, then transferred immediately to the electrodepositon cell to start the experiments.

2.3. Three-electrode setup: vertical and parallel

The electrochemical apparatus used for deposition process was an EG&G-PAR potentiostat-galvanostat Model 263. The deposition of FePt nanodot arrays and Ni-doped FePt thin films were conducted in a jacket beaker with a deposition temperature of 75^{o}C while equiatomic FeNi film deposition was carried out in a 150mL beaker at room temperature, all using a vertical three-electrode setup with a Pt mesh as the counter electrode, the sample as the working electrode and a saturated mercurous sulfate electrode as the reference electrode (mercurous sulfate electrode - $Hg/HgSO_4$, Koslow 5100P), sometimes also called SSE (+0.65V vs. SHE[105]). A schematic showing the vertical three-electrode setup for FePt deposition is displayed in **Fig 2.3**; the temperature of the solution is kept stable at 75^{o}C by connecting the jacketed beaker to a water bath circulator (Thermo Neslab, EX 7); the reference electrode is separated from the main heated water jacket by a Luggin capillary. However, to make the set-up simpler, we found that at 75^{o}C, the reference electrode can be placed directly in the solution in close proximity to the working electrode, thus avoiding the use of a salt bridge.

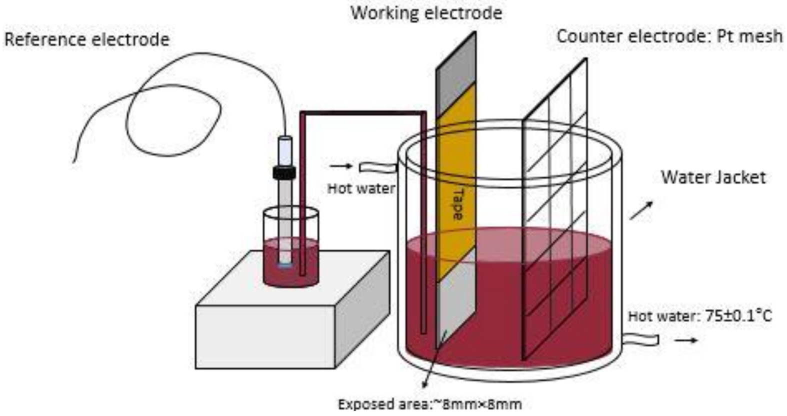

Fig 2. 3 The vertical configuration of three-electrode setup for FePt electrodeposition

The parallel configuration is applied for electrodeposition of Pt-doped FeNi alloys, in consideration of enhancing composition homogeneity (**Fig. 2.4**). More details can be found in later discussions of electrolyte preparation for Pt-doped FeNi deposition.

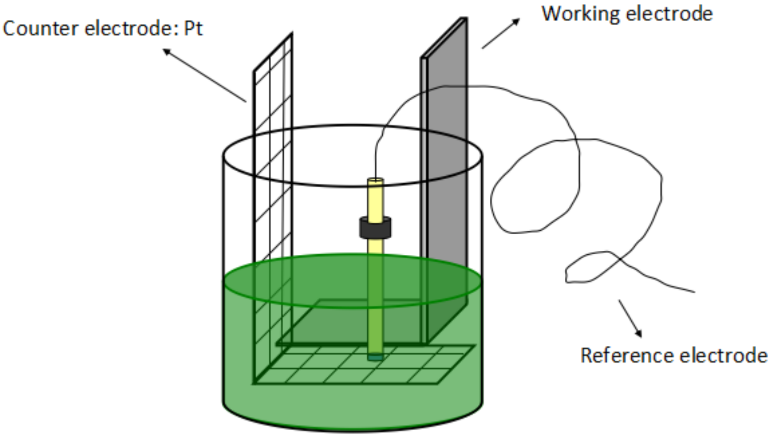

Fig 2. 4 The parallel configuration of three-electrode setup

2.4. Preparation of Pt-p-salt

$Pt(NH_3)_2(NO_2)_2$, also known as Pt-p-salt, is adopted as the Pt source for electrodeposition of FePt and Pt doped permalloy, prepared following the recipe given in the *Handbook of*

Preparative Inorganic Chemistry[106]. The starting $H_2Pt(NO_2)_4$ can be prepared from acidic H_2PtCl_6:

$$PtCl_6^{2-} + 6NO_2^- = Pt(NO_2)_4^{2-} + 2NO_2 + 6Cl^- \quad \text{Eq 2. 1}$$

The Pt-p-salt precipitates when an aqueous solution of $H_2Pt(NO_2)_4$ is treated with aqueous ammonia:

$$Pt(NO_2)_4^{2-} + 2NH_3 = [Pt(NO_2)(NH_3)_2] + 2NO_3^- \quad \text{Eq 2. 2}$$

The detailed preparation process is carried out as follows: a jacketed beaker (**Fig. 2.5**) is used to hold 100ml DI water. 1g H_2PtCl_6 and 4g $NaNO_2$ (an excess of $NaNO_2$ was used here to ensure completion of the conversion to Pt-p-salt) are added and dissolved, then the temperature of the jacketed beaker is set to and kept at 95^0C for around 9 hours till the solution turns from brown red to colorless. A 250ml Erlenmeyer flask is used to hold the colorless solution, then 4ml of 14M $NH_3 \cdot H_2O$ is added into the solution in a fume hood. The Erlenmeyer flask is sealed and kept in a refrigerator for nearly a day till a dense whitish mass of fine, needlelike crystals (Pt-p-salt) comes out of the solution. As a final step, the solution is filtered continuously with DI water, the precipitate is then dried and stored, showing a pale-yellow color.

Fig 2. 5 A commercial jacket beaker with a volume of 250mL

2.5. Solutions for electrodeposition: FePt nanodot arrays, Ni-doped FePt, permalloy & equiatomic FeNi and Pt-doped FeNi

A 100ml “background” bath was used as a basis for all the electrodeposition processes mentioned in this thesis; it contained 0.15M NH_2CH_2COOH, 0.15M $(NH_4)_2C_6H_6O_7$, 0.1M $NaNO_2$, 0.1M $(NH_4)_2SO_4$.

2.5.1. Solution for electrodeposited FePt nanodot arrays

The composition of the electrolyte for Fe-Pt deposition[13] was 50mM $Fe_2(SO_4)_3$, 15mM $Pt(NH_3)_2(NO_2)_2$ (namely, Pt-p-salt), 0.15M $(NH_4)_2C_6H_6O_7$, 0.15M NH_2CH_2COOH, 0.1M $(NH_4)_2SO_4$ and 0.1M $NaNO_2$ (**Table 2.1**). All mentioned chemicals above have been purchased and are commercially available except the Pt-p-salt. The pH and temperature of the plating bath were 8.0 and 75°C, respectively.

$NaNO_2$	0.1M
$(NH_4)_2SO_4$	0.1M
NH_2CH_2COOH, glycine	0.15M
$(NH_4)_2C_6H_6O_7$	0.15M
$Fe_2(SO_4)_3$	50mM
$Pt(NH_3)_2(NO_2)_2$	15mM
pH: 8 (by KOH), Temperature: 75°C (water bath circulator, EX 7)	

Table 2. 1 Recipe of FePt plating bath

2.5.2. Solution development for electrodeposition of Ni-doped FePt

$Fe_2(SO_4)_3$, $Pt(NH_3)_2(NO_2)_2$, and $NiSO_4$ were added as Fe, Pt, and Ni source into the background bath, successively. The pH of the electrolyte is adjusted to be 8 by using KOH and the deposition temperature is fixed at 75°C. Detailed information will be given when it comes to the discussion of electrolyte development for FeNiPt below.

2.5.3. Solution for electrodeposition of permalloy and equiatomic FeNi

For FeNi permalloy deposition, $Fe_2(SO_4)_3$ and $NiSO_4$ were added as Fe and Ni source, a series of solutions based on different Ni^{2+}/Fe^{3+} were explored. While the concentration of $NiSO_4$ was fixed at 64mM, concentration of ferric sulfate varies from 8mM, 2mM, 1.25mM to 1mM. A recipe showing all the constituents of the electrolyte is given below:

$NaNO_2$	0.1M
$(NH_4)_2SO_4$	0.1M
NH_2CH_2COOH, glycine	0.15M
$(NH_4)_2C_6H_6O_7$	0.15M
$Fe_2(SO_4)_3$	8, 2, 1.25, 1mM
$NiSO_4$	64mM
pH: 8 (adjusted using KOH), T: 25°C	

Table 2. 2 Make-up of the Fe-Ni electrolyte

2.5.4. Solution for electrodeposition of Pt-doped permalloy

With $Ni_{81}Fe_{19}$ obtained from various solution above, we choose to add 0.1mM Pt-p-salt into solution of $Ni^{2+}/Fe^{3+} = 64:4$ for Pt-doped permalloy deposition while depositing films at room temperature and keeping pH of solution at 8.

2.6. Characterization methods

The composition of the samples were measured by EDS attached to a Field Emission Scanning Electron Microscope (Joel 6700 or FEI Quanta 620). The surface morphology of the samples were observed using a Scanning Electron Microscope (Joel 6700 or FEI, Quanta 650) or AFM. Magnetic properties and magnetization states of electrodeposits were evaluated by using a Vibrating Sample Magnetometer (ADE VSM 886), while crystal structure was examined with X-ray diffraction (X'pert). Crystallographic structure was determined using X-ray diffraction (X'pert) with a Cu-K radiation. In-plane and out-of-plane hysteresis loops were measured by Vibrating Sample Magnetometer (VSM) to determine magnetic properties like saturation magnetization (M_s), coercivity (H_c) and uniaxial anisotropy (K_u) with a model of ADE VSM 886, in a magnetic field between -20kOe to 20kOe.

3. Synthesis and characterization of FePt nanodot arrays for BPM

3.1. Characterization of Fe$_{45}$Pt$_{55}$ nanodot arrays with a height of 80nm

A Fe$_{45}$Pt$_{55}$ patterned arrays was obtained by electrodeposition at the potential of -1.45V (vs. MSE) and was annealed at temperature of 450^{o}C, 550^{o}C and 650^{o}C for 1h, subsequently. Since “technical,” or extrinsic magnetic properties such as the remanence B$_{r}$ and coercivity H$_{c}$ depend on the microstructure of the magnetic materials and are therefore determined in part by the annealing process, a systematic study was carried out to investigate the structure and magnetic properties as a function of annealing temperature.

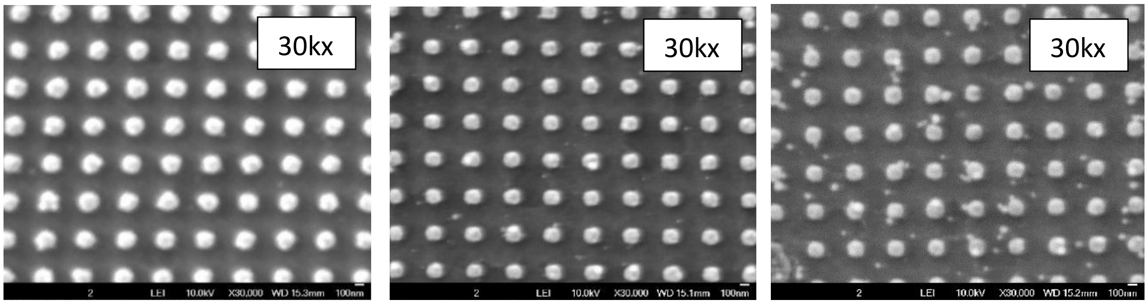

Figure 3. 1 Plan-view SEM images of FePt sample D (as-deposited, 450^{o}C, 650^{o}C) at 30kX

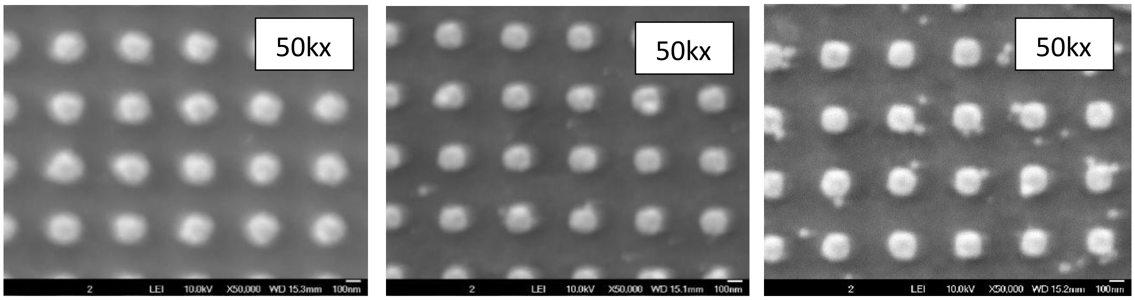

Figure 3. 2 Plan-view SEM images of FePt sample D (as-deposited, 450^{o}C, 650^{o}C) at 50kX

The surface of the as-deposited sample was observed in the SEM with a magnification of 30kX or 50kX (**Fig 3.1** and **Fig 3.2**), verifying the uniform arrangement of the nanodot arrays with 150nm diameter and 150nm pitches, which remained unaffected up to at least an annealing temperature of 650ºC.

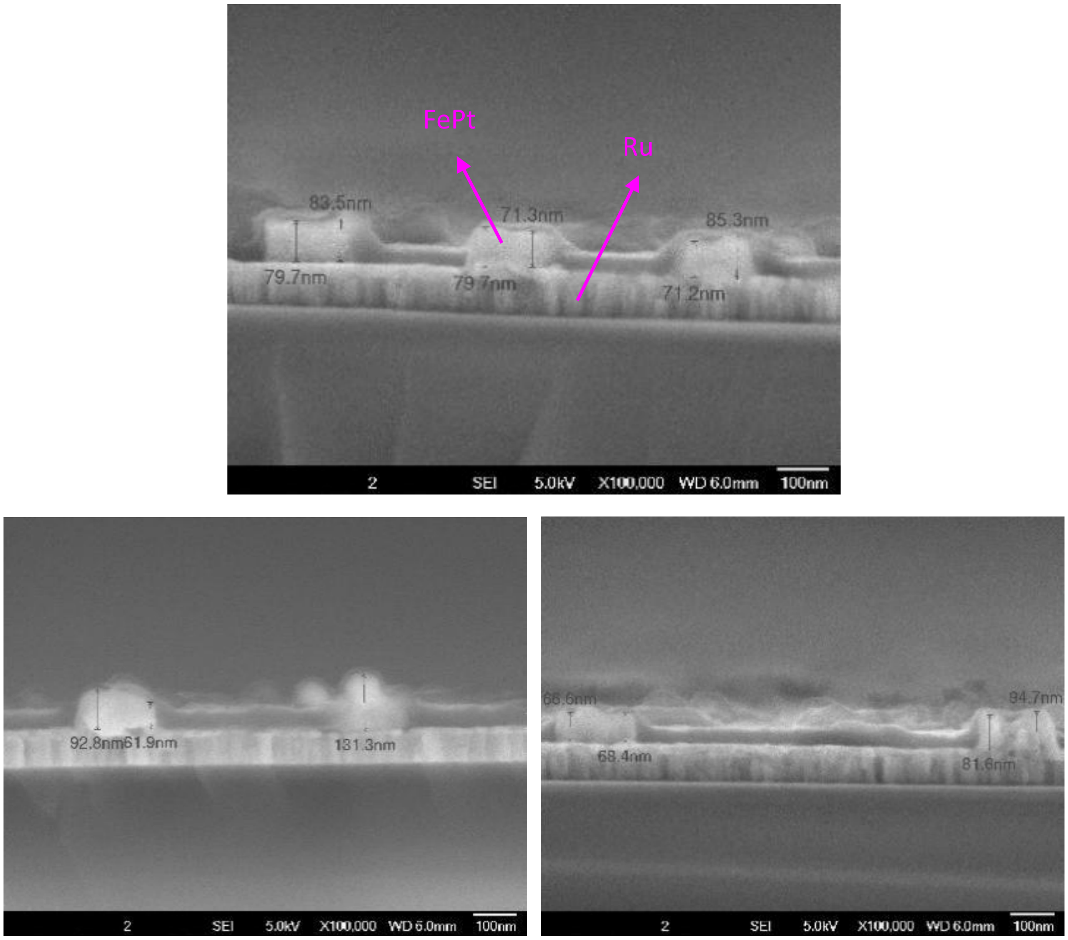

Figure 3. 3 Cross-sectional SEM images of FePt sample D after 650ºC annealing

A 80nm Ru layer with a columnar structure is clearly observed from the cross-section SEM images with a magnification of 100kx (**Fig 3.3**). The thickness of the FePt nanodots was determined from the same images and was measured to be around 80nm.

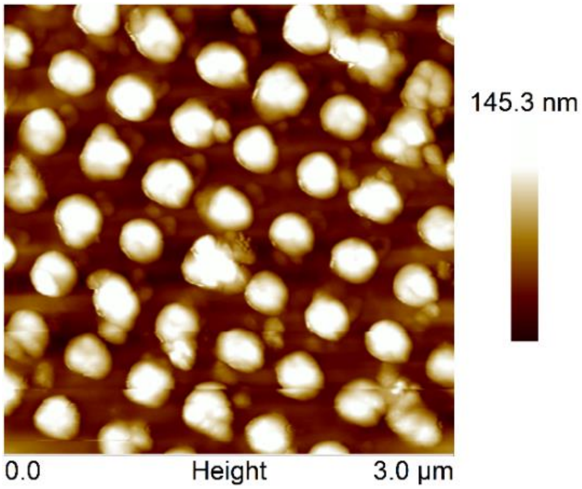

Figure 3. 4 AFM image of sample $Fe_{45}Pt_{55}$ after 650°C annealing for 1h (courtsey of Marcel Mibus)

In the AFM image (**Fig 3.4**), after 650°C annealing for 1h, the uniformity of nanodot arrays and the thickness of the nanodots was confirmed, allowing to conclude that a relatively harsh annealing process would result in limited morphological changes and would not yield to delamination.

The hysteresis loops of the as-deposited and annealed samples at different temperatures (1h) were obtained using the VSM (ADE 886), as shown below in **Fig 3.5~ 3.8**. In all hysteresis loops displayed here, the in-plane direction appeared to be the easy axis compared to the out-of-plane direction, and magnetization values did not seem to decrease dramatically with the raising of annealing temperature, suggesting limited oxidation.

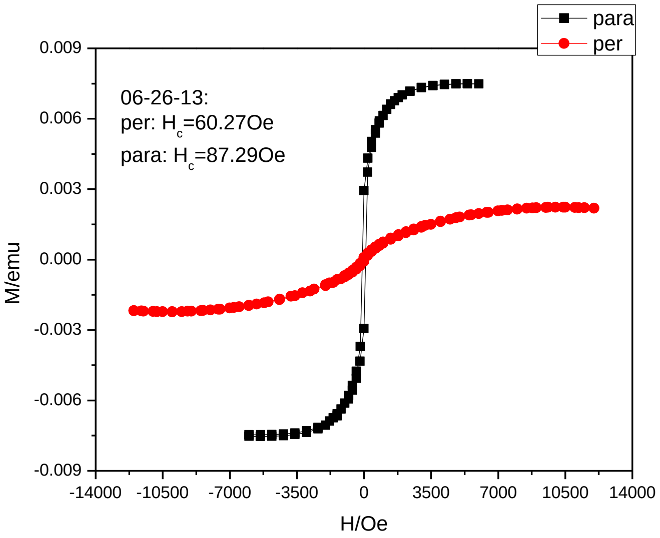

Figure 3. 5 Hysteresis loops of as-deposited FePt pattern sample D

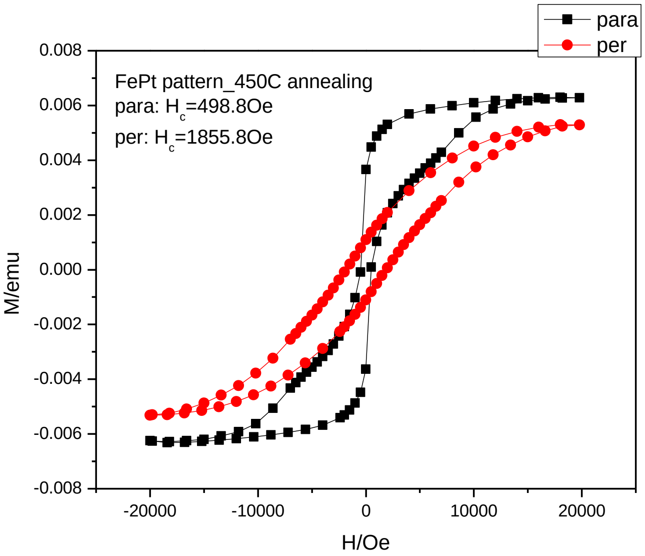

Figure 3. 6 Hysteresis loops of sample D after 450°C annealing

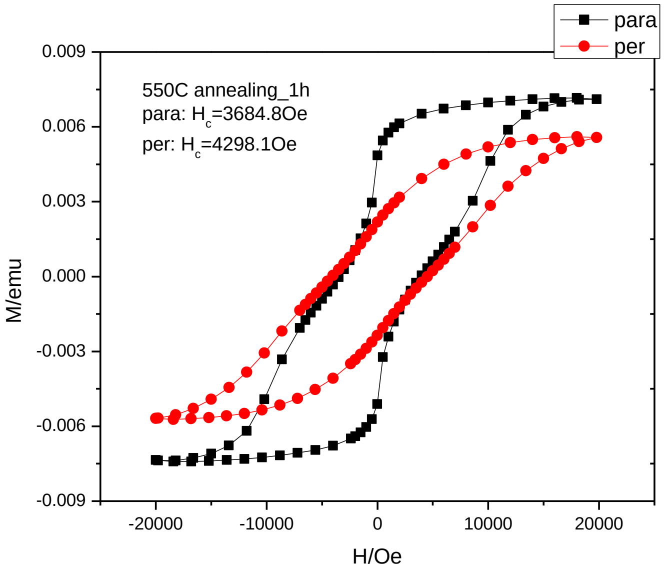

Figure 3. 7 Hysteresis loops for sample D after 550°C annealing

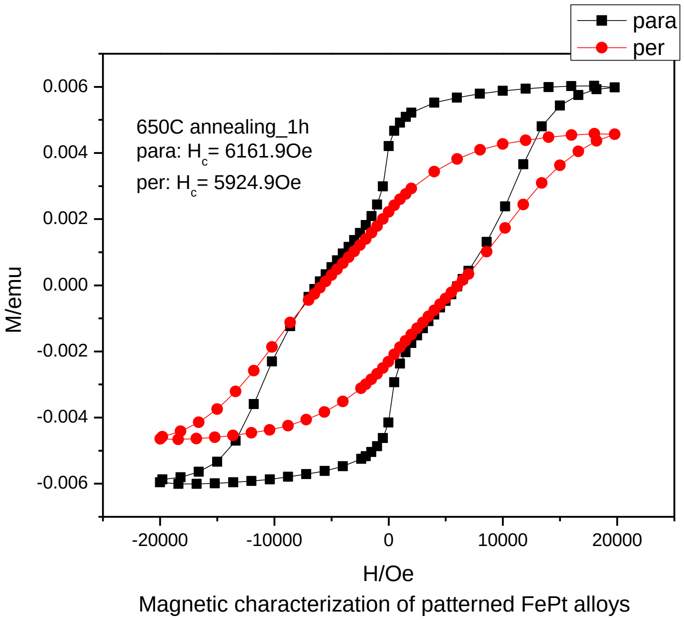

Figure 3. 8 Hysteresis loops for sample D after 650°C annealing

For better comparison, we group the magnetic loops both in the in-plane (**Fig 3.9**) and the out-of-plane directions (**Fig 3.10**).

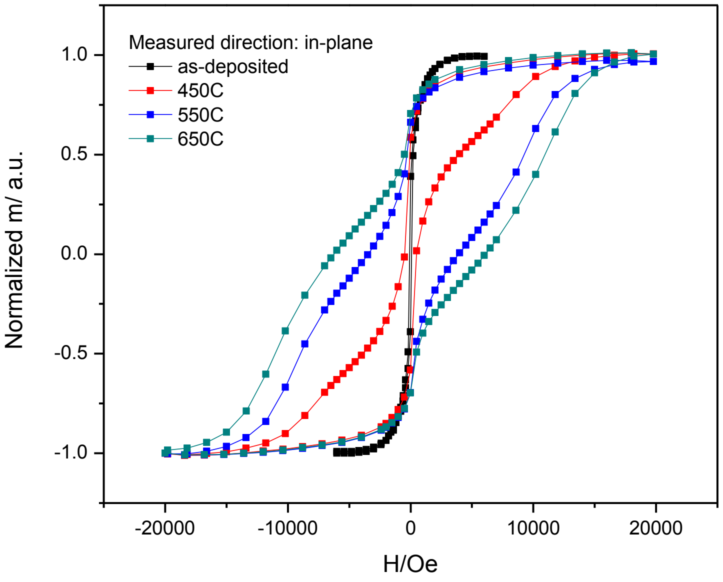

Figure 3. 9 Hysteresis loops of patterned $Fe_{45}Pt_{55}$ in the in-plane direction at different temperatures

In the in-plane direction, the as-deposited FePt patterned sample is magnetically soft, similar to as-deposited FePt thin films, suggesting the formation of disordered A1 phase[107], which was confirmed by XRD analysis (**Fig 3.11**). After annealing, the coercivity increased from less than 100 Oe in the as-deposited nanodot arrays to around 6.2kOe after 650^{o}C annealing in forming gas (5% Ar + 95% H_2) for 1h, demonstrating magnetic hardening. Since the $L1_0$ ordered phase is highly anisotropic with K_1~7×10^7 erg/cc, large coercivities are expected due to the formation of the ordered phase[108]. Therefore, the increased coercivity indicates an increased volume fraction of the $L1_0$ FePt phase transformed from the fcc FePt matrix. Furthermore, the M-H loops appeared to be the superposition of two separate loops for a soft and a hard phase where the presence of the former would reduce the coercivity; this indicates that the ordered (hard) and the disordered (soft) regions are magnetically decoupled, which is beneficial to reduce the media noise[109].

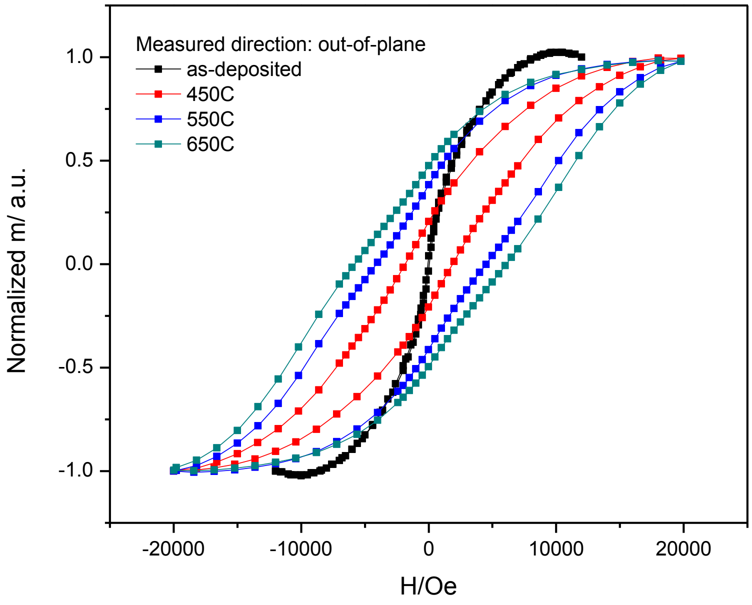

Figure 3. 10 Hysteresis loops of patterned $Fe_{45}Pt_{55}$ in the out-of-plane directions at different T

In the out-of-plane direction, the as-deposited FePt patterned sample is also magnetically soft with a coercivity around 60 Oe. All the hysteresis loops displayed a smoothly increasing magnetization loop, in contrast with the in-plane loop; this behavior can be rationalized by the fact that the soft phase in the perpendicular direction increases its magnetization slowly, due to the demagnetizing field. The coercivity increases with higher annealing temperatures, and reached a value of around 6 kOe after a 650°C annealing. The gradual increase in coercivity with heat treatment indicates the gradual transformation from a low K_u soft magnetic phase to a high K_u hard magnetic phase.

Despite no visible formation of $L1_0$ phase from XRD patterns (**Fig 3.11**), annealing results in the increasing volume of a hard phase.

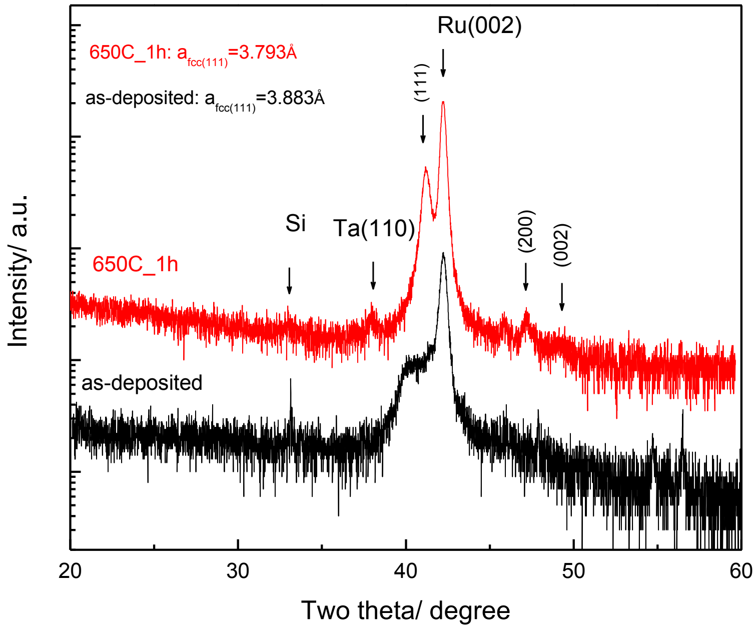

Figure 3. 11 XRD pattern for as-deposited and annealed $Fe_{45}Pt_{55}$ nanodot arrays

In the XRD of $Fe_{45}Pt_{55}$ patterned alloy, there is no evidence for ordering up to 650°C, 1 hour annealing; the alloy FePt(111) peak shifts to a higher angle (41.22° at 650°C) and the calculated lattice parameter decreases, indicating an increase in Fe content in the solid solution, perhaps related to a loss of Pt due to formation of a solid solution with Ru. The presence of a much clearer FePt(200) peak than FePt(002) peak, together with the presence of a FePt(111) peak in the 650°C annealed sample suggests that the majority of the structural domains have the tetragonal c axis in plane or inclined to the film plane[110].

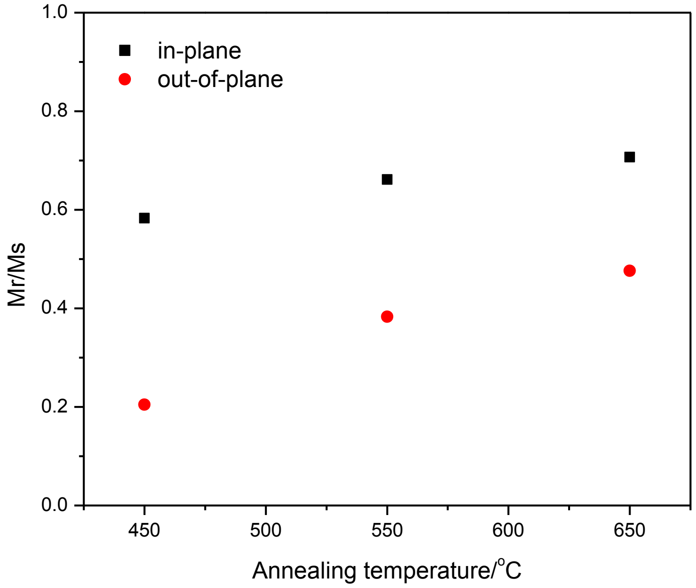

Figure 3. 12 Mr/Ms of $Fe_{45}Pt_{55}$ at different annealing temperatures in both in-plane and out-of-plane directions

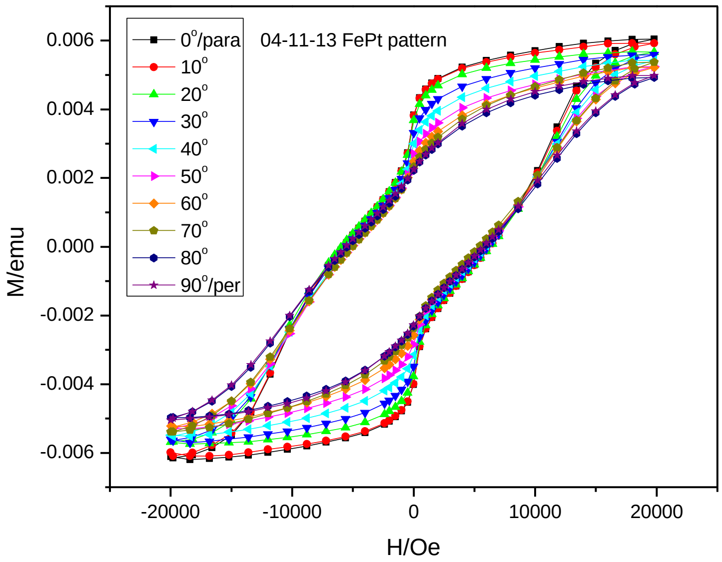

Figure 3. 13 Hysteresis loops for 650°C annealed $Fe_{45}Pt_{55}$ nanodot arrays at various angles

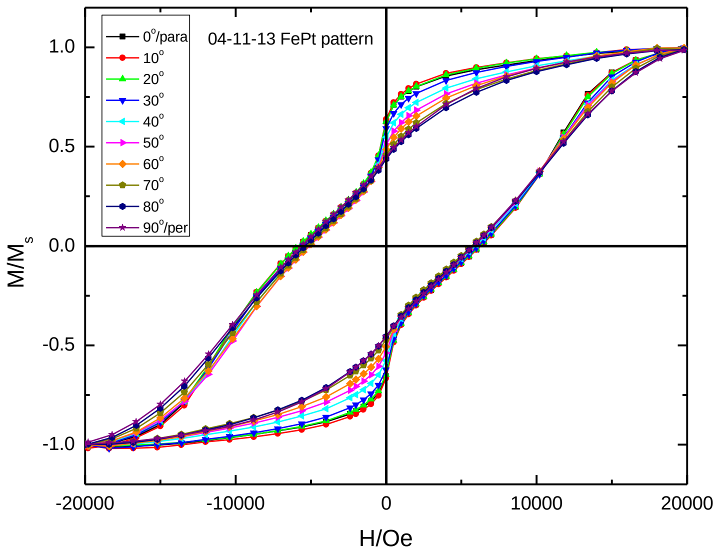

Figure 3. 14 Normalized hysteresis loops for 650°C $Fe_{45}Pt_{55}$ nanodot arrays at various angles

Angle-dependent measurement of hysteresis loops is a valuable method to gain insight into the magnetization process, allowing a direct comparison to be made with theoretical predictions about the switching field angle dependence[111]. **Fig 3.14** displays the loops measured at various angles between the easy axis in the plane of the 650°C annealed $Fe_{45}Pt_{55}$ film and the applied field, varying in the range of 0° to 90°, by 10° steps. A gradual evolution of the loops can be observed as the field direction varies from the easy in-plane to the hard out-of-plane direction. For increasing angles, all curves present similar features. In particular, demagnetization (**Fig 3.15**) develops into two distinct stages; the change in the slope close to saturation confirms that there are two phases in the patterned sample - a soft phase and a hard one.

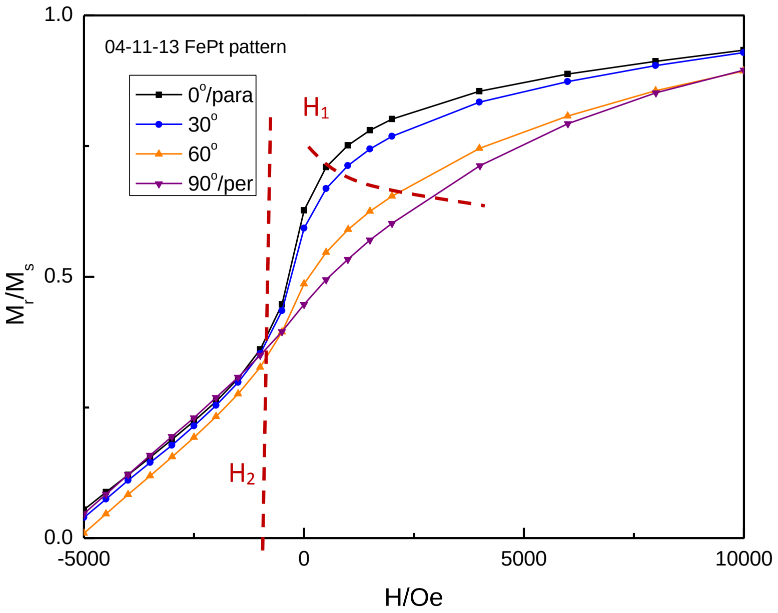

Figure 3. 15 Detailed view of the first quadrant part of selected hysteresis loops at different angles ϕ

Coming down from saturation, a progressive change in the slope is observed around a certain field H_1, followed by a faster demagnetization down to a second critical field H_2, at which dominant irreversible demagnetization processes start. While H_1 increases with tilting angle ϕ, the switching field H_2, which is extracted from each curve as the field corresponding to maximum slope changes, remains constant at about -1000Oe. It's worth noting that the coercivity H_c follows the behavior of H_2, remaining around 6 kOe over the whole range.

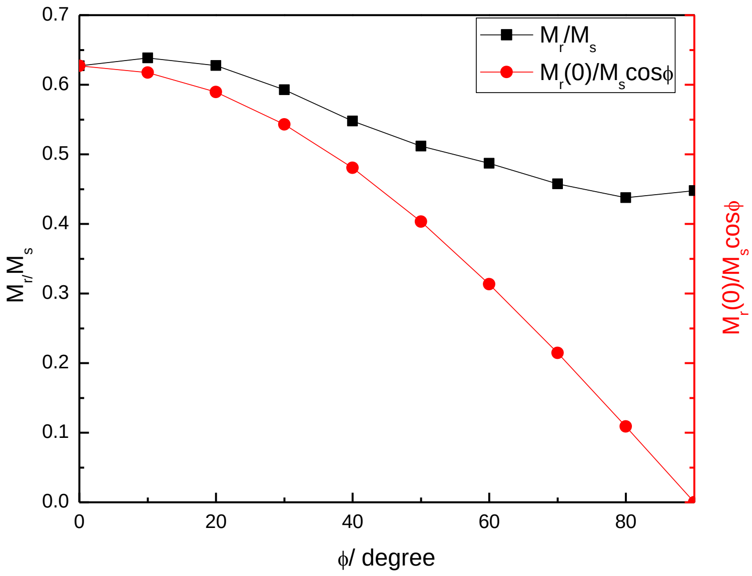

Figure 3. 16 Angular variation of the magnetization at remanence compared with $[M_r(0)/M_s]\cos\phi$

The values of M_r/M_s and $[M_r(0)/M_s]\cos\phi$ for 650°C annealed $Fe_{45}Pt_{55}$ are compared in **Fig 3.16**. At angles between 0°~20°, the measured remanent magnetization deviates from the $\cos\phi$ dependence and remains almost constant, probably due to irreversible rotations or domain patterns rearrangement[112]. From 20° to 90°, deviations from the cosine function grow with increasing tilting angle ϕ.

3.2. Deposition of FePt nanodot at a short time

Previously, we have demonstrated the successful fabrication of a $Fe_{45}Pt_{55}$ nanodot array by the electrodeposition process, along with the prepatterned substrates produced by UV-NIL. It showed a coercivity exceeding 6kOe after 650°C annealing. Here the magnetic properties of deposited FePt layer were further optimized by varying the deposition time, in consideration of varying the height of nanodot. Three FePt patterned samples are obtained at the potential of -1.39V vs. MSE with varying thickness, details can be found in **Table 3.1** below:

Sample name	Composition/ EDS at 5kV Fe : Pt	Applied potential/ V vs. MSE	Deposition time	Thickness/nm
8b	48:52	-1.39	12min	~55
8c	47:53	-1.39	15min	~70
8e	48:52	-1.39	10min	~30

Table 3. 1 Three FePt nanodot array samples deposited at -1.39V vs. MSE with varying deposition time

Thicknesses are estimated from cross-section SEM images with two degree tilted angle; in these conditions it can be very difficult to obtain high quality images after the samples are subjected to magnetic measurements and heat treatment, therefore the heights of nanodots are mostly imaged at edges or locations where defects exist and nanodots are isolated (**Fig 3.17**).

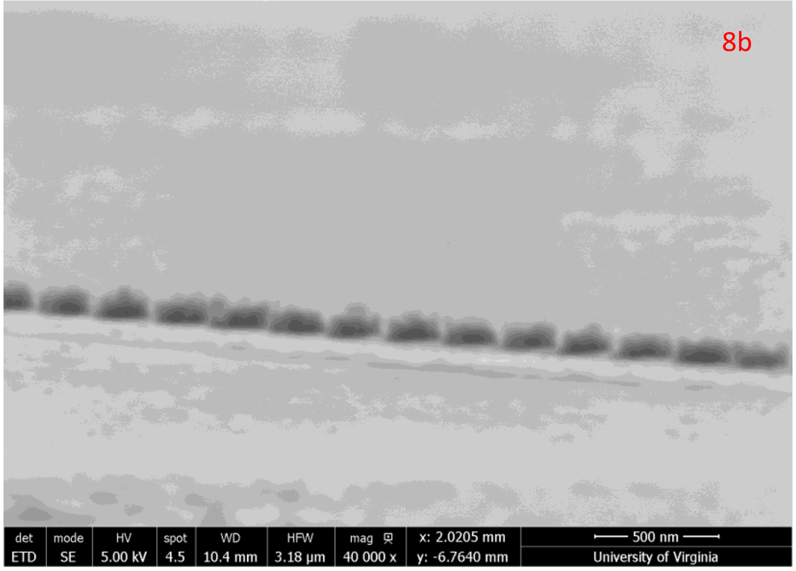

Figure 3. 17 Cross-section image of FePt nanodot arrays (sample 8b: $Fe_{52}Pt_{48}$)

The 30° tilted SEM images of samples with a magnification of 20kx are shown below:

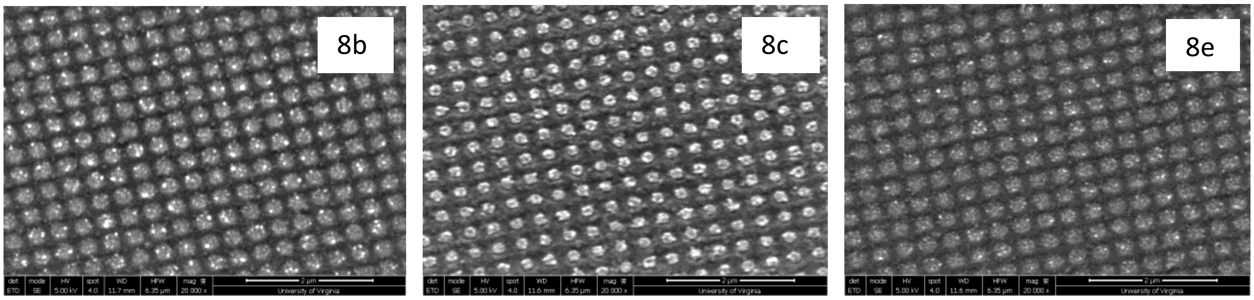

Figure 3. 18 Tilted SEM images of 650°C annealed FePt samples with a magnification of 20kx

Structural and magnetic characterization of these samples is detailed in the following.

Sample 8b:

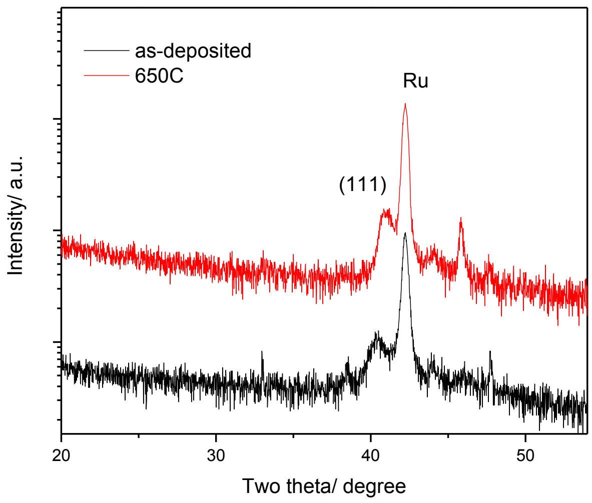

Figure 3. 19 XRD pattern for $Fe_{52}Pt_{48}$ patterned arrays before and after 650°C annealing

The only peak observed from the as-deposited sample is the FePt(111) peak, showing a strong (111) orientation. The FePt(111) peak shifts from 40.59° to 41.06° after 650°C annealing for 1h, corresponding to the shrinkage of the calculated lattice parameter from

3.847Å to 3.804Å, suggesting an increase in Fe content in the solid solution (fcc-Fe: a=0.359nm; fcc-Pt: a=0.392nm), as seen in previous samples.

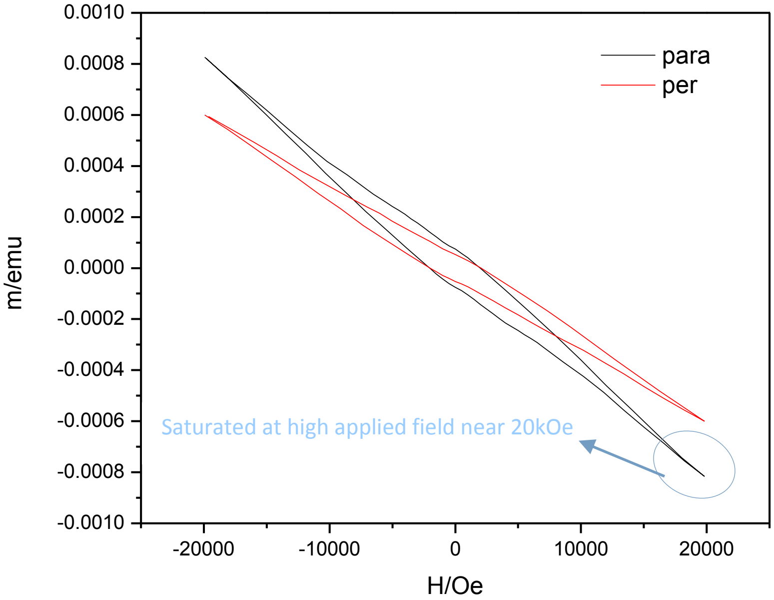

Figure 3. 20 Original hysteresis loop for $Fe_{52}Pt_{48}$ patterned arrays after 650°C annealing

As the deposition time was shortened, the height of the nanodot arrays was expected to be lower. More importantly, the sample area we used here was rather small, leading to a very small volume of the magnetic array and to a signal showing a low overall moment (**Fig 3.20**). For the VSM measurement of low moment samples (either caused by a small sample volume or a large sample with extremely low magnetization) here, the problem we need to consider is the accuracy of measurement. In the FePt nanodot arrays, the substrate and the sample holder display diamagnetic behavior, and this diamagnetism dominates the hysteresis curve at high magnetic field[113]. To get true hysteresis loop for the sample, it is necessary to subtract the signal from the substrate and sample holder from the overall signal, and **Fig 3.21** represents the final result here. Note that these corrections may lead to significant errors.

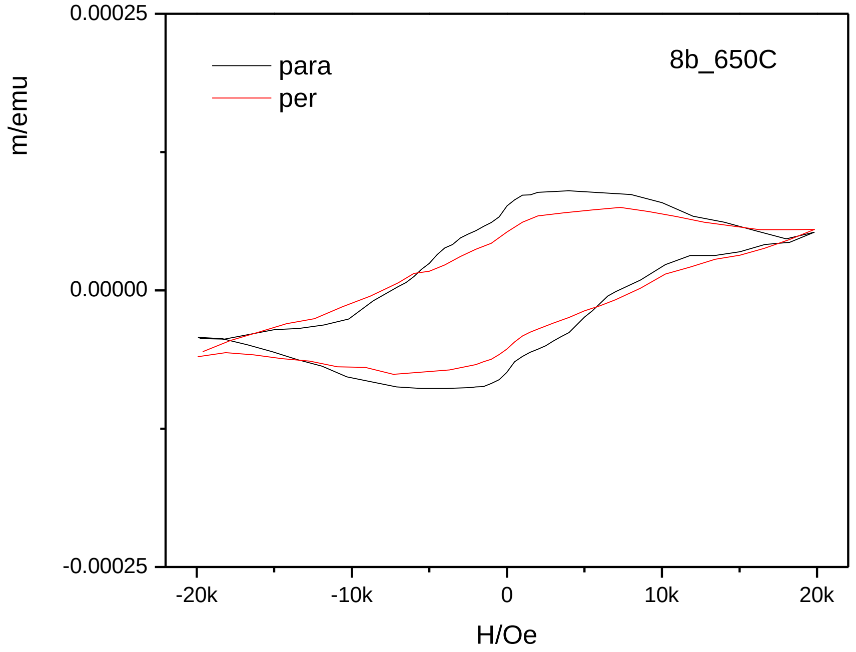

Figure 3. 21 Hysteresis loop for $Fe_{56}Pt_{44}$ patterned arrays after 650°C annealing

In the parallel direction, the sample was saturated with a maximum field of 20kOe (roughly the field limit for non-cryogenic commercial VSMs), however, in the perpendicular direction, saturation was not reached at 20kOe, which means that when a field larger than 20kOe is applied, probably a larger saturation moment and coercivity for this sample would be obtained to reflect more accurate information about this sample. In this curve, the coercivity is estimated to be 7.3kOe in the parallel direction and 8.2kOe in perpendicular direction.

Sample 8c:

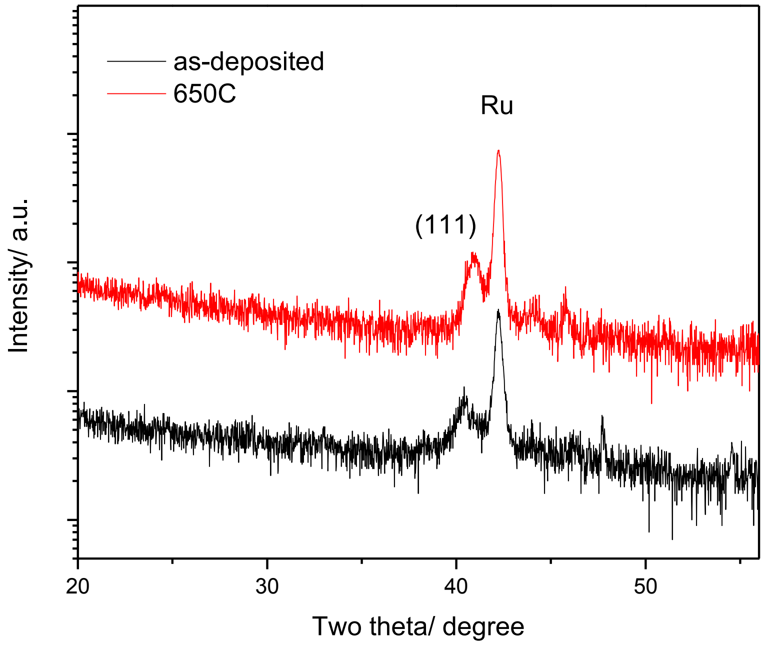

Figure 3. 22 XRD pattern for $Fe_{56}Pt_{44}$ patterned arrays before and after 650^{o}C annealing

After 650^{o}C annealing for 1h, the FePt(111) peak shifts from 40.46^o to 40.95^o corresponding to the shrinkage of the lattice parameter from 3.858Å to 3.814Å.

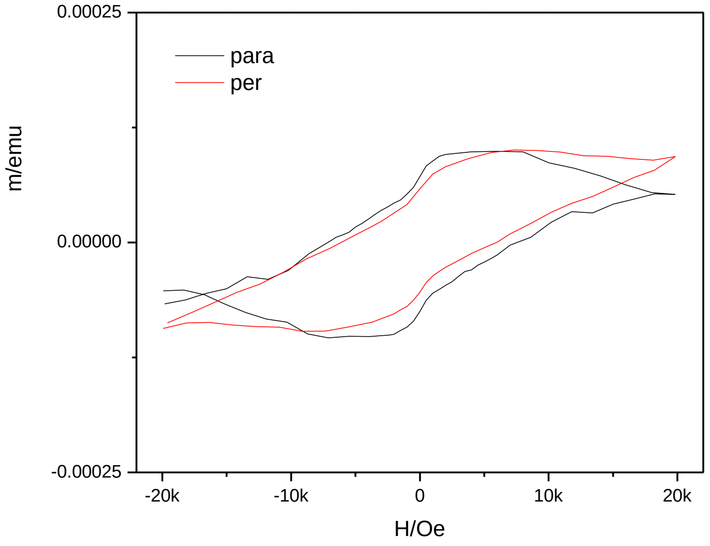

Figure 3. 23 Hysteresis loop for $Fe_{51}Pt_{49}$ patterned arrays after 650°C annealing

The coercivity was estimated as above by correcting for the sample holder, obtaining 7.4kOe in the parallel direction and 6kOe in the perpendicular direction.

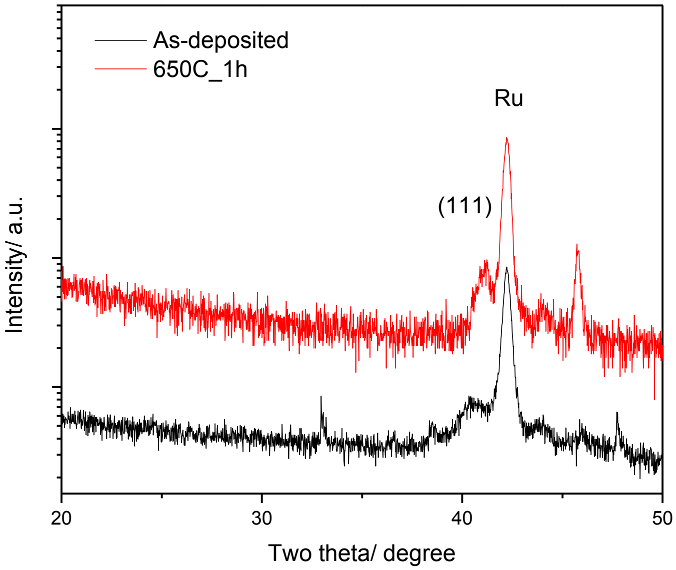

Figure 3. 24 XRD pattern for $Fe_{51}Pt_{49}$ patterned arrays before and after 650°C annealing

After 650°C annealing for 1h, the FePt(111) peak shifts from 40.73° to 41.14° , corresponding to the shrinkage of the lattice parameter from 3.841Å to 3.797Å.

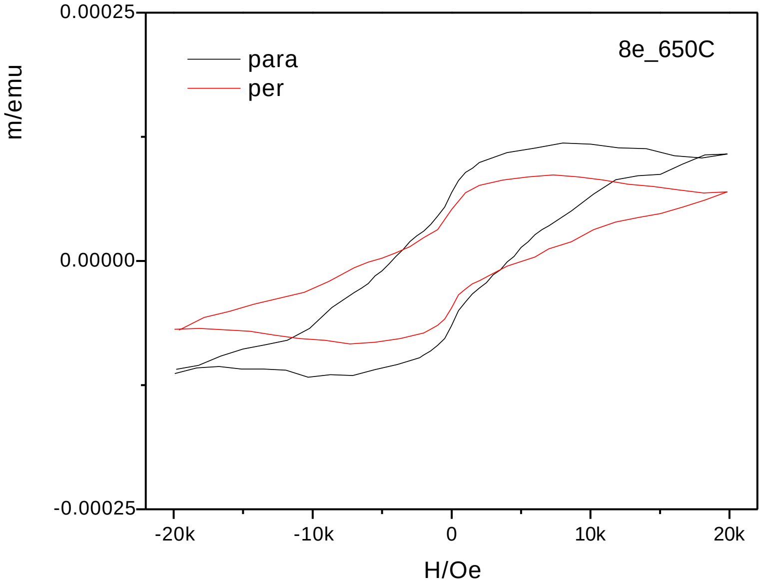

Figure 3. 25 Hysteresis loop for $Fe_{51}Pt_{49}$ patterned arrays after 650°C annealing

The coercivity was estimated to be 4.2kOe in the parallel direction and 5.4kOe in the perpendicular direction.

To conclude, the properties of this set of patterned samples are summarized in **Table 3.2**:

Applied Potential V vs. MSE	Composition (EDS) Fe: Pt	Thickness/ nm	Lattice Constant	Lattice Constant_650°C	Hc,para _650°C	Hc,per _650°C
-1.39	48:52	~55	3.847	3.804	7.3Oe	8.2kOe
-1.39	47:52	~70	3.858	3.814	7.4kOe	6.0kOe
-1.39	48:52	~30	3.841	3.797	4.2kOe	5.4kOe

Table 3. 2 Properties of FePt nanodot arrays with different heights

The increase in coercivity could due to a first approximation be related to the thickness, as should be expected in a first order phase transition such as that between fcc and $L1_0$ phase. However, the expected trend is not observed; this is probably due to errors related to the correction of the hysteresis loop shape.

3.3. Deposition of FePt nanodot at a longer time

In the previous session, we compared and discussed the structure and magnetic properties of three FePt patterned samples deposited within 15min, all the nanodot arrays displayed significant magnetic hardening upon heat treatment at 650°C. Here we described patterned FePt samples with longer deposition time and reported their structure and magnetic property dependence on different annealing temperatures. First, two FePt patterned sample were deposited at -1.42V vs. MSE for 3000s (E1) and for 2500s (E2).

Sample Name	Applied Potential V vs. MSE	Deposition time/s	Composition (EDS) Fe: Pt	Thickness /nm
E1	-1.42	3000	51:49	~200
E2	-1.42	2500	51:49	~160

Table 3. 3 Properties of FePt nanodot arrays samples (E1 and E2) with different heights

Plane view of as-deposited FePt samples are shown below (**Fig 3.26**) with a magnification of 40kx.

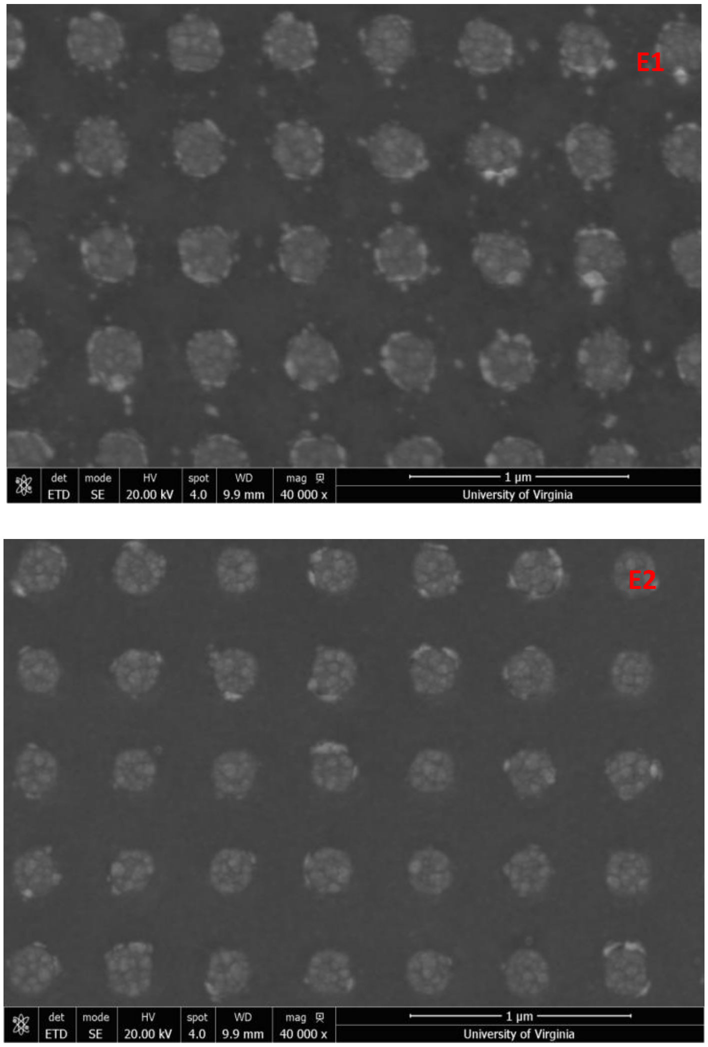

Figure 3. 26 Plane view of as-deposited FePt samples (E1 and E2)

Fig 3.27 shows plane view and 45° tilted SEM images of 400°C annealed samples:

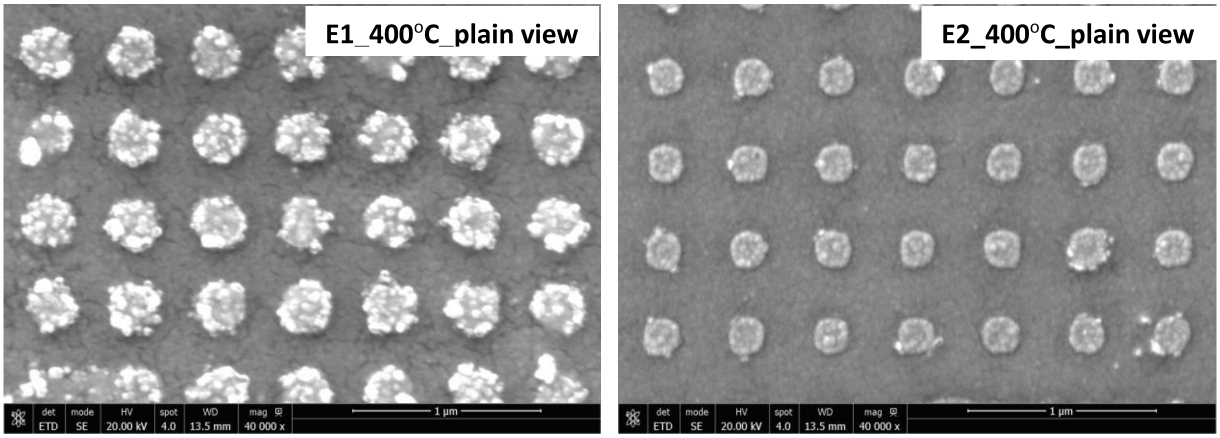

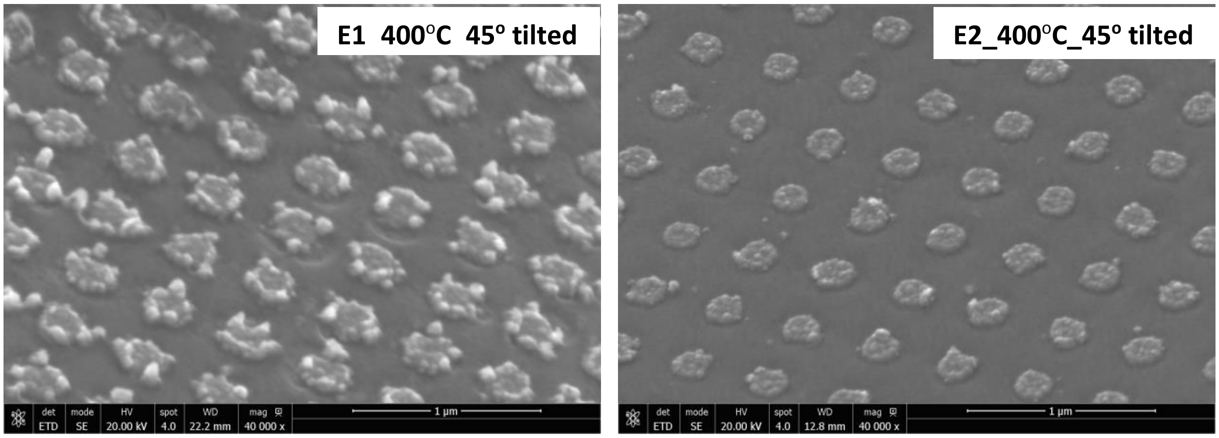

Figure 3. 27 Plane view and 45° tilted SEM images of 400°C annealed FePt patterned samples.

Fig 3.28 shows plane view and 45° tilted SEM images of 750°C annealed samples:

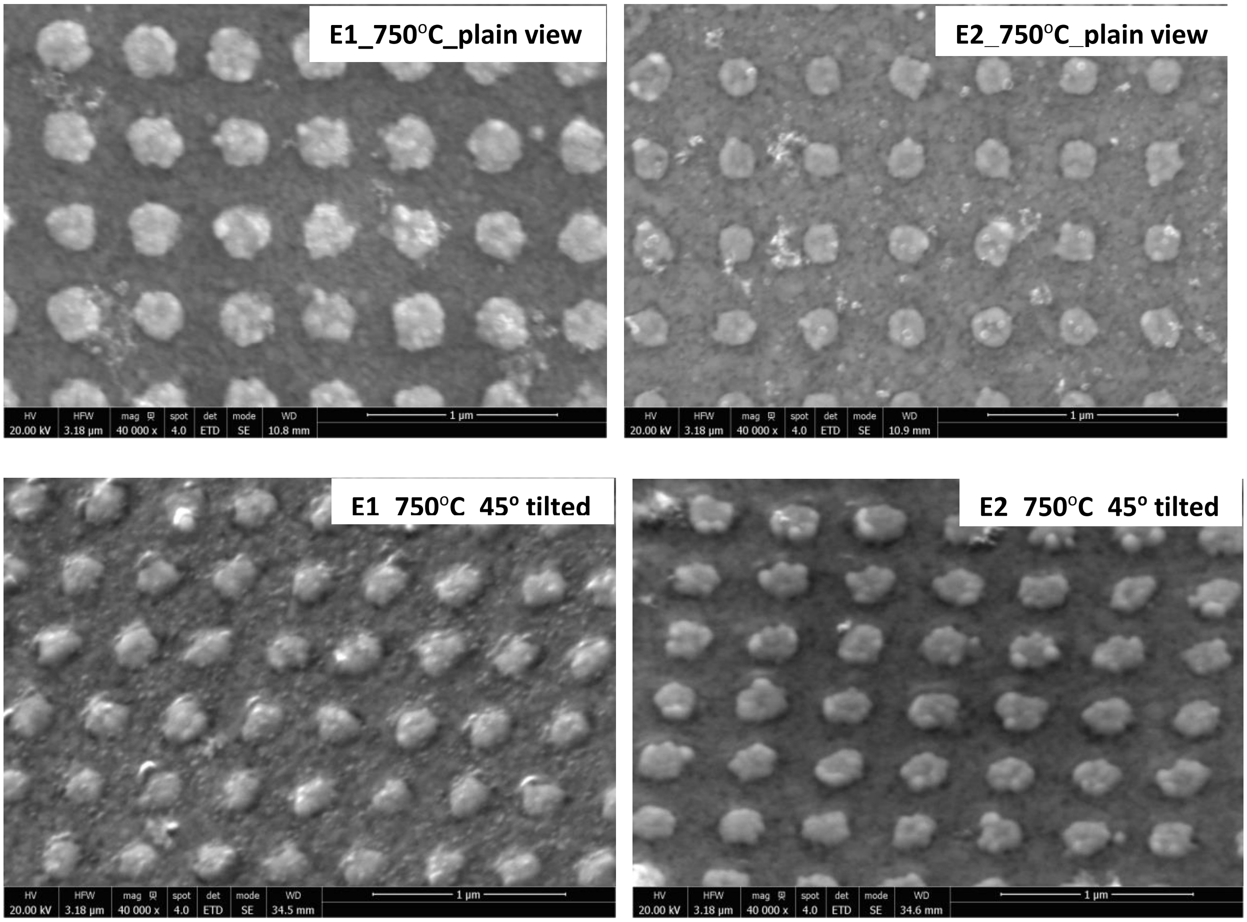

Figure 3. 28 Plane view and 45° tilted SEM images of 750°C annealed FePt patterned samples.

From this series of SEM images (**Fig 3.26-3.28**), we find that both as-deposited samples (E1 and E2) exhibit a granular morphology that develops in distinct particulates upon annealing.

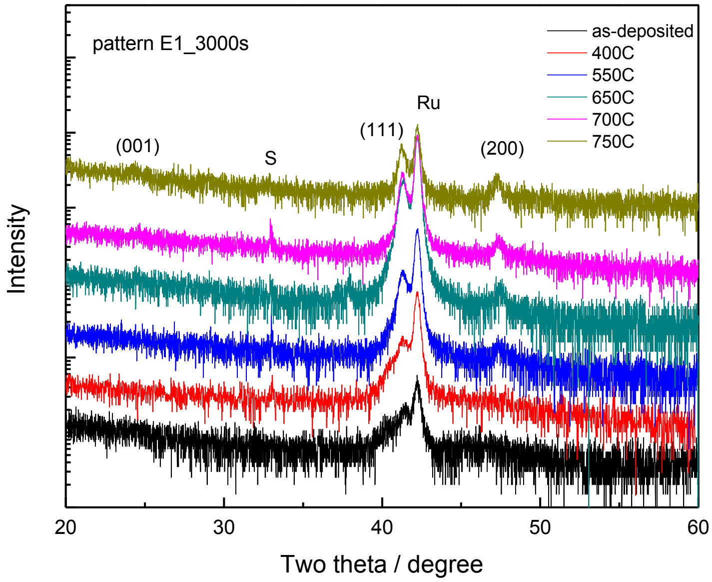

Figure 3. 29 XRD pattern for as-deposited and annealed FePt patterned sample E1

The XRD patterns for as-deposited and low temperature annealed (400°C) FePt nanodot arrays (**Fig 3.29**) show a shoulder near the FePt(111) peak, which was identified to be Pt(111). Pt is fcc with a (111) preferred orientation and a lattice constant of 3.92Å, close to that of the $L1_0$ FePt. The mismatch between FePt and Pt is so small (1.6%) that FePt would grow well with Pt(111) to yield a single FePt(111) peak[114], which was confirmed in XRD patterns at/above 550°C annealing. Other changes are observed: (i) the intensity of the (111) peak increases, evidenced from the increase of its relative intensity with respect to the nearby Ru (0002) from the substrate upon/beyond 450°C annealing for 1h, (ii) FePt(200) peak appeared upon annealing at 550°C for 0.5h, and the FePt (001) peak was detected after annealing at 650°C for 0.5h. The progressive formation of distinct grains is the likely cause for the gradual disappearance of the magnetic anisotropy[108], as observed in **Fig 3.30**. VSM measurements showed almost identical hysteresis loops in the in-plane and out-of-plane directions of sample E1 upon heat treatment at 750°C for 0.5 hours.

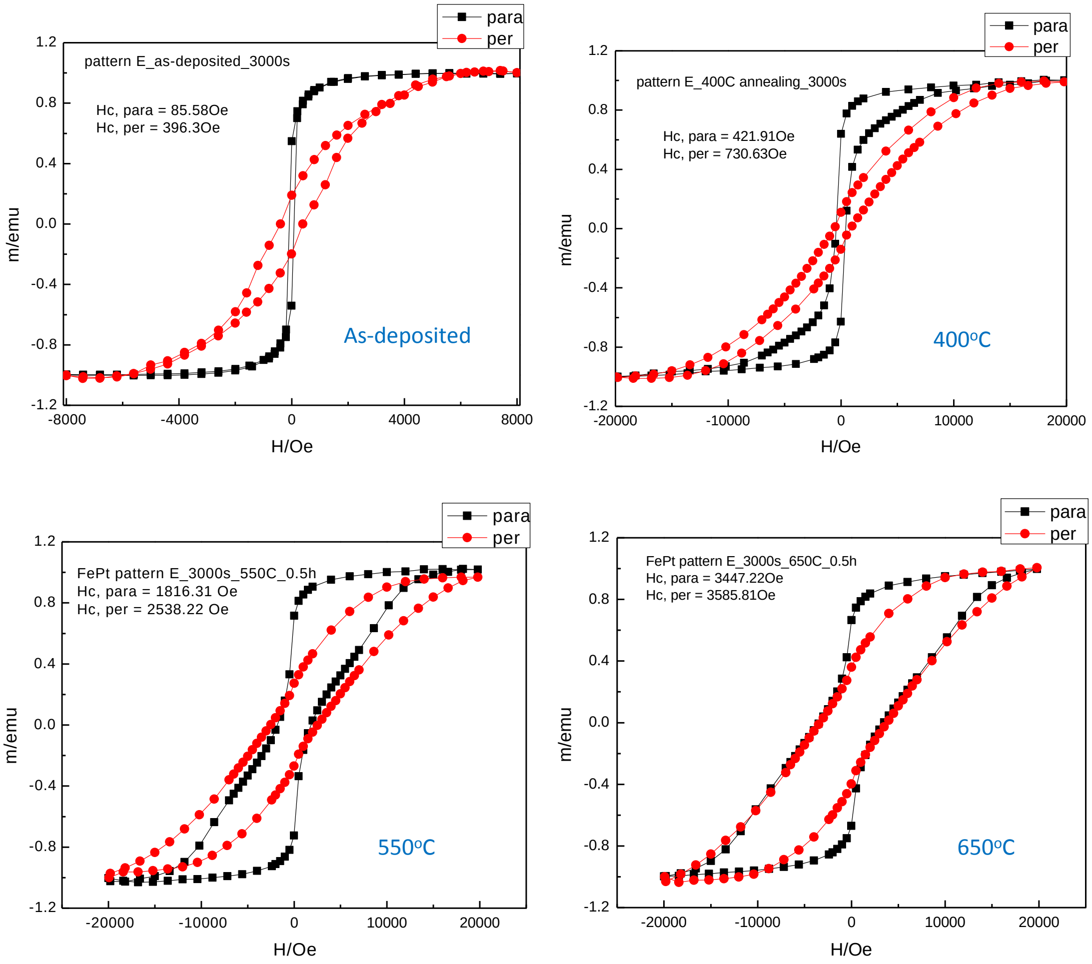

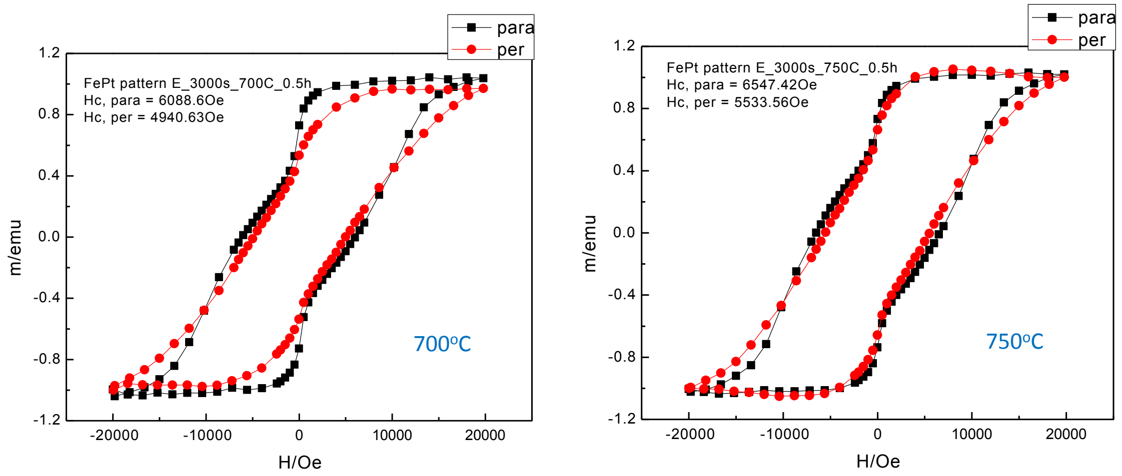

Figure 3. 30 Hysteresis loops of as-deposited and annealed FePt patterned sample E1

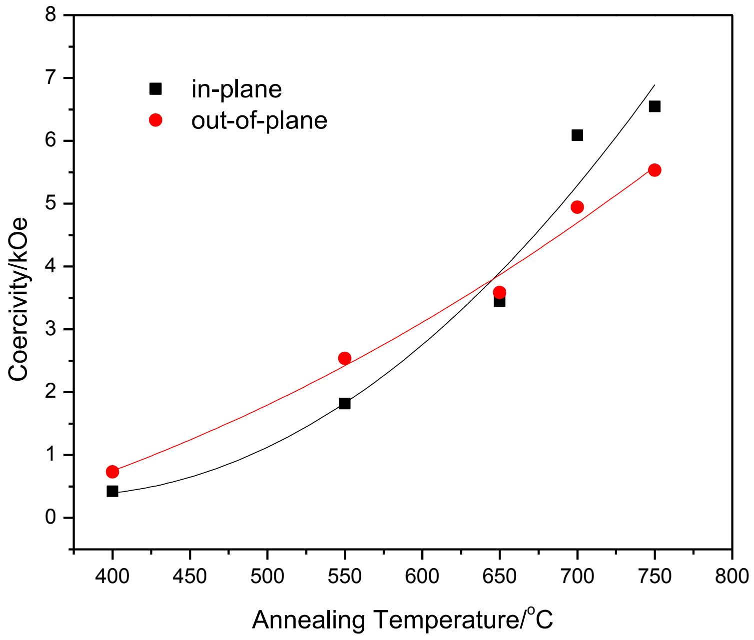

Figure 3. 31 Dependence of H_c on the annealing temperature for FePt patterned sample E1

The curves of **Fig 3.31** shows in-plane (H_{in}) and out-of-plane (H_{out}) coercivity vs. annealing temperature for sample E1. Below 650^{o}C annealing, H_{in} is smaller than the H_{out}, however, above 650^{o}C annealing, H_{in} exceeded H_{out}, which may be related to the appearance of a stronger FePt(200) peak. The difference in magnetic properties upon annealing at high temperature is, however, minimal.

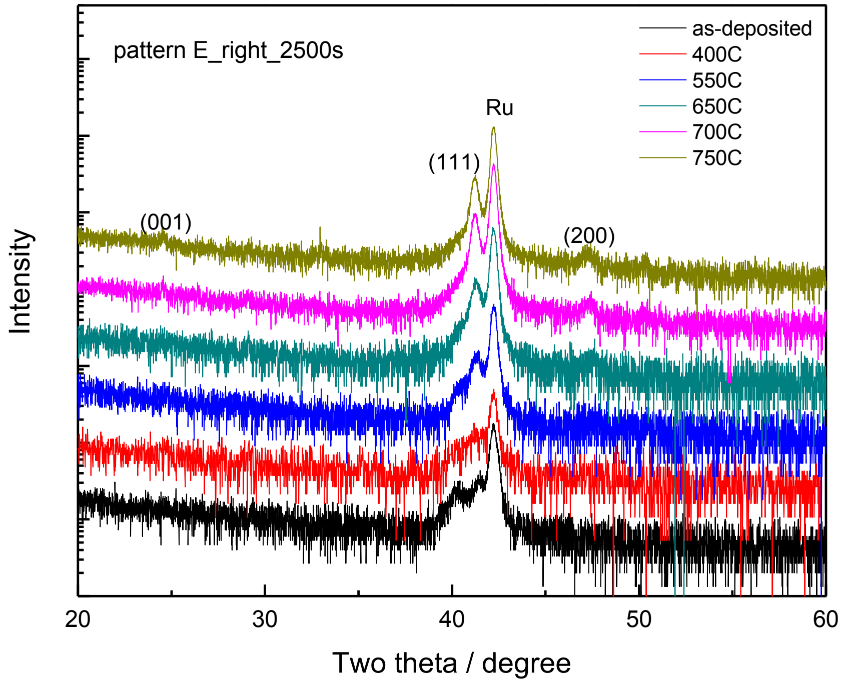

Figure 3. 32 XRD pattern for as-deposited and annealed FePt patterned sample E2

The XRD patterns (Fig **3.32**) for as-deposited FePt showed an apparent Pt (111) peak besides the FePt (111). Upon 400/550°C annealing for 0.5h, the Pt(111) peak disappeared and the XRD pattern yielded a single FePt(111) peak. FePt(200) peak appeared at 700°C, and a slight peak of FePt (001) peak was observed a the same time. The coercivity increases with annealing temperature (**Fig 3.33**) but decreases after 700°C annealing; this behavior can be rationalized considering the annealing of defects such as antiphase boundaries, thus decreasing the density of pinning sites. Additional pinning sites could also be located at the boundaries between fcc and fct phases or at planar defects[115].

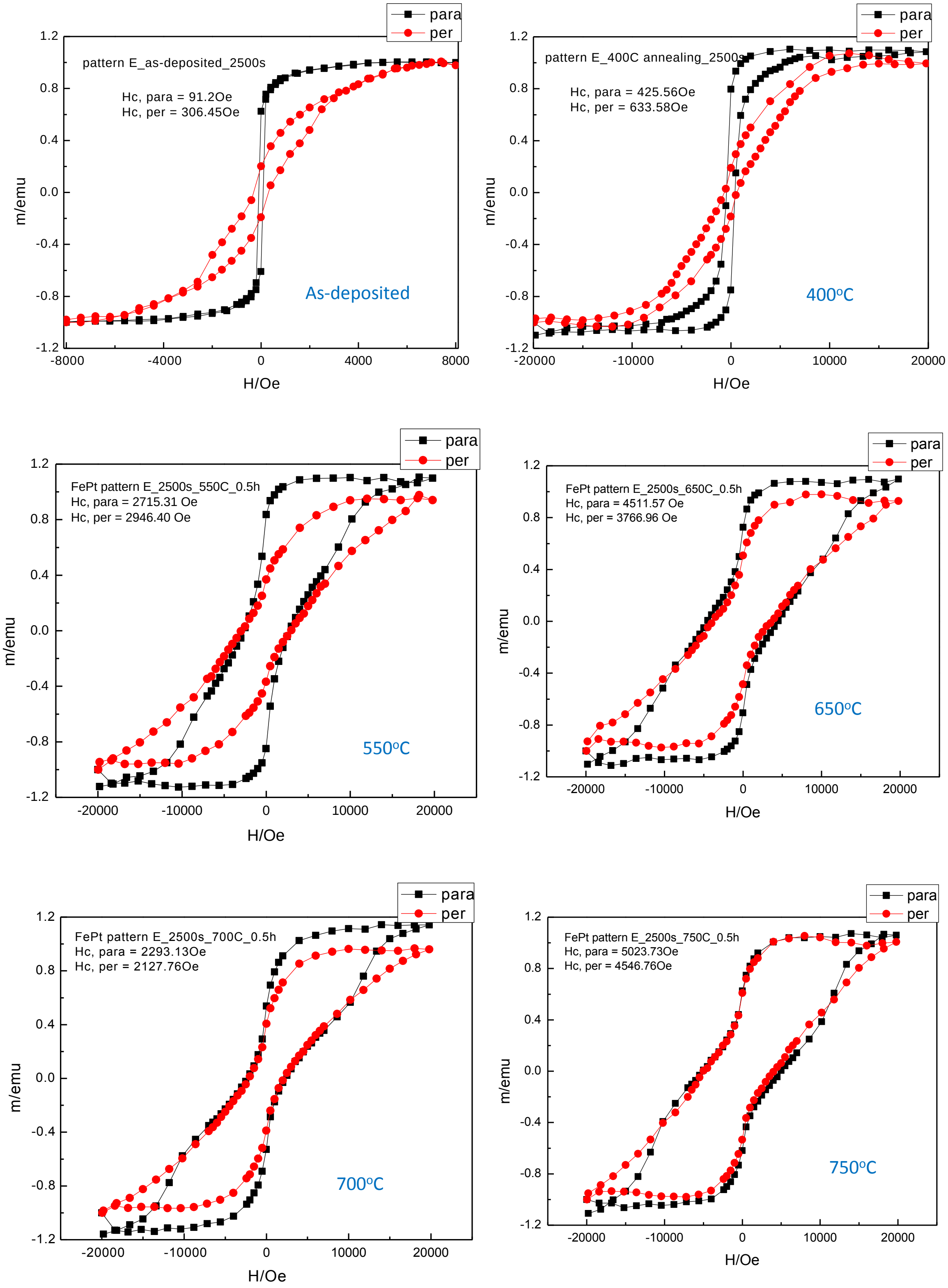

Figure 3. 33 Hysteresis loops for as-deposited and annealed FePt patterned sample E2

From **Fig 3.30** and **Fig 3.33**, both sample E1 and E2 display similar loops, probably related to both samples exhibiting the same preferred FePt(111) orientation[114].

Another two FePt patterned samples (D1 and D2) were electrodeposited at the potential of -1.46V vs. MSE for 2000s and 1000s, respectively (**Table 3.4**), and later were by accident heat treated at 850°C for 10min.

Sample Name	Applied Potential V vs. MSE	Deposition time/s	Composition (EDS) Fe: Pt	Area/cm^2	Thickness /nm
D1	-1.46	2000	48:52	0.48	~150
D2	-1.46	1000	46:54	0.38	~80

Table 3. 4 Deposition conditions, composition and thickness of two FePt samples (D1 and D2)

Given the area of each sample, we can study the relationship between the current density *i* and the deposition time t for both sample D1 and D2 (**Fig 3.34**). This *i*-t response is comprised of two parts: the current owing to the charging of the double-layer and the subsequent part owing to the electron transfer reaction. Current density for sample D1 is slightly higher than that of D2, which might be the reason for a slightly higher Fe content in sample D1 than D2. The morphology of sample D1 and D2 after deposition is shown in **Fig 3.35** and **Fig 3.36**, respectively.

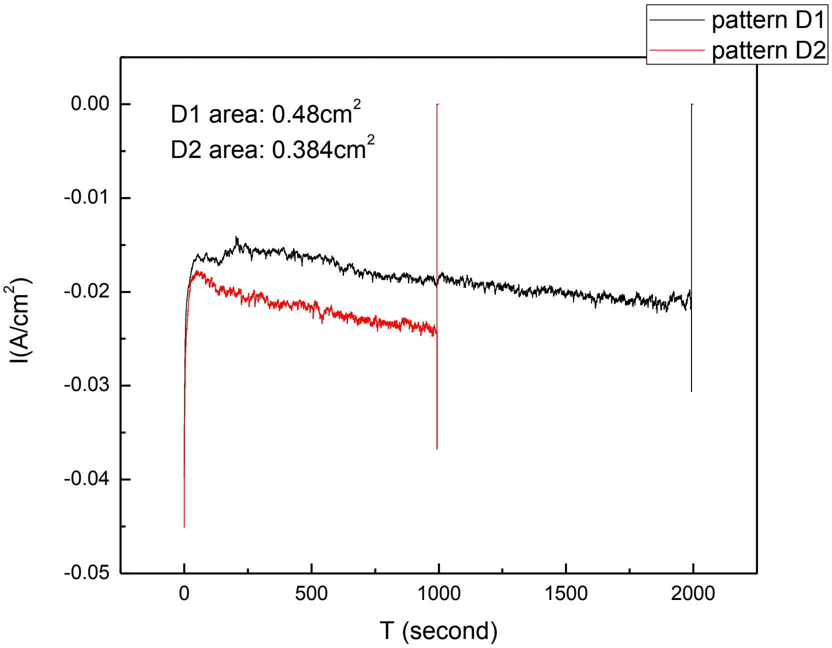

Figure 3. 34 Current density vs. deposition time for sampe D1 and D2

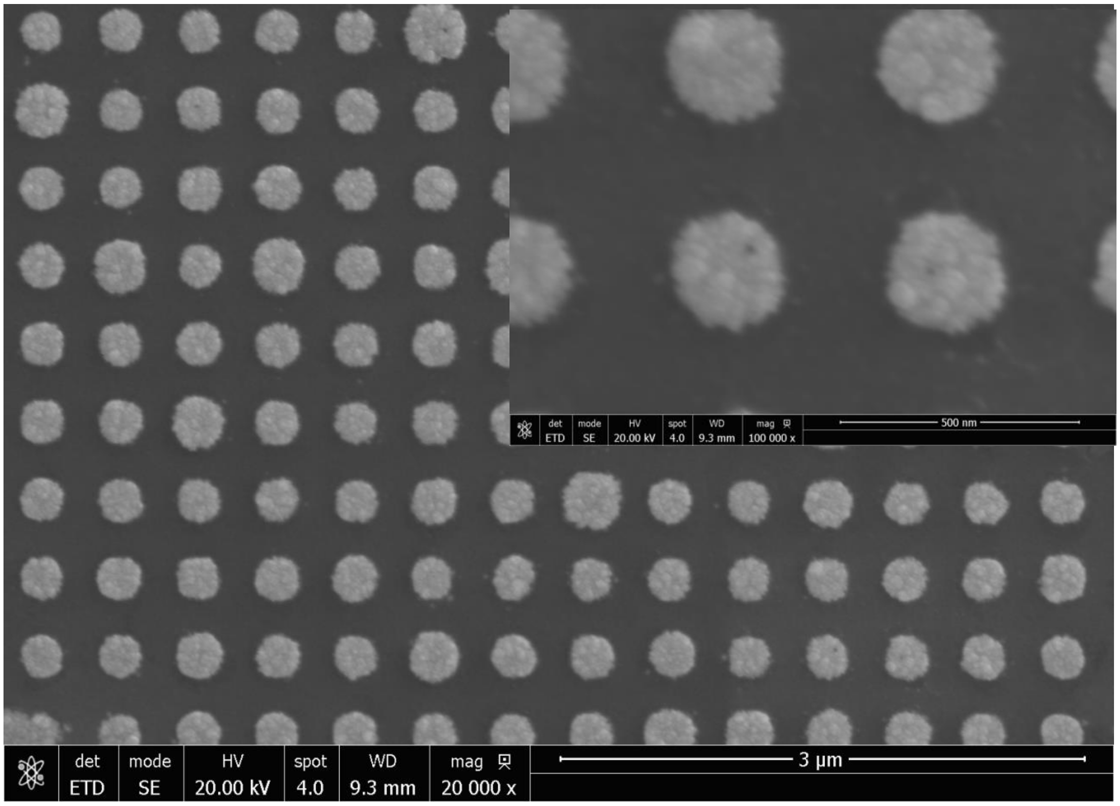

Figure 3. 35 Plane view of as-deposited FePt sample D1 with a magnification of 20kx (insert is a 100kx)

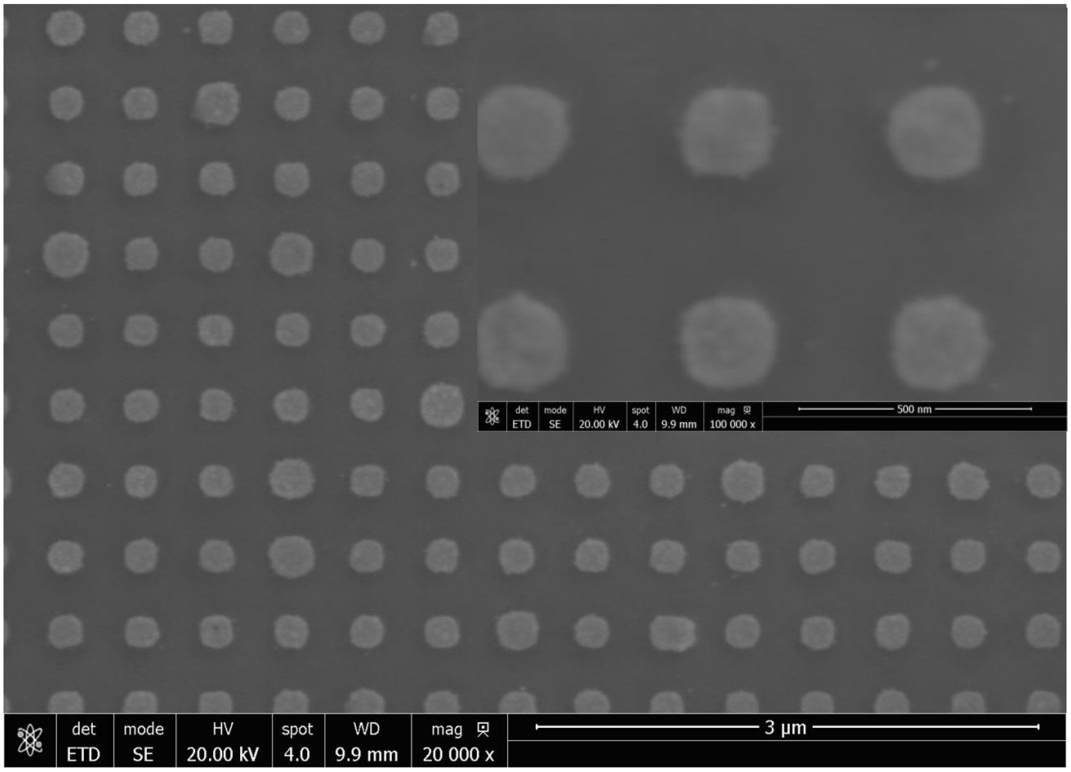

Figure 3. 36 Plane view of as-deposited FePt sample D2 with a magnification of 20kx (insert is a 100kx)

Fig 3.37 report the morphology of $Fe_{48}Pt_{52}$ nanodot arrays (D1) after annealing at 850°C; note the clear deviation from a cylindrical shape in the tilted SEM image, probably due to the tendency for minimization of the surface area.

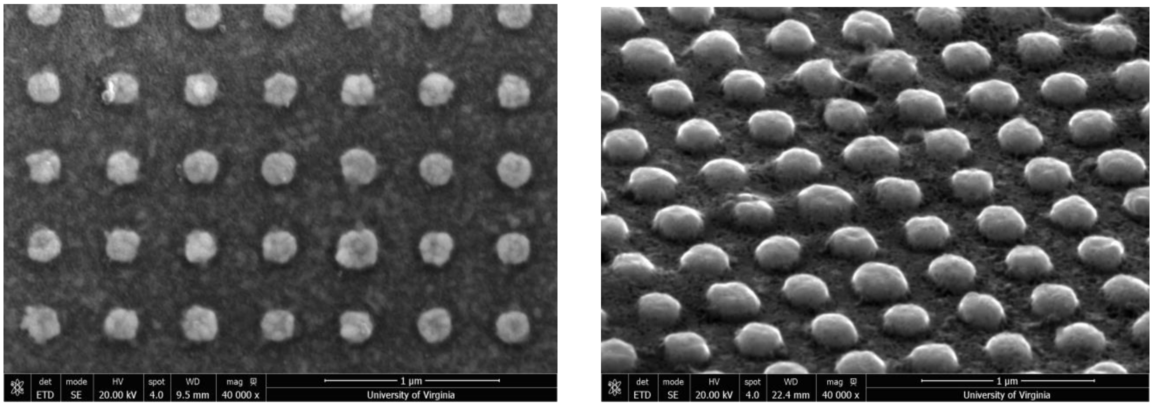

Figure 3. 37 SEM image (left) and tilted SEM image (right, tilt angle 60°) of 850°C annealed sample D1: $Fe_{48}Pt_{52}$

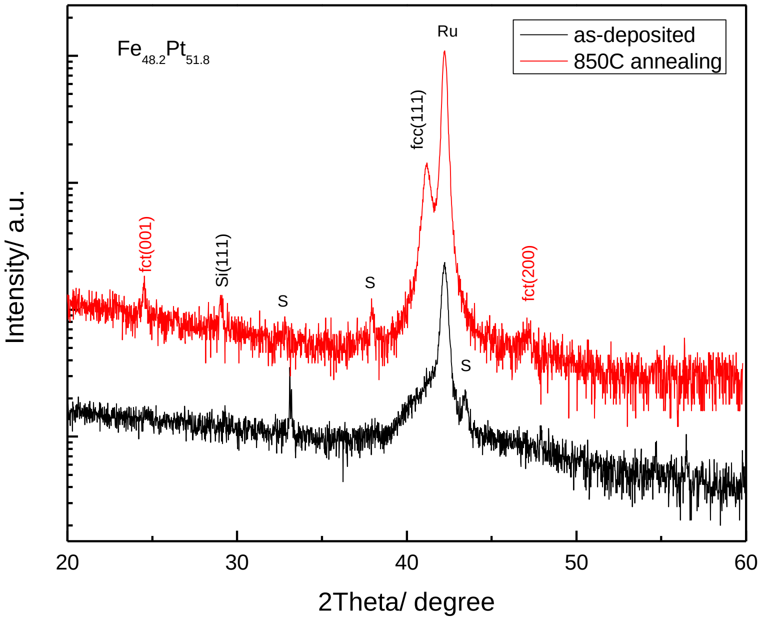

Figure 3. 38 XRD pattern for sample $Fe_{48}Pt_{52}$ before and after 850°C annealing

XRD patterns for sample D1 is shown in Fig **3.38**. In the as-deposited film, no apparent peak from the alloy material is identified, consistent with the results from previous studies within the group[116]: in the as-deposited state, FePt films are either unoriented or present a preferred (111) orientation[117]. After 850°C annealing for 10min, a strong FePt(111) peak as well as a weak (200) peak appeared, and the appearance of the (001) peak indicated the formation of $L1_0$ phase, which leads to a high coercivity of 6.8kOe in the in-plane direction and 5.9kOe in the out-of-plane direction (**Fig 3.39**).

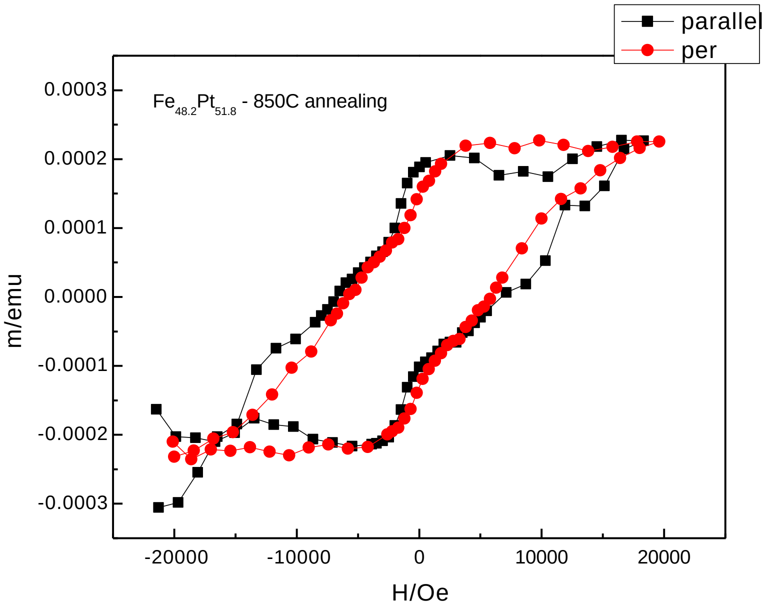

Figure 3. 39 Hysteresis loops for sample $Fe_{48}Pt_{52}$ before and after 850°C annealing

Fig 3.40 reports the morphology of sample D2 after annealing at 850°C; the average height of the nanodot arrays here is around half of sample D2, corresponding to its shortened deposition time (2000s for D1 and 1000s for D2).

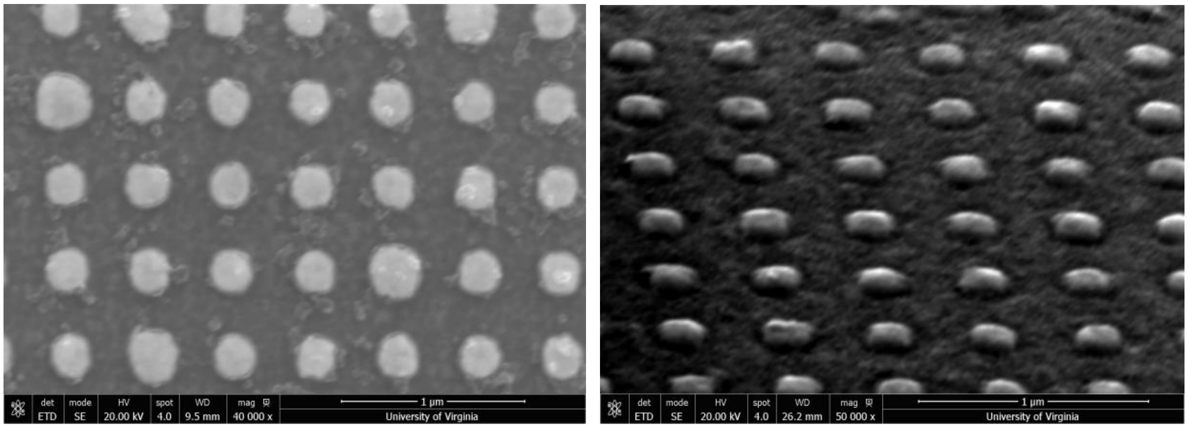

Figure 3. 40 SEM image (left) and tilted SEM image (right, tilt angle 60°) of 800°C annealed sample D2 - $Fe_{46}Pt_{54}$

The EDS mapping of patterned sample D2 is shown in **Fig 3.41**. Obviously, Fe and Pt are uniformly distributed throughout the nanodot arrays.

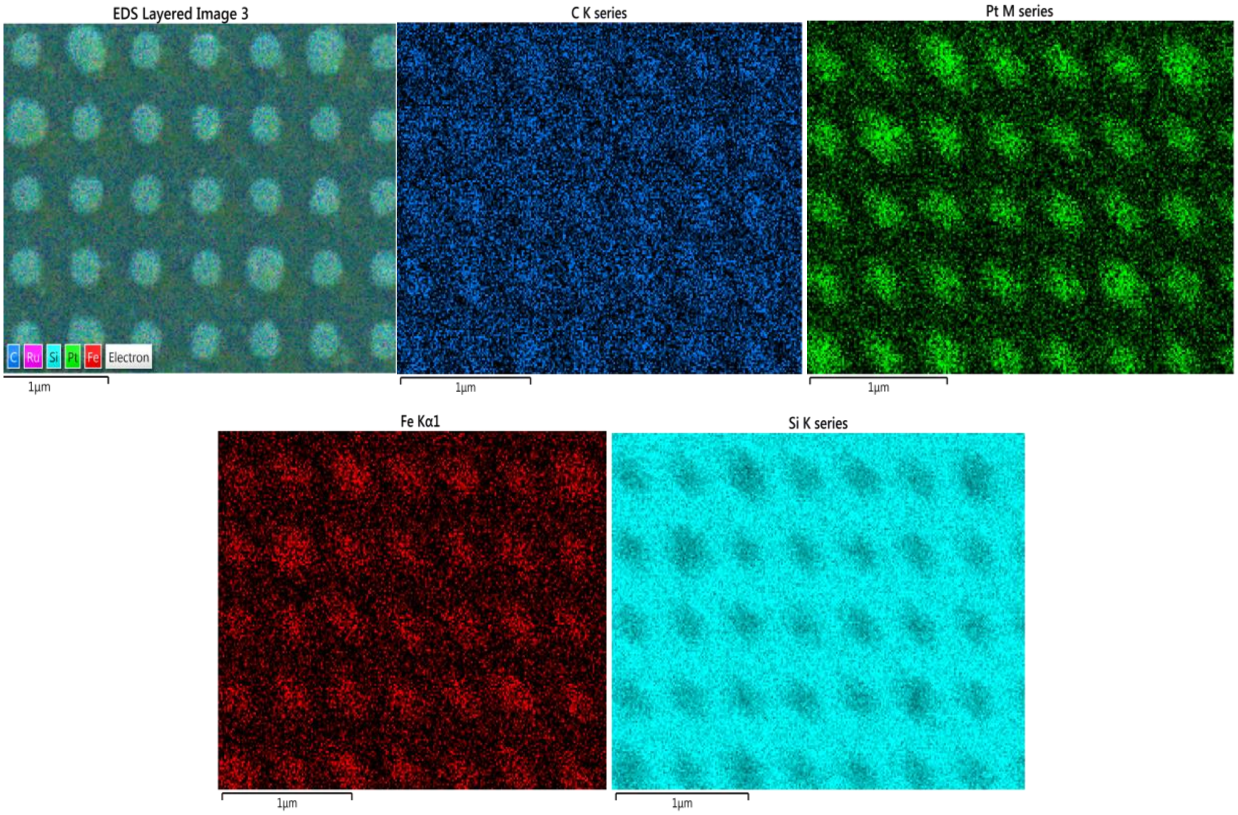

Figure 3. 41 Mapping of $Fe_{46}Pt_{54}$

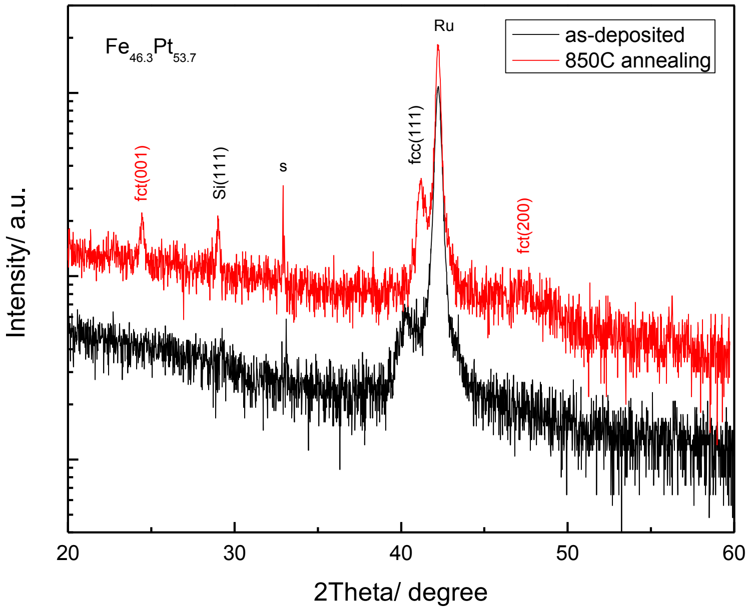

Figure 3. 42 XRD pattern for sample D1- $Fe_{46}Pt_{54}$ before and after 850°C annealing

XRD patterns for sample D2 are shown in **Fig 3.42**. For as-deposited $Fe_{46}Pt_{54}$, a fcc(111) peak is observed at 40.45°; after annealing at 850°C for 10min, the (111) peak becomes much more intense and shifts to larger angles; the coercivity became 4.7kOe in the parallel direction and 4.3kOe in the perpendicular direction (**Fig 3.43**), showing an essentially isotropic behavior.

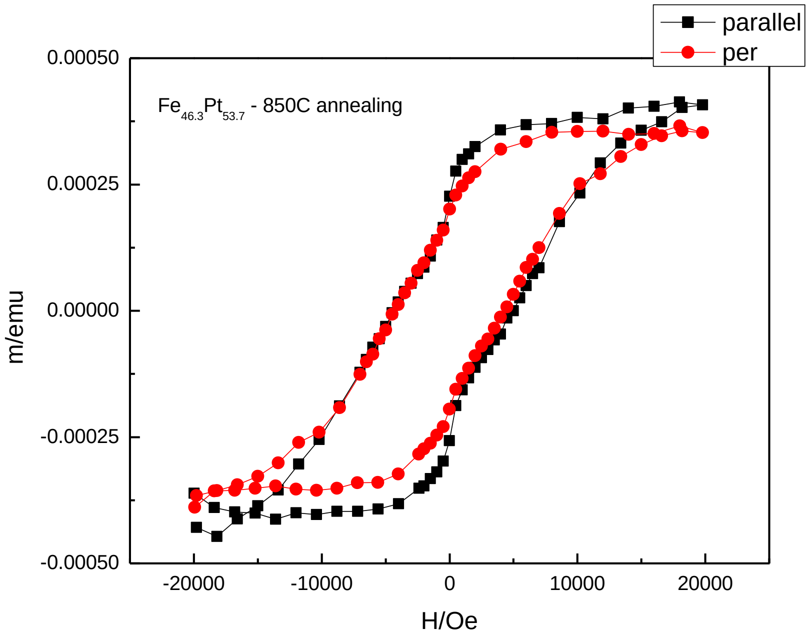

Figure 3. 43 Hysteresis loops for sample $Fe_{46}Pt_{54}$ before and after 850°C annealing

4. Synthesis and characterization of FeNiPt alloy for potential application in HAMR

4.1. Electrolyte selection for FeNiPt deposition

A series of solutions based on various ratios of $Fe_2(SO_4)_3$, Pt-p-salt and $NiSO_4$ were explored, with the total volume being kept in all cases at 100ml. At first, 25mM $Fe_2(SO_4)_3$, and 10mM Pt-p-salt were tried, while the concentration of $NiSO_4$ varied from 2mM, 5mM, 10mM, 15mM to 20mM aimed at depositing Ni-doped FePt thin films. A recipe showing all the constituents of the electrolyte is given in **Table 4.1**.

$NaNO_2$	0.1M
$(NH_4)_2SO_4$	0.1M
NH_2CH_2COOH, glycine	0.15M
$(NH_4)_2C_6H_6O_7$	0.15M
$Fe_2(SO_4)_3$	50mM
$Pt(NH_3)_2(NO_2)_2$	10mM
$NiSO_4$	2, 5, 10, 15, 20mM

pH: 8 (by KOH), T: 75^{o}C (water bath circulator, EX 7)

Table 4. 1 Make-up of the Fe-Ni-Pt electrolyte (Pt-p-salt: 10mM)

For each solution, we studied the alloy composition vs. potential behavior. Alloy composition is determined using energy dispersive spectroscopy (EDS) either attached to a JEOL JSM-6700F scanning electron microscopy (SEM), with an accelerating voltage of 20kV or a Quanta 650 SEM with an accelerating voltage of 5kV; the K or L lines were used to identify the elements Fe and Ni, and the M line was used for the element Pt. Results are shown below in **Figure 4.1**:

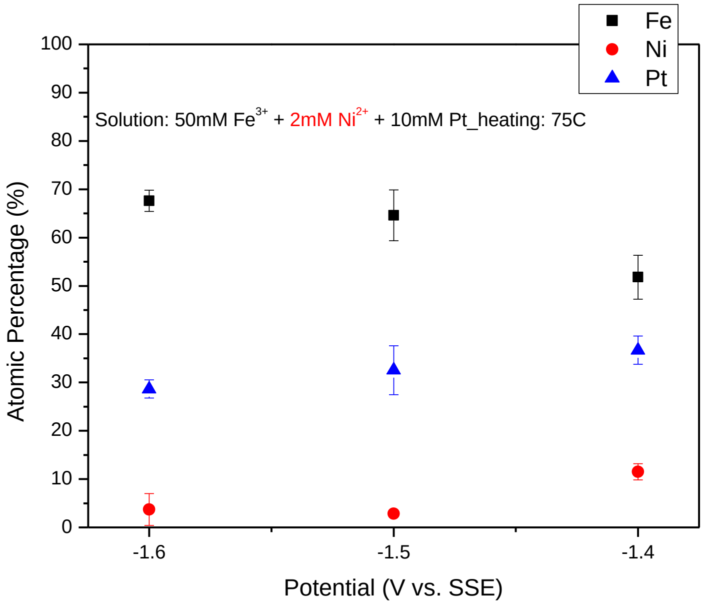

Fig 4. 1 Composition vs. potential for FeNiPt alloy thin films deposited from solutions with 2mM $NiSO_4$.

Our targeted composition of FeNiPt films is $Fe_{50-x}Ni_xPt_{50}$ $(0<x<30)$, but the films deposited from the solution with 2mM $NiSO_4$ concentration didn't reach a Pt content of 50at% even at the potential of -1.4V (vs. MSE). Though by adopting a more positive deposition potential, we can form FeNiPt thin films with 50 at% Pt, this would slow down deposition rate and make the deposition process much longer than expected. Therefore, we want to enhance the deposition process by increasing the concentration of metal sources in the plating bath. We first tried to change the concentration of $NiSO_4$ to 5mM, 10mM and 15mM, and found that results are quite similar to that obtained from the 2mM $NiSO_4$ solution (**Fig 4.2a**): we need therefore to extend the positive deposition potential limit from -1.4V to -1.25V (vs. MSE) and deposition time from several minutes to 2 hours to obtain a 10nm thickness FeNiPt film with a Pt content of around 50at%.

(a)

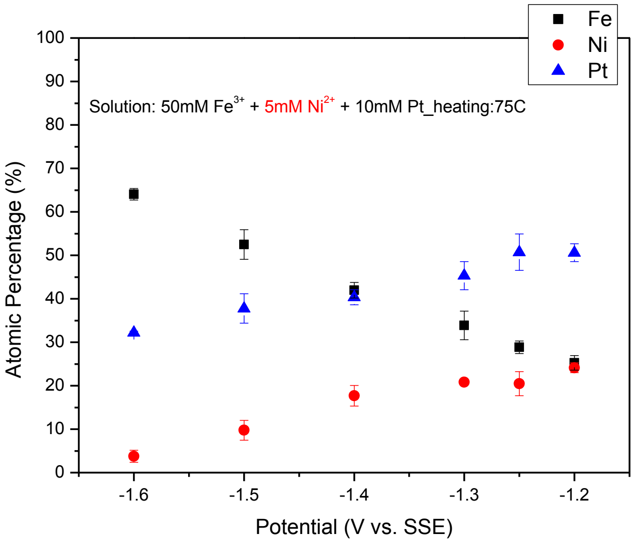
Fe
Ni
Pt
Solution: 50mM Fe^{3+} + 5mM Ni^{2+} + 10mM Pt_heating:75C
Atomic Percentage (%)
100
90
80
70
60
50
40
30
20
10
0
-1.6
-1.5
-1.4
-1.3
-1.2
Potential (V vs. SSE)

(b)

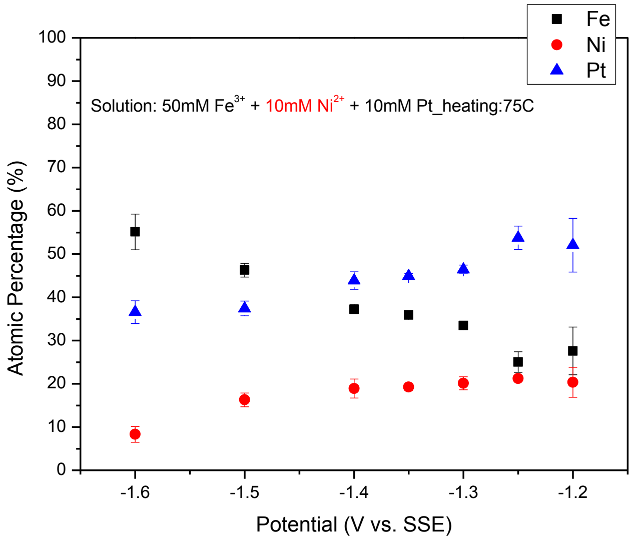
Fe
Ni
Pt
Solution: 50mM Fe^{3+} + 10mM Ni^{2+} + 10mM Pt_heating:75C
Atomic Percentage (%)
100
90
80
70
60
50
40
30
20
10
0
-1.6
-1.5
-1.4
-1.3
-1.2
Potential (V vs. SSE)

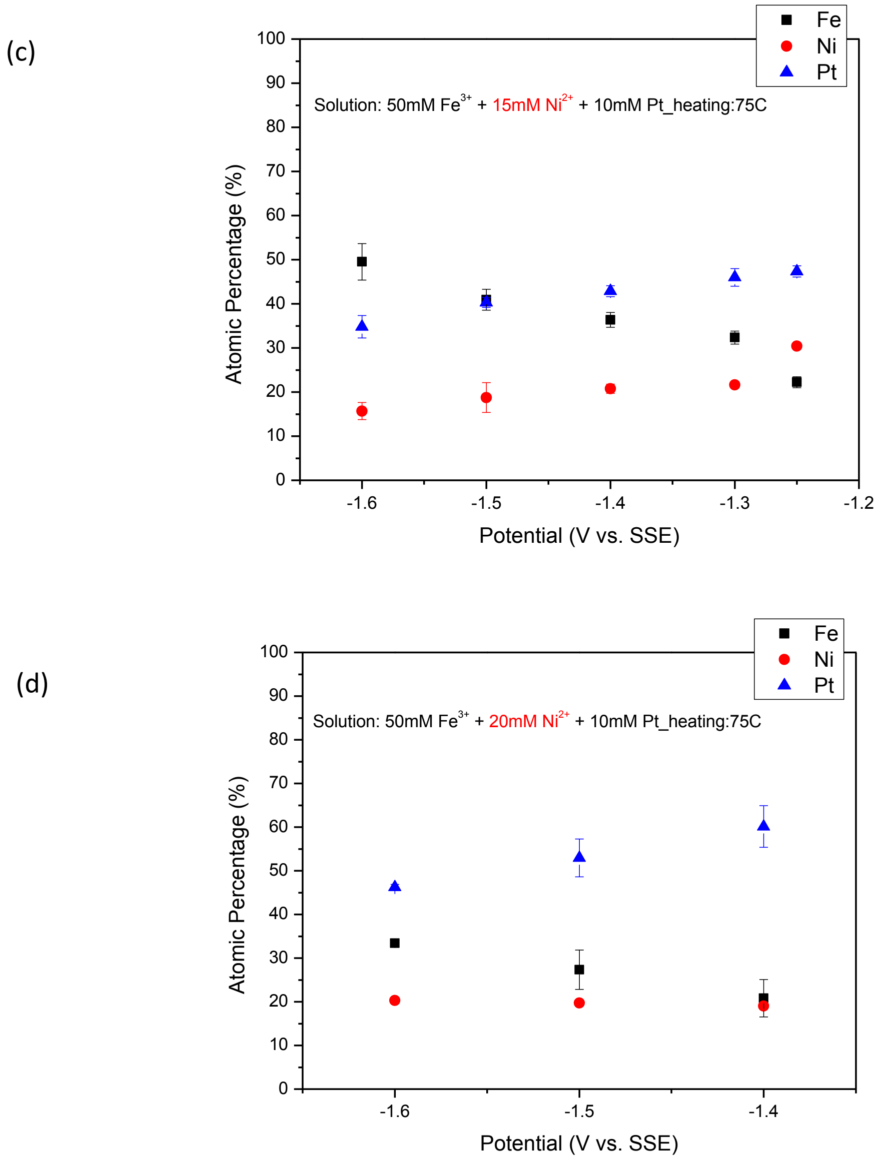

Fig 4. 2 Composition vs. potential for FeNiPt alloy thin films deposited from solutions with various $NiSO_4$ concentrations, as shown in each figure.

However, when we further increase the $NiSO_4$ concentration to 20mM, a film composition with a 50% Pt content can be easily tailored within the potential range of -1.5V ~ -1.6V (**Fig 4.2d**), and a deposition rate is significantly increased; for example, a growth time of 10 min at potential of -1.5V (vs. MSE) gives a film thickness of around 100nm. From all the films that have been grown, we selected and compared the deposition conditions of those satisfying a composition of $Fe_{50-x}Ni_xPt_{50}$ (0<x<30), given in **Table 4.2**. We also calculate the deposition rate (nm/h) from the average thicknesses calculated for samples 2, 4, 5 and 6; the relationship between this rate and the concentration of $NiSO_4$ in the electrolyte can be seen in **Fig 4.3**.

Sample	Solution	Potential (V vs. MSE)	Deposition time	Composition	Thickness
1	5mM Ni	-1.2V	2h	$Fe_{25}Ni_{24}Pt_{51}$	~10nm
2	5mM Ni	-1.25V	2h	$Fe_{29}Ni_{21}Pt_{51}$	~10nm
3	10mM Ni	-1.2V	2.25h	$Fe_{28}Ni_{20}Pt_{52}$	~10nm
4	10mM Ni	-1.25V	2h	$Fe_{25}Ni_{21}Pt_{54}$	~10nm
5	15mM Ni	-1.25V	2h	$Fe_{22}Ni_{30}Pt_{48}$	~10nm
6	20mM Ni	-1.5V	10min	$Fe_{27}Ni_{20}Pt_{53}$	100nm

Table 4. 2 Deposition conditions for films with a composition of $Fe_{50-x}Ni_xPt_{50}$ (0<x<30)

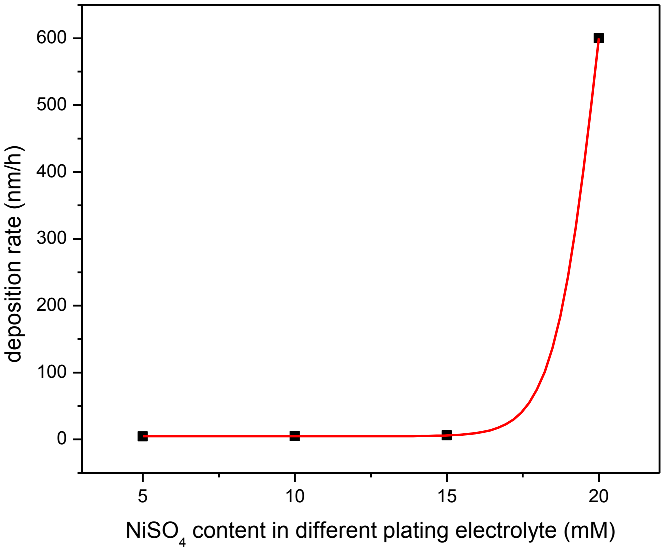

Fig 4. 3 Growth rate of $Fe_{25}Ni_{25}Pt_{50}$ thin film on the Ni^{2+} concentration in electrolytes

Besides, we also found that by increasing Ni^{2+} concentration in the electrolyte from 2mM to 20mM, the fraction of (Ni+Pt) with respect to Fe in the as-deposited FeNiPt thin films increased (**Fig 4.4**), which means that by adding more Ni^{2+} source in the electrolyte, we should expect a lower Fe content in the deposited films given the same deposition conditions. This behavior is expected for mutual alloys of Fe group metals.

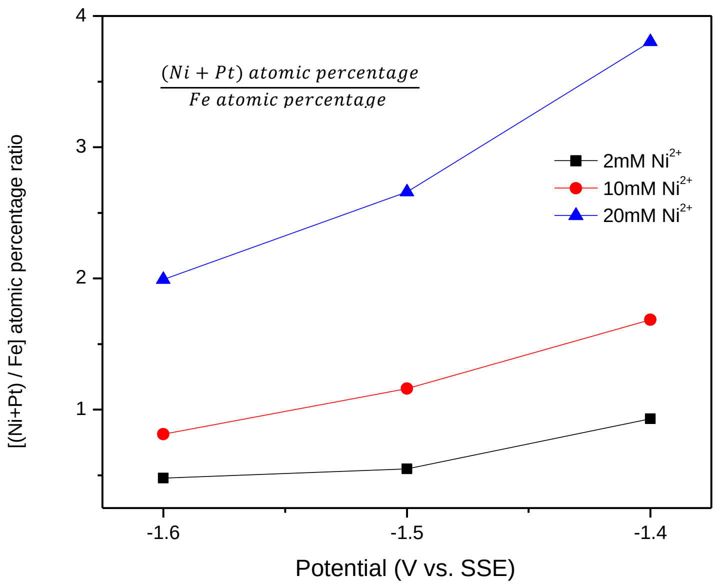

Fig 4. 4 Dependence of (Ni + Pt)/Fe ratio in deposited films on the Ni^{2+} concentration and applied potentials in electrolytes

By comparing the Fe/Ni ratio in the electrolyte and that in the deposited alloys (**Fig 4.5**), we found following:

- When the applied potential is fixed, the higher the Fe/Ni ratio in the electrolyte, the large the value of Fe/Ni in the deposited films;
- For the solution containing the largest amount of $NiSO_4$ (20mM), Fe/Ni increases very slowly with the increase of a negative potential, while for solutions containing

the least amount of $NiSO_4$ (5mM), Fe/Ni increases very fast with the potential being more negative. Combined with consistent trends observed in solutions with 10mM and 15mM $NiSO_4$, we therefore concludes that the Fe/Ni ratio becomes less sensitive to the applied potential when the Ni^{2+} becomes more concentrated in the plating electrolyte.

- The content of Fe in the alloy increased and Ni decreased with the potential going more negative. When deposited at the potential of -1.6 (V vs. MSE) from solutions with 5mM and 10mM $NiSO_4$, the percentage of Fe content in the films is much higher than their relative concentration in the electrolyte, suggesting the occurrence of the phenomenon of anomalous codeposition[118], where the preferential deposition of the thermodynamically less noble metal - Fe.

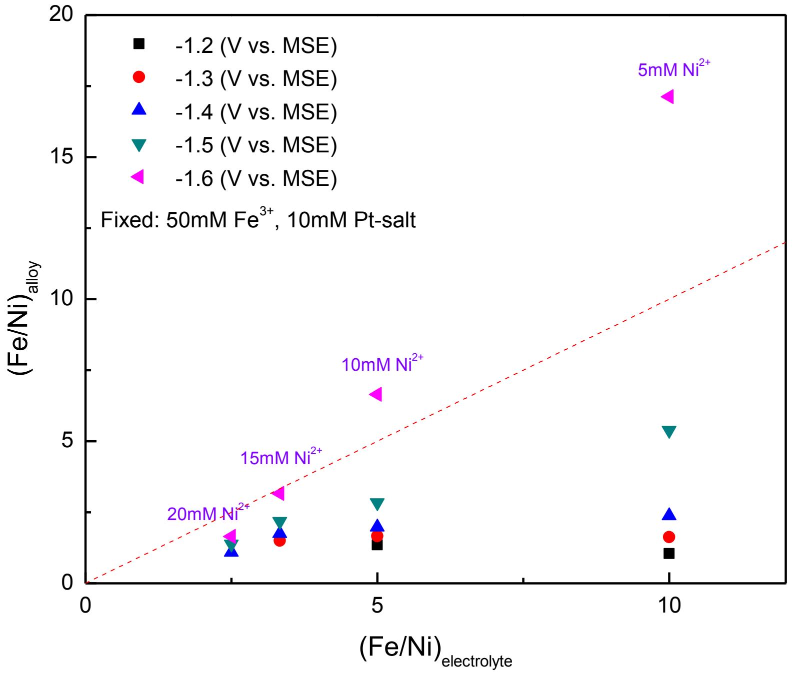

Fig 4. 5 Comparison of the (Fe/Ni) in electrolyte and that in the as-deposited films

As a summary, for each electrolyte with different $NiSO_4$ concentration (2mM, 5mM, 10mM, 15mM or 20mM), all the as-deposited films are homogenous and exhibit a shining surface in light gray to dark gray color with the deposition potential going more negative; the Fe content in the as-deposited alloy thin films decreases with the potential going more positive, while the Pt content keeps increasing. For solutions with 5mM, 10mM or 15mM $NiSO_4$, we obtained $Fe_{50-x}Ni_xPt_{50}$ ($20<x<30$) thin films around 10nm at the deposition potential within -1.2V to -1.25V (vs. MSE) for a relatively long deposition time (2-2.5h). By increasing the $NiSO_4$ concentration in the plating electrolyte to 20mM, we obtained a 100nm $Fe_{27}Ni_{20}Pt_{53}$ at a potential negatively shifted to -1.5V, which greatly enhanced the deposition rate and shortened the growth time to reach a suitable film thickness.

Till now, we successfully developed a solution that can be used to rapidly produce $Fe_{50-x}Ni_xPt_{50}$ films with $x \sim 20$ at a potential between -1.5V and -1.6V (**Fig 4.2d**). To generate a wider range of Ni content in the deposited films (namely, $0<x<30$), we changed the concentration of Pt-p-salt from 10mM to 15mM and explored the relationship between the composition of as-deposited thin films with the applied potentials for a series of solutions with Ni^{2+} concentration ranging from 5mM, 10M, 15mM to 25mM. The plating bath recipe and results are shown in **Table 4.3** and **Fig 4.6**, respectively.

$NaNO_2$	0.1M
$(NH_4)_2SO_4$	0.1M
NH_2CH_2COOH, glycine	0.15M
$(NH_4)_2C_6H_6O_7$	0.15M
$Fe_2(SO_4)_3$	50mM
$Pt(NH_3)_2(NO_2)_2$	15mM
$NiSO_4$	5, 10, 15, 25mM
pH: 8 (by KOH), T: 75^{o}C (water bath circulator, EX 7)	

Table 4. 3 Make-up of the Fe-Ni-Pt electrolyte (Pt-p-salt: 15mM)

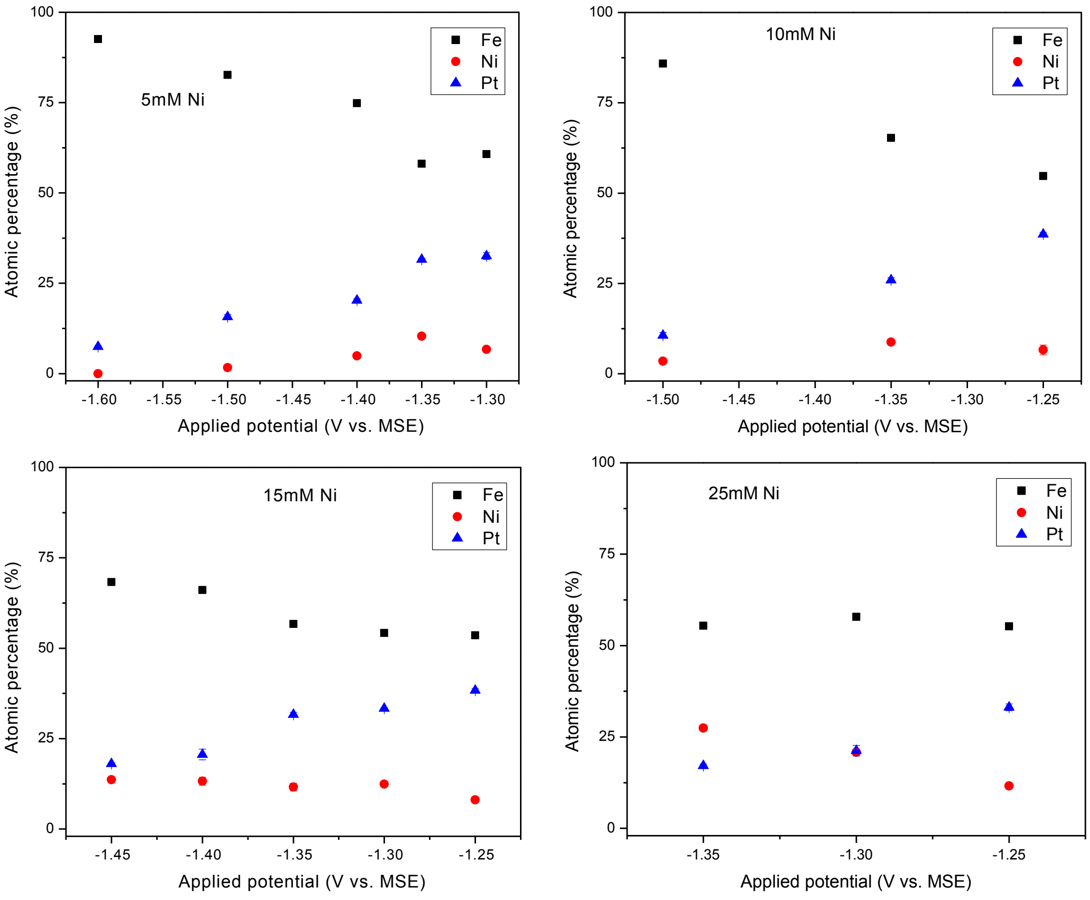

Fig 4. 6 Composition vs. potential for FeNiPt alloy thin films (Pt-p-salt: 15mM, $NiSO_4$: 5, 10, 15, 25mM)

We clearly see that all films generated here have a Fe content larger than 50%, which is beyond our expectation. However, one good thing here is that we begin to see relatively small amount of Ni content (<12%) in the as-deposited FeNiPt thin films in all these four solutions at potential of -1.25V, which is close to the region where we should expect a film with 50% Pt. As a result, we decided to modify the concentration of ferric sulfate in the deposition bath with the Pt-p-salt fixed at 15mM (**Table 4.4**), the results for deposition are shown in **Fig 4.7**.

$NaNO_2$	0.1M
$(NH_4)_2SO_4$	0.1M
NH_2CH_2COOH, glycine	0.15M
$(NH_4)_2C_6H_6O_7$	0.15M
$Fe_2(SO_4)_3$	5, 10, 15, 20mM
$Pt(NH_3)_2(NO_2)_2$	15mM
$NiSO_4$	15mM
pH: 8 (by KOH),	T: 75°C (water bath circulator, EX 7)

Table 4. 4 Make-up of the Fe-Ni-Pt electrolyte (Pt-p-salt: 15mM, $NiSO_4$: 15mM, ferric sulfate: 5, 10, 15, 20mM)

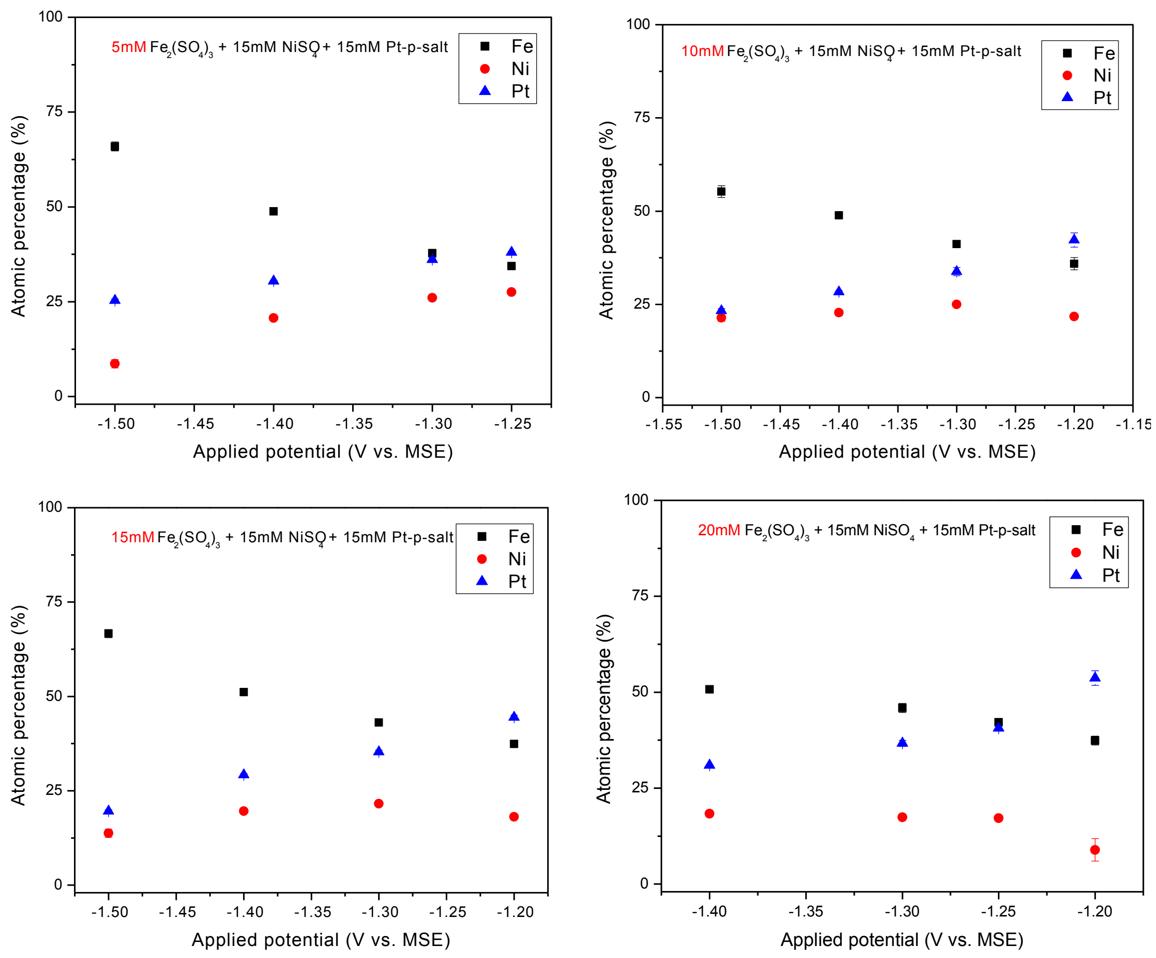

Fig 4. 7 Composition vs. potential for FeNiPt alloy (Pt-p-salt: 15mM; $NiSO_4$: 15mM, ferric sulfate: 5, 10, 15, 20mM)

Potential	5mM $Fe_2(SO_4)_3$	10mM $Fe_2(SO_4)_3$	15mM $Fe_2(SO_4)_3$	20mM $Fe_2(SO_4)_3$
-1.2V		$Fe_{36}Ni_{22}Pt_{42}$	$Fe_{37}Ni_{18}Pt_{45}$	$Fe_{37}Ni_9Pt_{54}$
-1.25V	$Fe_{34}Ni_{28}Pt_{38}$			$Fe_{42}Ni_{17}Pt_{41}$
-1.3V	$Fe_{38}Ni_{26}Pt_{36}$	$Fe_{41}Ni_{25}Pt_{34}$	$Fe_{43}Ni_{22}Pt_{35}$	$Fe_{46}Ni_{17}Pt_{37}$
-1.4V	$Fe_{49}Ni_{21}Pt_{30}$	$Fe_{49}Ni_{22}Pt_{28}$	$Fe_{51}Ni_{20}Pt_{29}$	$Fe_{51}Ni_{18}Pt_{31}$
-1.5V	$Fe_{66}Ni_9Pt_{25}$	$Fe_{55}Ni_{21}Pt_{24}$	$Fe_{67}Ni_{13}Pt_{20}$	

Table 4. 5 Composition of FeNiPt films deposited at various potentials from different solutions

From this set of data, we obtained a film with the composition of $Fe_{37}Ni_9Pt_{54}$, the first time that we generated FeNiPt thin films with a Ni content less than 10%. From **Table**

4.5, we see that increasing the $Fe_2(SO_4)_3$ concentration in the plating bath helps produce desired films at relatively positive potentials, therefore, we decided to further increase the concentration of ferric sulfate in the plating bath, the make-up recipe is shown in **Table 4.6**.

$NaNO_2$	0.1M
$(NH_4)_2SO_4$	0.1M
NH_2CH_2COOH, glycine	0.15M
$(NH_4)_2C_6H_6O_7$	0.15M
$Fe_2(SO_4)_3$	25, 30mM
$Pt(NH_3)_2(NO_2)_2$	15mM
$NiSO_4$	15mM
pH: 8 (by KOH), T: 75°C (water bath circulator, EX 7)	

Table 4. 6 Make-up of the Fe-Ni-Pt electrolyte (Pt-p-salt: 15mM, $NiSO_4$: 15mM, ferric sulfate: 5, 10, 15, 20mM)

The corresponding composition dependence on applied potentials is now shown below (**Fig 4.8**), it is clear that content of Fe in the alloy increased slowly with the potential going more negative. Specifically, from the solution containing 30mM ferric sulfate, we obtain a series of films with a Pt content near 50 at% (**Table 4.7**). Those films are selected and annealed at a temperature of 650°C for 1h under the flowing forming gas.

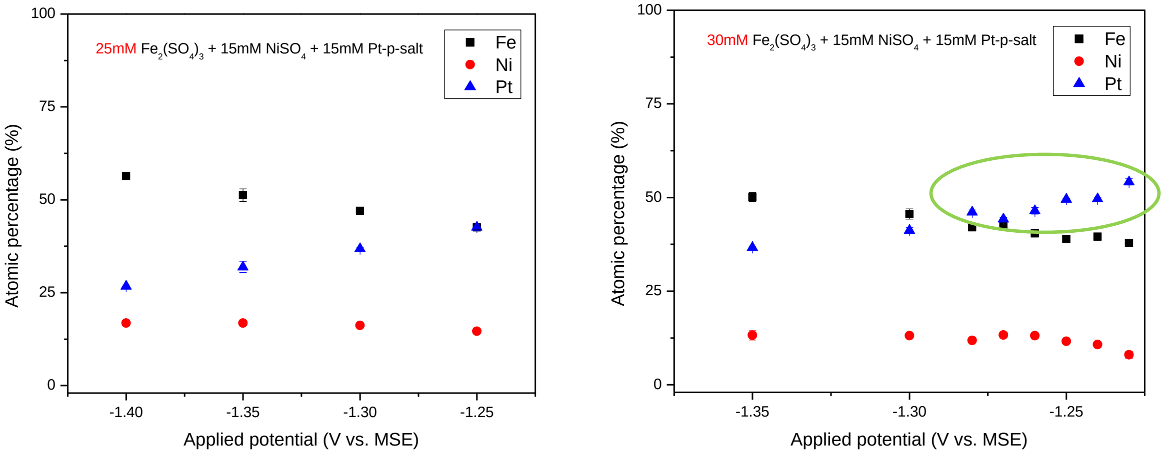

Fig 4. 8 Composition of films deposited at various potentials from solutions with 25mM and 30mM Ferric sulfate

Potential	Time	Composition	Fe/Pt	Thickness/nm
-1.22V	1.5h	$Fe_{38}Ni_{7}Pt_{55}$	0.678	~20
-1.23V	1.5h	$Fe_{38}Ni_{8}Pt_{54}$	0.697	~20
-1.24V	1h	$Fe_{39}Ni_{11}Pt_{50}$	0.797	~20
-1.25V	1h	$Fe_{39}Ni_{12}Pt_{49}$	0.786	~20
-1.26V	0.75h	$Fe_{40}Ni_{13}Pt_{47}$	0.869	~20
-1.27V	0.75h	$Fe_{43}Ni_{13}Pt_{44}$	0.962	~20
-1.28V	0.75h	$Fe_{42}Ni_{12}Pt_{46}$	0.913	~30

Table 4. 7 Composition of films deposited at various potentials from solution with 30mM ferric sulfate

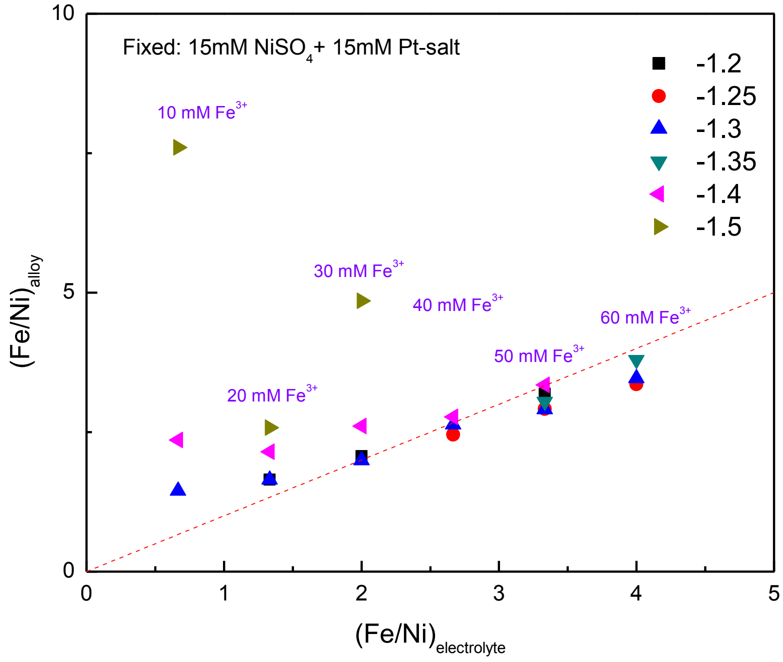

Fig 4. 9 Comparison of the (Fe/Ni) in electrolyte and that in the as-deposited films

Comparing the Fe/Ni ratio in the electrolyte and that in the deposited alloys (**Fig 4.9**), a similar phenomenon is observed as in **Fig 4.5**: when deposited at relatively negative potentials (-1.4 ~ -1.6V vs. MSE) from solutions with ferric concentration less than 30mM, the Fe percentage in the films is much higher than their relative concentration in the electrolyte, indicating the phenomenon of anomalous codeposition[119]. For solutions with higher ferric concentration (40, 50 and 60mM), Fe/Ni ratios in the as-deposited films become insensitive to the applied potentials and gets closer to the Fe/Ni ratios in the electrolyte.

4.2. Structure and magnetic properties of $Fe_{50-x}Ni_xPt_{50}$ thin films

Previously, we have electrodeposited a set of FeNiPt thin films from solutions containing the same background chemicals but slightly varied metallic concentration (**Table 4.2**) and another set from a single solution with 30mM ferric sulfate (**Table 4.7**). All films are annealed at 450°C, 550°C and 650°C for 1h subsequently. With the processing path the same, we compare the structure and magnetic properties of these films.

The thermodynamic disordering temperature of $L1_0$ FePt phase is 1300°C[120]. FePt films fabricated by sputtering or other deposition methods have a disordered FCC phase structure, high temperature heat treatment above 500°C is therefore normally needed to transform the FCC phase to an ordered FCT phase[121]. Here we studied the ordering temperature in Ni-doped FePt thin films produced by electrodeposition, together with the corresponding magnetic properties. All films were rapidly heated to a high temperature (450-700°C) in 3-5min, in the expectation to result in a fine microstructure.

i) Films with relatively large x (18<x<31, shown in **Table 4.2**).

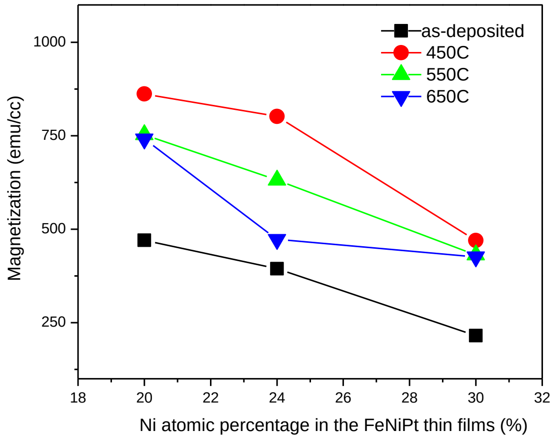

Fig 4. 10 Magnetization decreases with the increase of Ni content in 10nm FeNiPt films

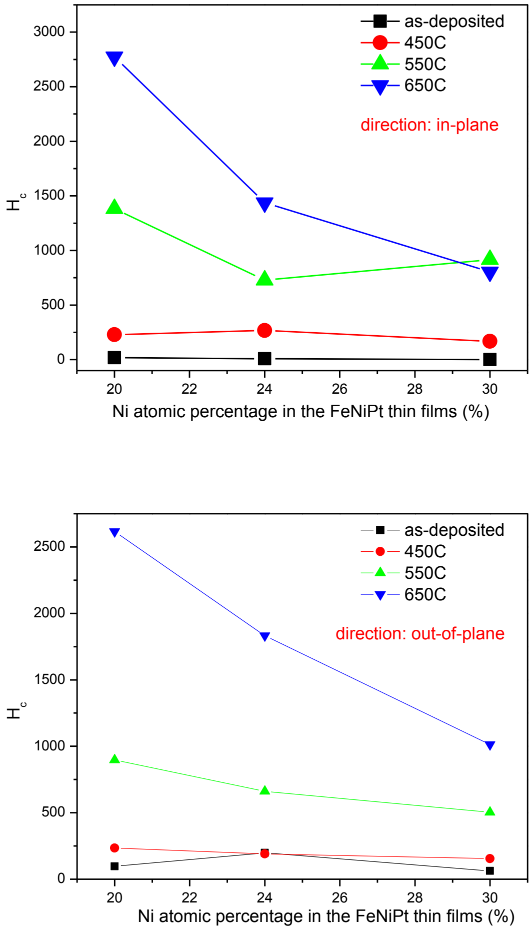

Fig 4. 11 Coercivity dependence on the Ni content in 10nm FeNiPt films

In this series of $Fe_{50-x}Ni_xPt_{50}$ (18<x<31) thin films with the same thickness of 10nm, coercivity grows and magnetization decreases with the increase of annealing temperature (**Fig 4.10** and **Fig 4.11**). Both in the as-deposited and annealed films, magnetization and coercivity decrease with the increase of Ni content.

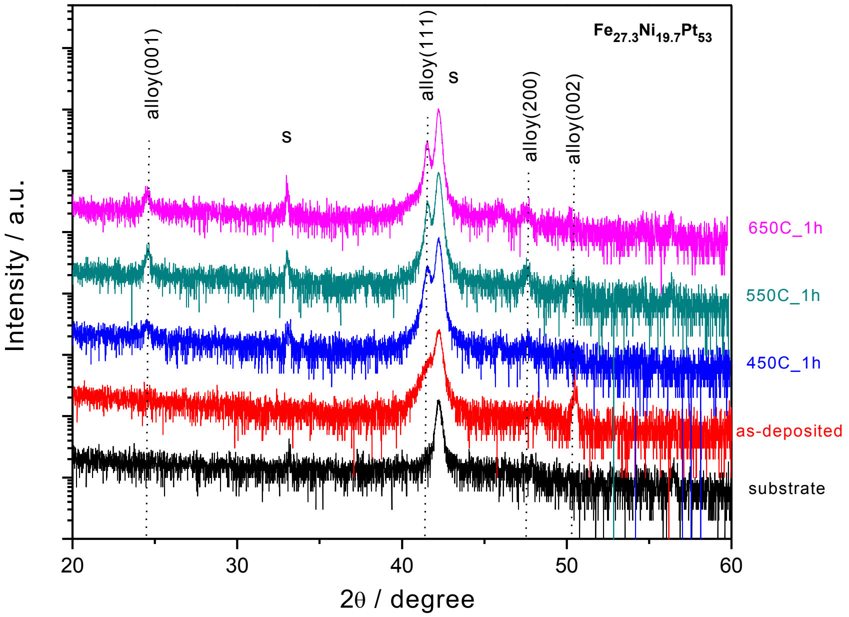

Fig 4. 12 XRD pattern of 100nm $Fe_{27}Ni_{20}Pt_{53}$ before and after annealing

The XRD patterns of as-deposited and annealed $Fe_{27}Ni_{20}Pt_{53}$ are shown in **Fig 4.12**, while the in-plane hysteresis loops of these films are shown in **Fig 4.13**. Lattice constants extracted from XRD data are listed in **Table 4.8**. It can be seen that the coercivity and squareness ratio (remanent to saturated magnetization: M_r/M_s) of the film increase with annealing temperature up to 550°C, and remain nearly the same after 650°C annealing.

T/°C	(001)		(111)		(200)		(002)	
	2θ/°	c/Å	2θ/°	a'/Å	2θ/°	a/Å	2θ/°	c/Å
450°C	24.493	3.631	41.582	3.759				
550°C	24.574	3.620	41.519	3.764	47.535	3.823	50.297	3.625
650°C	24.532	3.626	41.549	3.762	47.517	3.824	50.184	3.633

Table 4. 8 lattice parameters calculated from XRD (for $L1_0$ FePt: a = 3.853Å, c = 3.713Å)

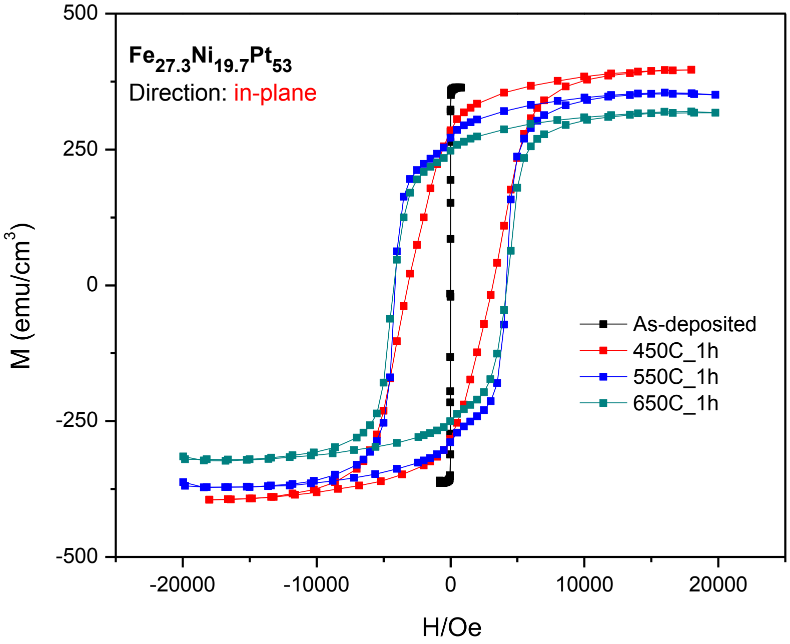

Fig 4. 13 Hysteresis loops of 100nm $Fe_{27}Ni_{20}Pt_{53}$ in in-plane direction before and after annealing

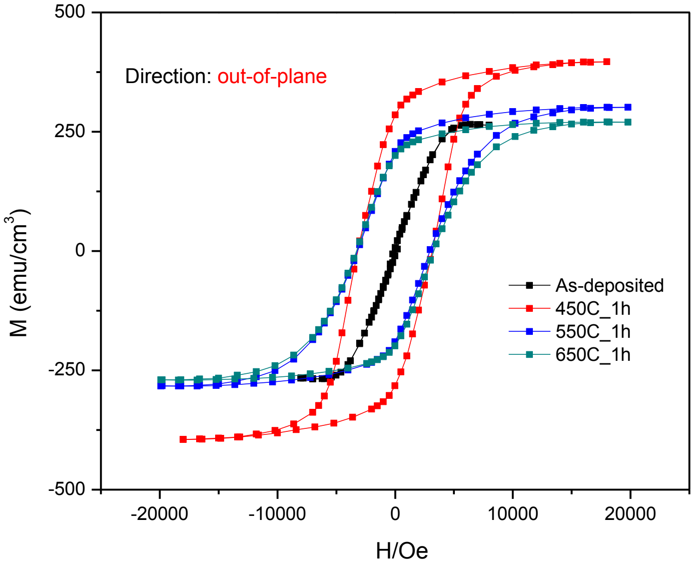

Fig 4. 14 Hysteresis loops of 100nm $Fe_{27}Ni_{20}Pt_{53}$ in out-of-plane direction before and after annealing

Fig 4.14 shows the corresponding hysteresis loops in the perpendicular direction; it can be concluded that the easy magnetization axis is mainly in the film plane, and magnetic hardening can be attributed to the formation of the high anisotropy $L1_0$ FePt phase[125]. This is indeed observed after annealing at 450°C for 1h, corresponding to the appearance of (001) and (200) peaks. After 550°C and 650°C annealing for 1h, the coercivity continues to increase, and the sample finally reached a coercivity of 4.2kOe in the in-plane direction and 3.3kOe in the out-of-plane direction.

ii) For $Fe_{50-x}Ni_xPt_{50}$ films with a relatively small x (7<x<13), thicknesses are examined under SEM, showing similar values around 20nm (**Fig 4.15**).

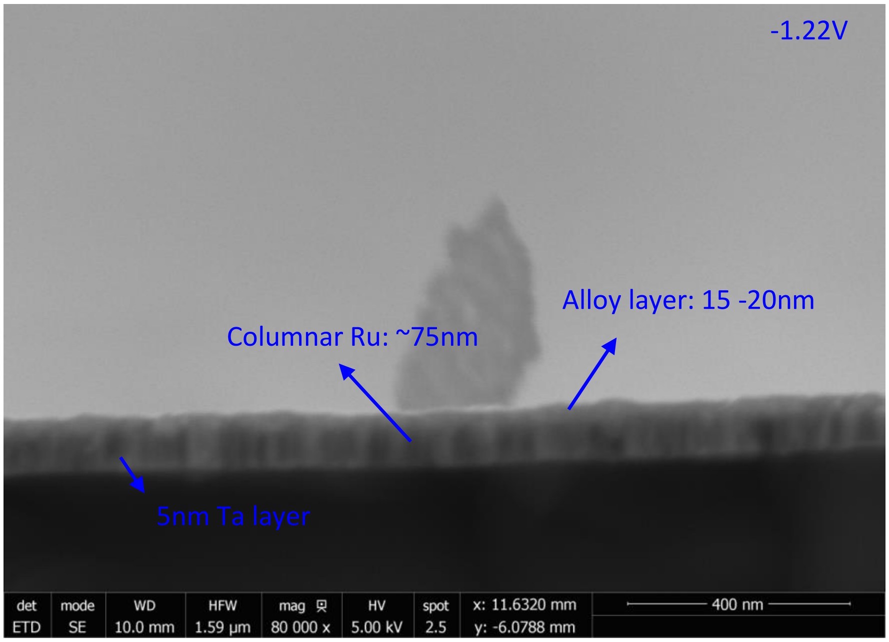

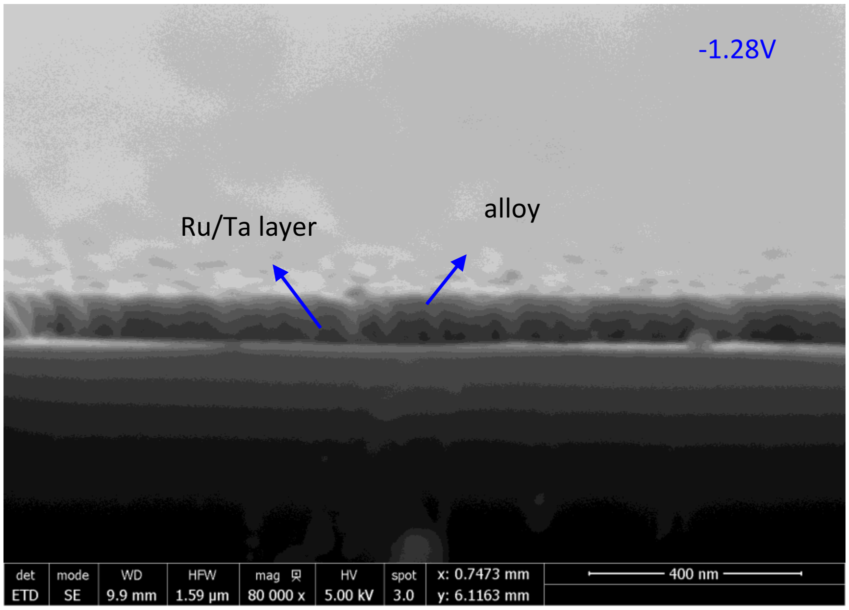

Fig 4. 15 Selected SEM cross-section images showing the thickness of FeNiPt films

1). Film $Fe_{38}Ni_7Pt_{55}$:

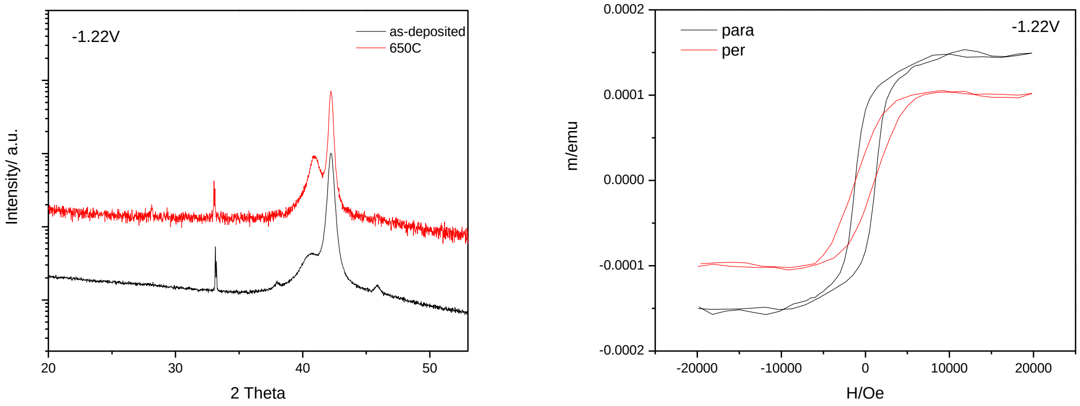

Fig 4. 16 left: XRD (before/after 650^{o}C, 1h); right: Hysteresis loops for film $Fe_{38}Ni_7Pt_{55}$ after 650^{o}C annealing

After 650ºC annealing for 1h, the fcc(111) peak shifts from 40.804º to 40.964º with its intensity being much stronger, the lattice parameter of annealed films is calculated to be 3.8137 Å, indicating a decrease of Pt content, probably due to interdiffusion into Ru (**Fig 4.16**, left). No evidence of ordering is observed and the annealed film shows a single fcc(111) texture, however, coercivity grows to around 1.2kOe in both the in-plane and out-of-plane directions after annealing (**Fig 4.16**, right).

2). Film Fe$_{38}$ Ni$_8$Pt$_{54}$:

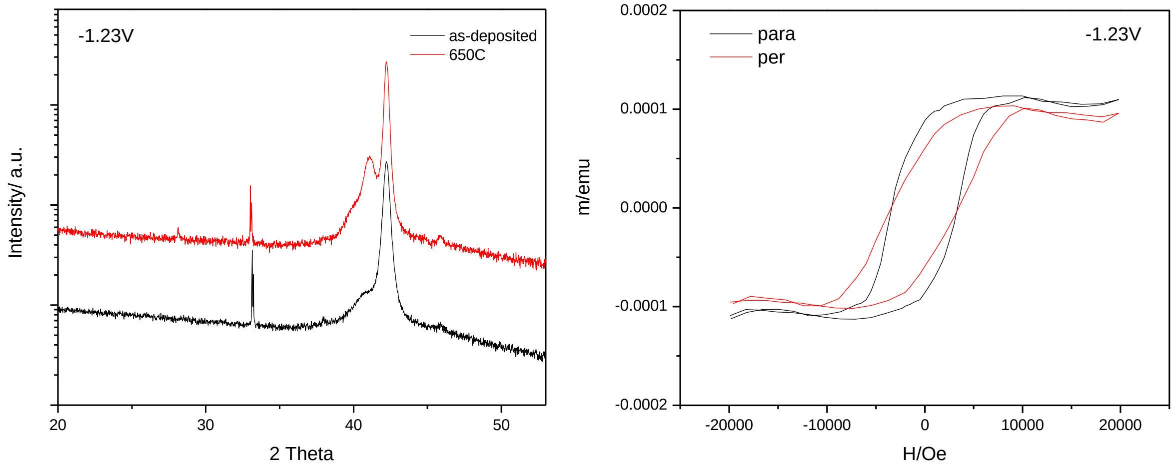

Fig 4. 17 Left: XRD (before/after 650^{o}C, 1h); right: Hysteresis loops for film Fe$_{38}$ Ni$_8$Pt$_{54}$ after 650^{o}C annealing

From the fcc(111) peak, lattice parameter of annealed films is calculated to be 3.7993 Å (**Fig 4.17**, left), and coercivity grows to around 3.4kOe both in the in-plane and out-of-plane directions (**Fig 4.17**, right).

3). Film Fe$_{39}$Ni$_{11}$Pt$_{50}$:

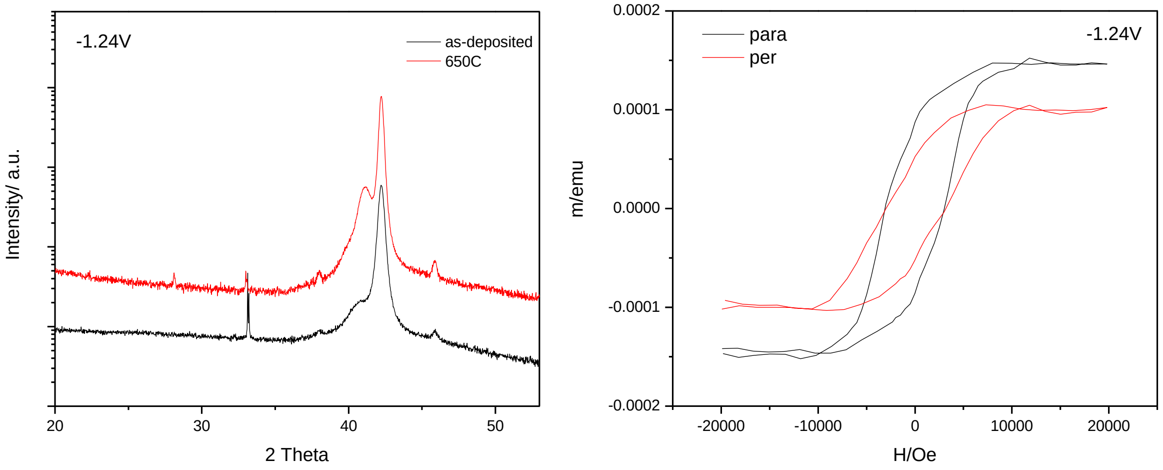

Fig 4. 18 left: XRD (before/after 650^{o}C, 1h); right: Hysteresis loops for film Fe$_{39}$Ni$_{11}$Pt$_{50}$ after 650^{o}C annealing

From the fcc(111) peak, lattice parameter of annealed films is calculated to be 3.7943 Å (**Fig 4.18**, left), and coercivity grows to around 3.0kOe both in the in-plane and out-of-plane directions (**Fig 4.18**, right).

4). Film $Fe_{39}Ni_{12}Pt_{49}$:

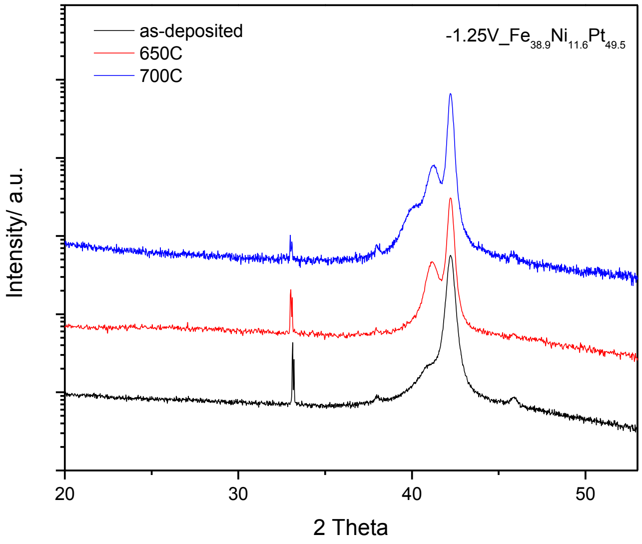

Fig 4. 19 XRD for film $Fe_{39}Ni_{12}Pt_{49}$ before/after 650°C, 1h

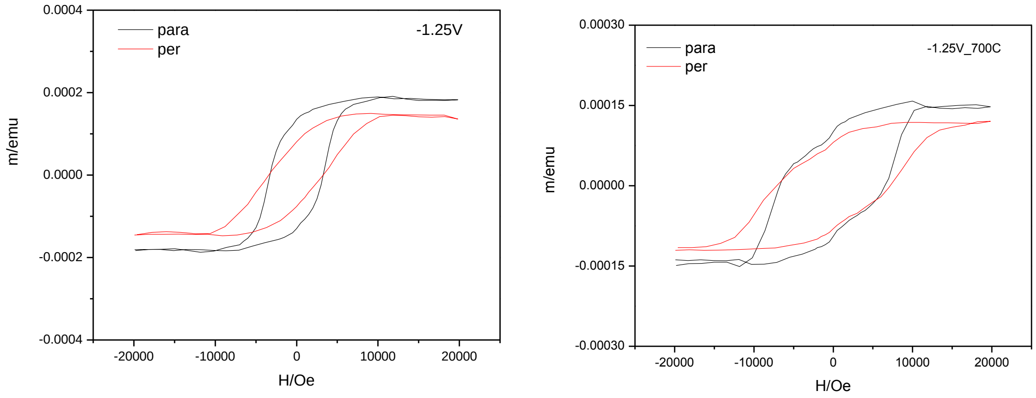

Fig 4. 20 Hysteresis loops of film $Fe_{39}Ni_{12}Pt_{49}$ measured after 650°C annealing (left) and 700°C annealing (right)

From the fcc(111) peak, the lattice parameter of 650°C annealed films is calculated to be 3.7906 Å (**Fig 4.19**). Coercivity grows to be around 3.3kOe both in the in-plane and out-of-plane directions after heat treatment at 650°C for 1h; and further increased to 6.6kOe in the in-plane direction and 7.2kOe in the perpendicular direction, respectively, after 700°C annealing for 1h (**Fig 4.20**). While magnetization curves in both directions are smooth after 650°C annealing, the hysteresis loop after 700°C shows a more apparent kink at low magnetic field in the out-of-plane direction than that in the in-plane direction. The kink comes from magnetically soft phases mixed in the hard phase[122]; these are probably due to nucleation of magnetization reversal under opposite field started at the soft phase[123]. The occurrence of the soft phase is confirmed in the XRD that shows a shoulder peak near fcc(111), and its amount is estimated by the decrease of magnetization at the kink[122], which is around 24%. One future experiment will seek to further annealing the sample and verify whether the kink disappears and the coercivity grows.

5). Film $Fe_{40}Ni_{13}Pt_{47}$:

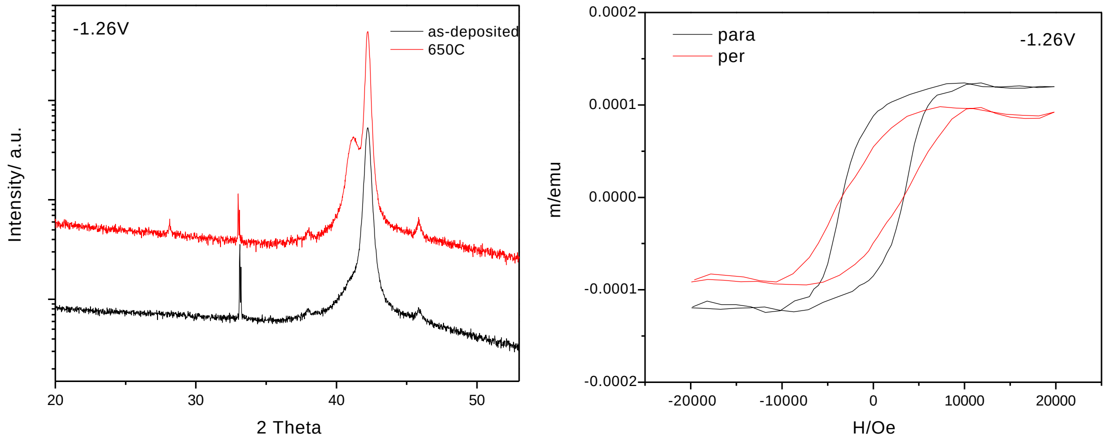

Fig 4. 21 Left: XRD (before/after 650°C, 1h); right: Hysteresis loops for film $Fe_{40}Ni_{13}Pt_{47}$ after 650°C annealing

From the fcc(111) peak, the lattice parameter of annealed films is calculated to be 3.7866 Å (**Fig 4.21**, left), and coercivity grows to around 3.4kOe both in the in-plane and out-of-plane directions (**Fig 4.21**, right).

6). Film $Fe_{43}Ni_{13}Pt_{44}$:

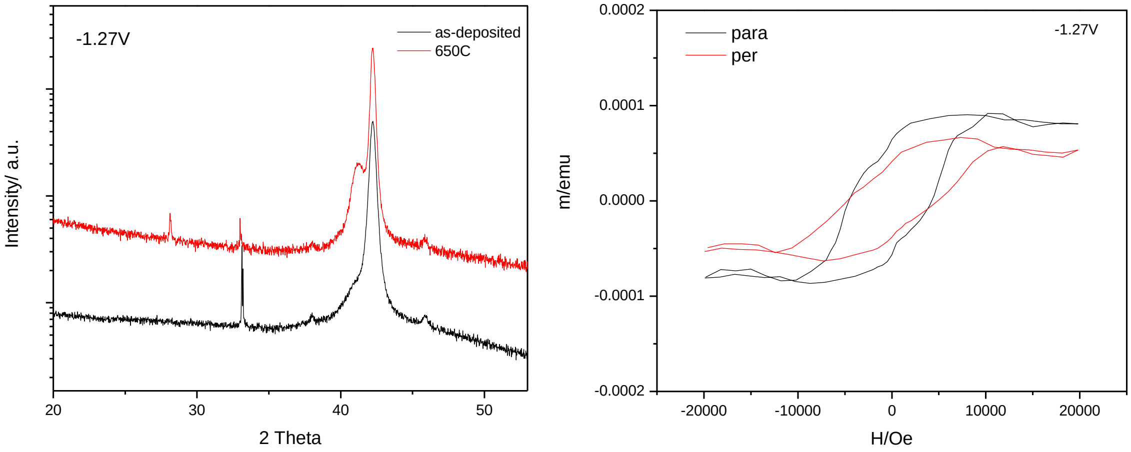

Fig 4. 22 left: XRD (before/after 650°C, 1h); right: Hysteresis loops for film $Fe_{43}Ni_{13}Pt_{44}$ after 650°C annealing

From the fcc(111) peak, lattice parameter of annealed films is calculated to be 3.7856 Å (**Fig 4.22**, left), and coercivity grows to around 4.8kOe both in the in-plane and out-of-plane directions (**Fig 4.22**, right).

7). Film $Fe_{42}Ni_{12}Pt_{46}$:

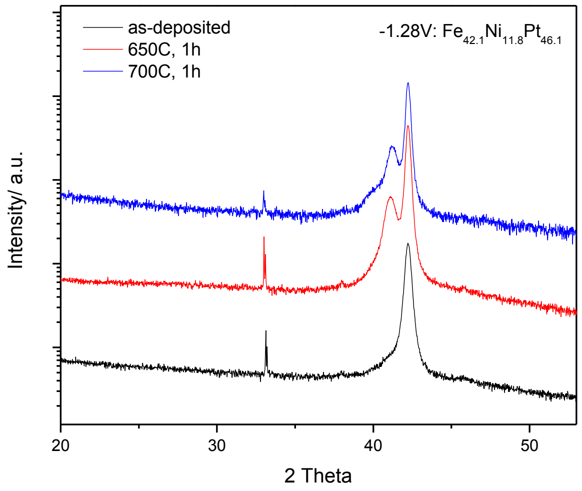

Fig 4. 23 XRD for film $Fe_{42}Ni_{12}Pt_{46}$ before and after 650°C annealing

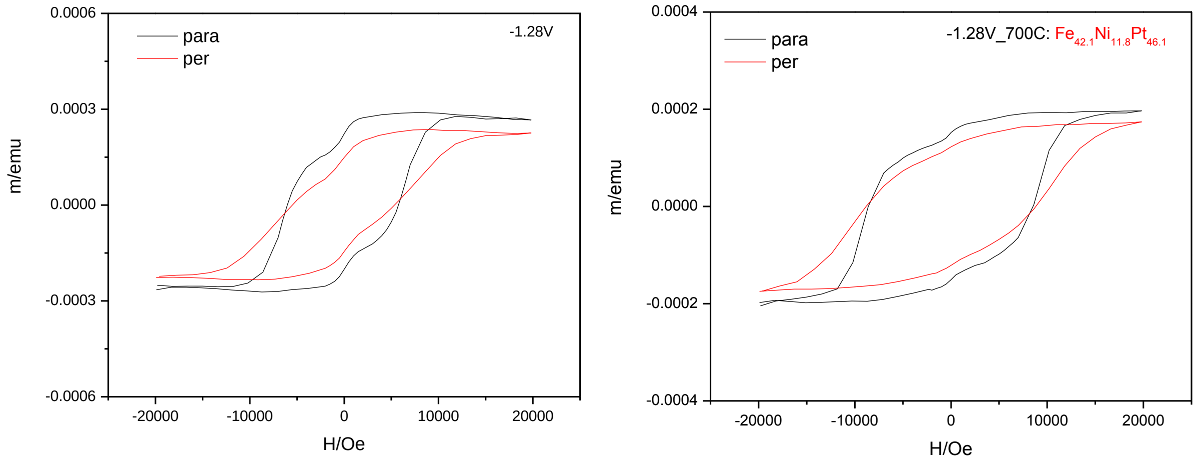

Fig 4. 24 Hysteresis loops for film $Fe_{42}Ni_{12}Pt_{46}$ after 650°C annealing for 1h (left); 700°C annealing for 1h (right)

From the fcc(111) peak, lattice parameter of 650°C annealed films is calculated to be 3.7980 Å **(Fig 4.23**, left**)**, and coercivity grows to around 5.9kOe in the in-plane direction and 5.4kOe in the out-of-plane directions. By further heat treatment in forming gas for 1h at 700°C, coercivities increased to 8.6kOe~8.8kOe in the two directions **(Fig 4.23**, right**)**. It is worth noting that since the hysteresis loops here are not saturated at 20kOe (the most common maximum applied field provided by current commercial VSMs), therefore the actual coercivity of the sample should be larger than the current value[124]. A more accurate coercivity value might be obtained by using VSM with a maximum applied field of 30kOe or more. From the kink in the magnetization curve after 700°C annealing, the amount of soft magnetic phase is estimated about 14%.

From the above, we see that this series of FeNiPt films have very similar behavior in structure and magnetic properties before and after annealing, however, the coercivity may vary widely. This demonstrates that coercivity is highly dependent on fine details of the microstructure that could only be understood by detailed investigations at the nm scale, utilizing TEM imaging and diffraction. In summary, FeNiPt films with a Pt content around 50% could transform from soft magnetic materials to very hard ones after 700°C annealing for 1h. The lattice parameters for the fcc phase for each sample after 650°C annealing are extracted from XRD patterns and compared with values calculated following Vegard’s law, which states that the lattice parameter is directly proportional to atomic percentage of the alloy (fcc-Fe: 3.591Å, fcc-Ni: 3.52Å, fcc-Pt: 3.92Å) in **Table 4.14**, in which we can see the error is below 1.7%, demonstrating good agreement between experimental lattice parameters and that calculated from Vegard’s law.

Applied potenital V. vs. MSE	Composition (EDS) Fe: Ni: Pt	Lattice parameter a’ from Vegard’s law (Å)	lattice parameter a from XRD (Å)	Error (%)
-1.22	38:7:55	3.76698	3.8137	1.22
-1.23	38:8:54	3.76298	3.7993	0.96
-1.24	39:11:50	3.74769	3.7943	1.23
-1.25	39:12:49	3.74369	3.7906	1.24
-1.26	40:13:47	3.7364	3.7866	1.33

-1.27	43:13:44	3.72653	3.7856	1.56
-1.28	42:12:46	3.73382	3.798	1.69

Table 4. 9 Comparison of lattice parameter from fcc(111) peak in XRD and from Vegard's law

The dependence of magnetic properties on film composition is also investigated.

potenital /V. vs. MSE	Composition Fe: Ni: Pt	Fe/Pt ratio	Thicknes s/nm	Hc_annealed at 650^{o}C/kOe	Hc_annealed at 700^{o}C/kOe
-1.22	38:7:55	0.69	~15	1.2	
-1.23	38:8:54	0.70	~20	3.4	
-1.24	39:11:50	0.78	~20	3.0	
-1.25	39:12:49	0.80	~20	3.3	7.2
-1.26	40:13:47	0.85	~20	3.4	
-1.27	43:13:44	0.98	~20	4.8	
-1.28	42:12:46	0.91	~30	5.9	8.8

Table 4. 10 The dependence of magnetic properties on composition; Hc stands for coercivity.

By comparing films deposited at -1.24 ~-1.27V vs. MSE with a stable Ni composition (11~13 at.%) and a thickness of 20nm, it can be concluded that the coercivity increases with the Fe/Pt ratio within the range of 0.78 to 0.98 (**Fig. 4.25**). Though film with composition Fe$_{38}$Ni$_{8}$Pt$_{54}$ deposited at -1.23V with a thickness of 20nm shows a Fe/Pt ratio smaller than 0.7, its relatively high coercivity (3.4kOe) can be explained by lower Ni content compared to other electrodeposited alloys (11-13 at% Ni), which is consistant with the findings from Li *et al*[64]., stating that adding Ni to ordered FePt intermetallic compound decreases anisotropy energy, leading to a decrease in coercivity.

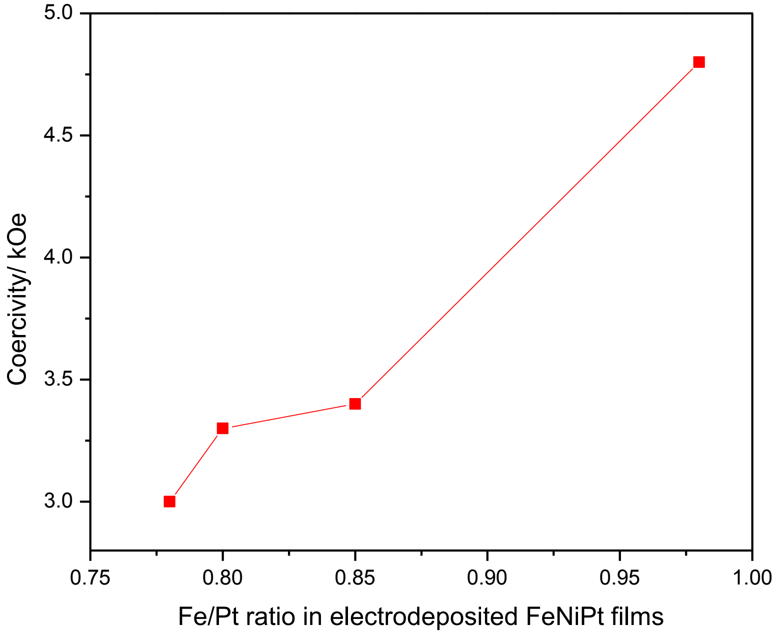

Fig 4. 25 Relationship between Fe/Pt ratio and coercivity.

After comparing magnetic properties of Ni-doped FePt films with a thickness around 20nm, we further compare properties in thicker films (~80nm) by generating a new series of thin films based on the same solution (30mM ferric sulfate), see below in **Table 4.11**. The relationship between deposition rate and potential is plotted in **Fig 4.26**.

Potential	Time	Composition	thickness
-1.22V	4h	$Fe_{30}Ni_8Pt_{62}$	~80nm
-1.24V	3.5h	$Fe_{32}Ni_{10}Pt_{58}$	~80nm
-1.26V	2.75h	$Fe_{30}Ni_{14}Pt_{56}$	~80nm
-1.28V	2h	$Fe_{39}Ni_{11}Pt_{50}$	~80nm

Table 4. 11 A new series of FeNiPt thin films with a thickness of 80nm deposited from solution with 30mM ferric sulfate

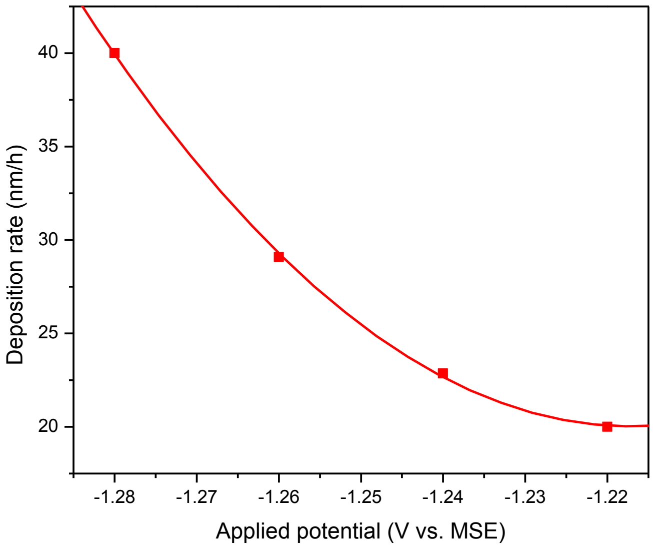

Fig 4. 26 Deposition rate for this set of FeNiPt deposition

Oxygen content was examined by EDS attached to a SEM (FEI Quanta 650) with an accelerating voltage of 5kV in high vacuum mode: data are summarized in **Table 4.12**. It turned out that oxygen content was significantly less than 10 at% in this set of films.

Potential	**Fe at.%**	**Ni at.%**	**Pt at.%**	**O at.%**
-1.22V	33.4	6.3	53.4	6.9
-1.24V	33.7	8.6	49.6	8.2
-1.26V	31.4	10.2	49.2	9.1
-1.28V	37.3	9.1	45.0	8.6

Table 4. 12 Oxygen content in the FeNiPt thin films

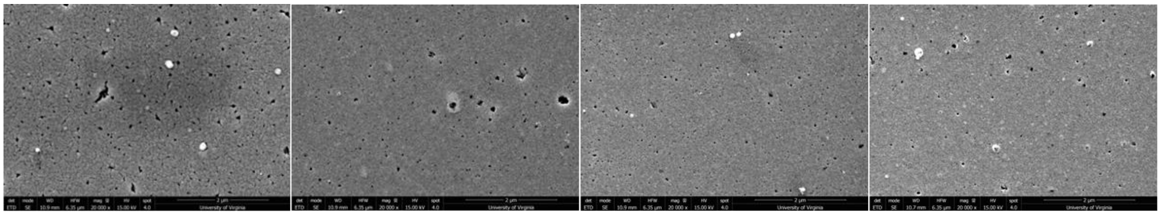

Fig 4. 27 SEI images of the same series of FeNiPt thin films which show relatively low porosity; applied potential decreases from left to right.

The plane-view images of these FeNiPt films all show significantly low porosity, which were estimated to be around 4.4%, 3.6%, 2.2% and 1.9%, respectively by using the software imageJ (**Fig 4.27**). Hydrogen formation and nucleation of bubbles remaining attached to the surface might be the reason leading to porosity.

a) For film $Fe_{30}Ni_{8}Pt_{62}$:

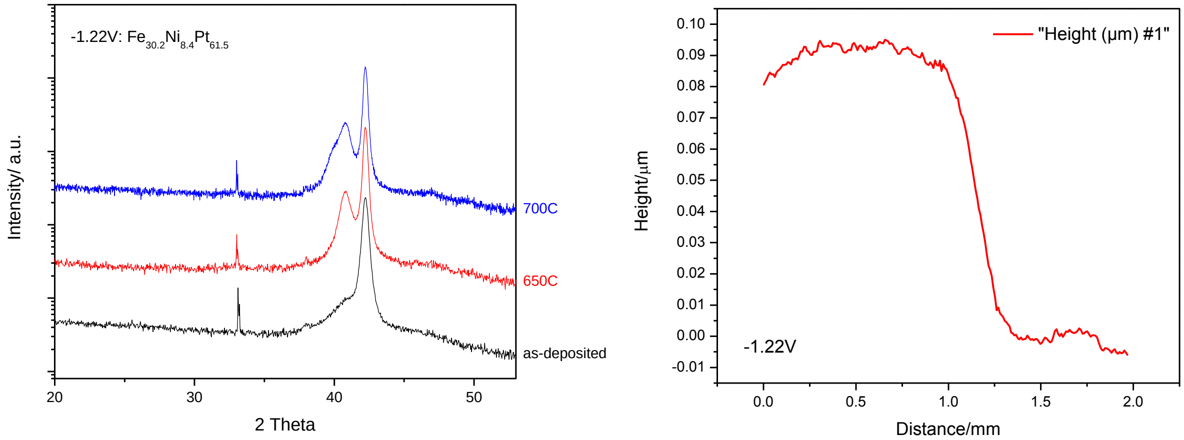

Fig 4. 28 XRD for as-deposited/650°C/700°C annealed $Fe_{30}Ni_{8}Pt_{62}$ film (left); film thickness measured by profilometer (right)

The film thickness is measured to be around 80nm by using profilometry, which was confirmed by cross-section images in the SEM (**Fig 4.16**). In as-deposited films, there is a very weak fcc(111) peak, and after annealing, the fcc (111) peak becomes more intense **(Fig 4.28**, left**)**. However, no (001) superlattice peak is observed after high temperature treatment up to 700°C for 1h.

The properties of film a, b, c and d are shown in the **Table 4.13**:

Applied Potential V vs. MSE	Composition (EDS) Fe: Ni: Pt	Fe/Pt ratio	Hc_650°C	Lattice Constant_650°C	Hc_700°C
-1.22	30:8:62	0.48	289Oe	3.8253	2.6kOe
-1.24	32:11:57	0.56	1.4kOe	3.8143	4.0kOe
-1.26	30:13:57	0.53	1.4kOe	3.8082	2.6kOe
-1.28	39:11:50	0.78	3.9kOe	3.7927	7.6kOe

Table 4. 13 comparison of thin film properties (film a, b, c and d)

The images below show in order: cross sectional images of the films and miscellaneous structural and magnetic properties from this set of films.

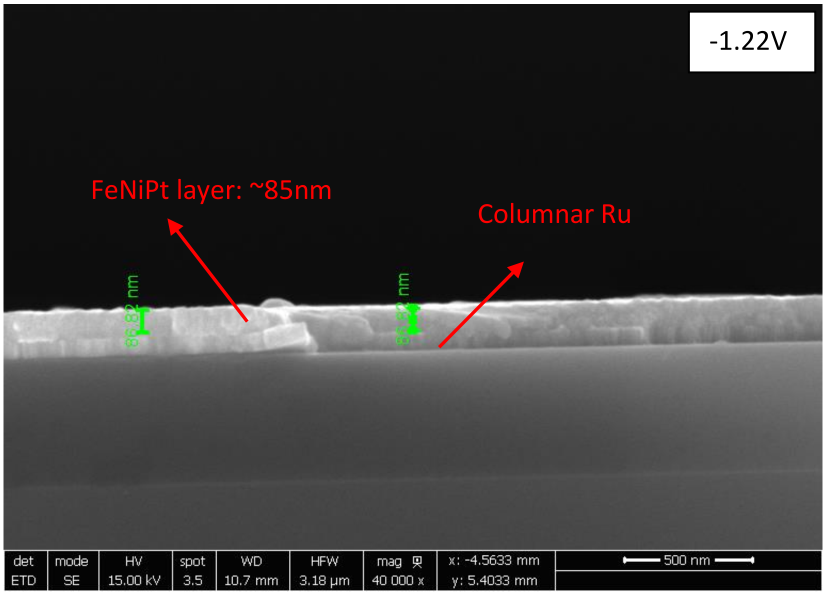

Fig 4. 29 Selected cross-sectional SEM images of FeNiPt films showing the thickness of film deposited at -1.22V vs. MSE.

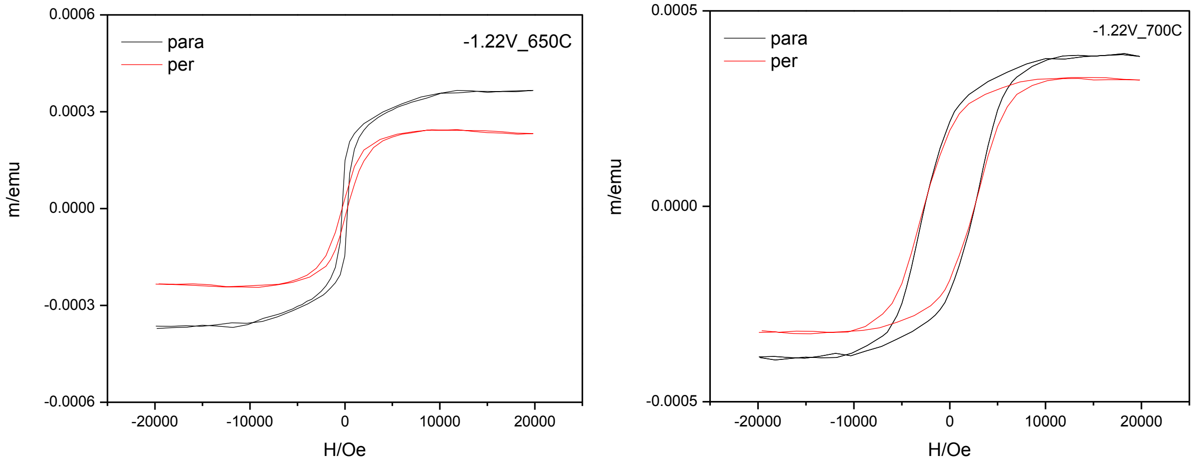

Fig 4. 30 Hysteresis loops for film $Fe_{30}Ni_{8}Pt_{62}$ after 650°C and 700°C annealing, respectively

b) For film $Fe_{32}Ni_{11}Pt_{57}$:

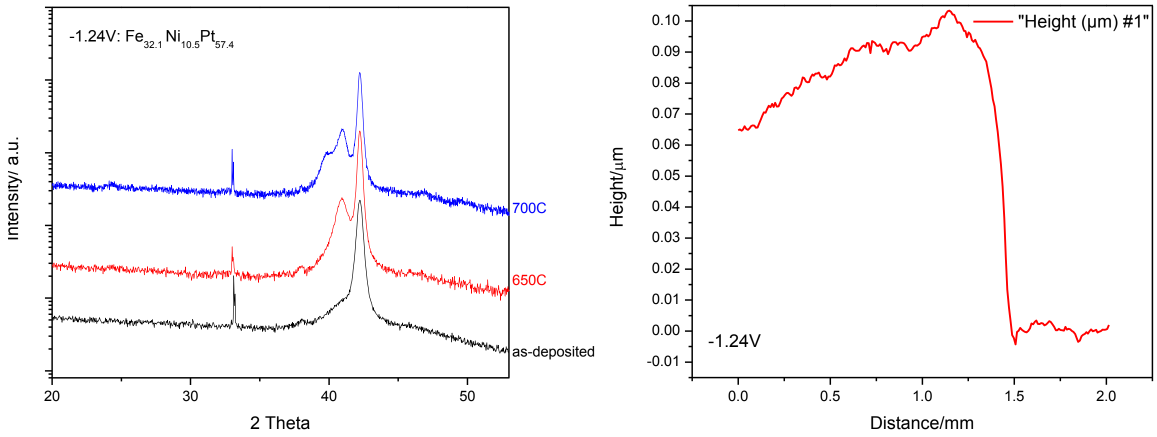

Fig 4. 31 XRD for as-deposited/650°C/700°C annealed $Fe_{32}Ni_{11}Pt_{57}$ film (left); film thickness measured by profilometer (right)

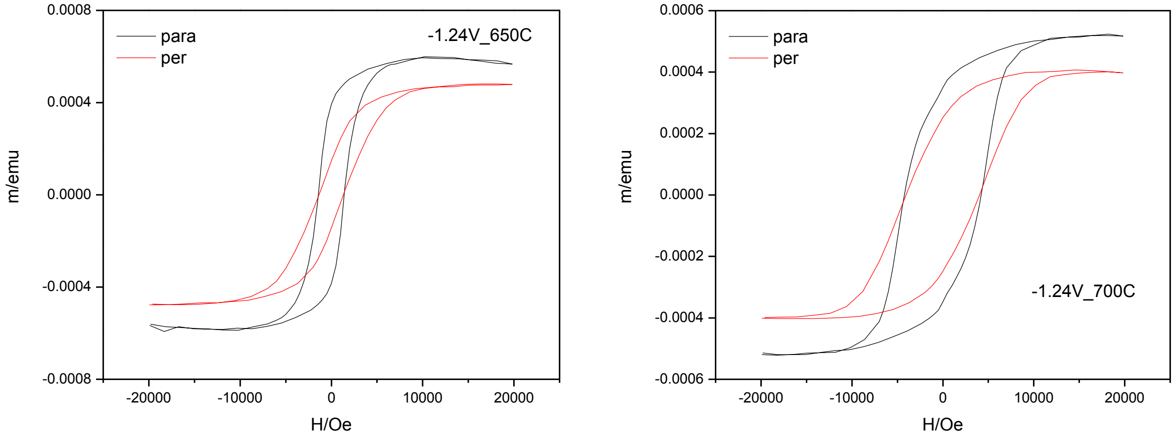

Fig 4. 32 Hysteresis loops for film $Fe_{32}Ni_{11}Pt_{57}$ after 650°C and 700°C annealing, respectively

c) For film $Fe_{30}Ni_{13}Pt_{57}$:

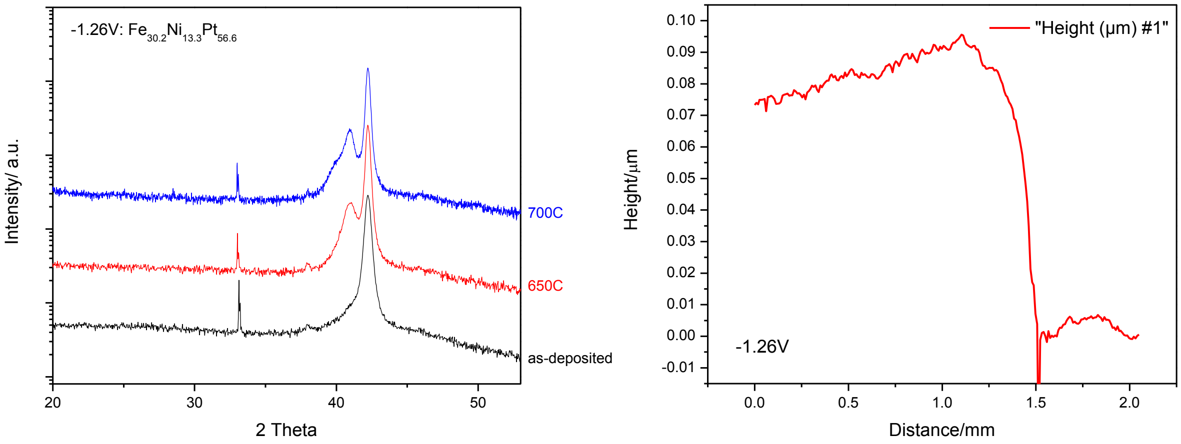

Fig 4. 33 XRD for as-deposited/650°C/700°C annealed $Fe_{30}Ni_{13}Pt_{57}$ film (left); film thickness measured by profilometer (right)

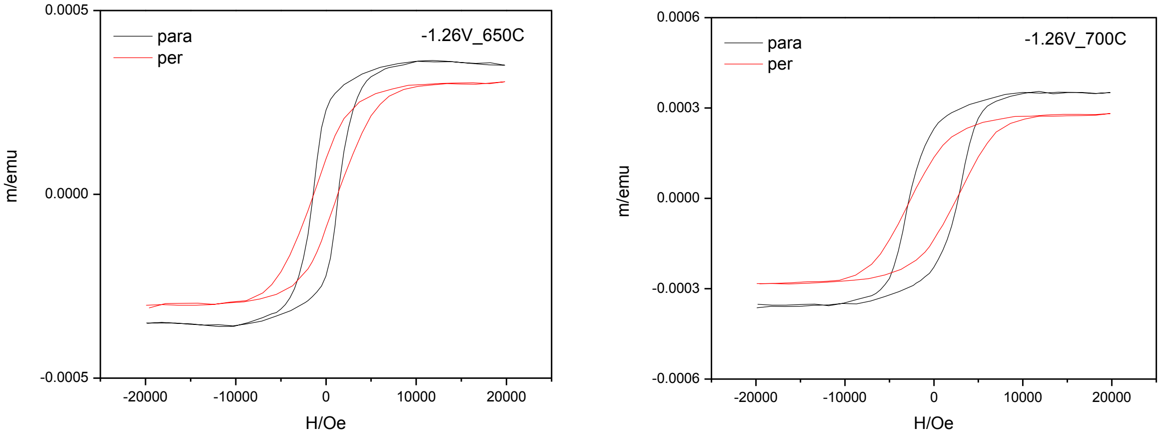

Fig 4. 34 Hysteresis loops for film $Fe_{30}Ni_{13}Pt_{57}$ after 650°C and 700°C annealing, respectively

d) For film $Fe_{39}Ni_{11}Pt_{50}$:

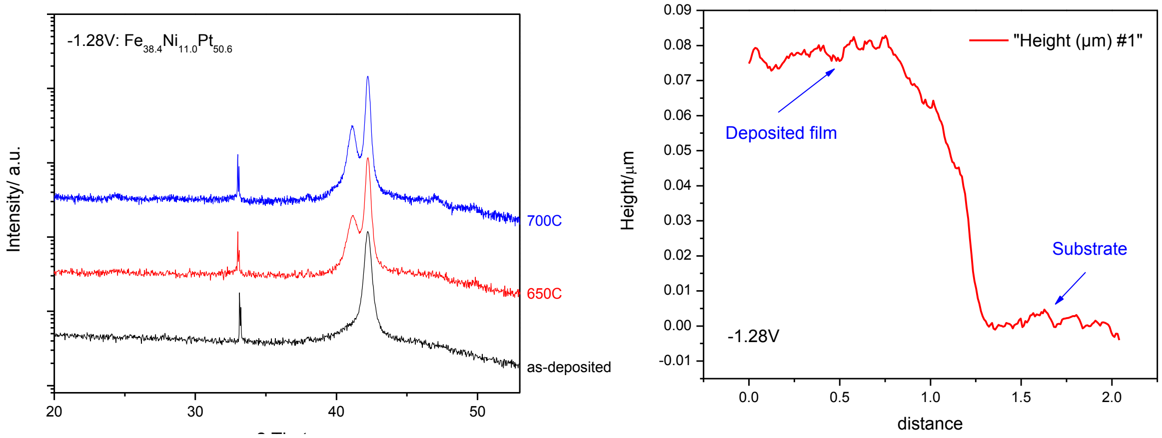

Fig 4. 35 XRD for as-deposited/650°C/700°C annealed $Fe_{39}Ni_{11}Pt_{50}$ film (left); film thickness measured by profilometer (right)

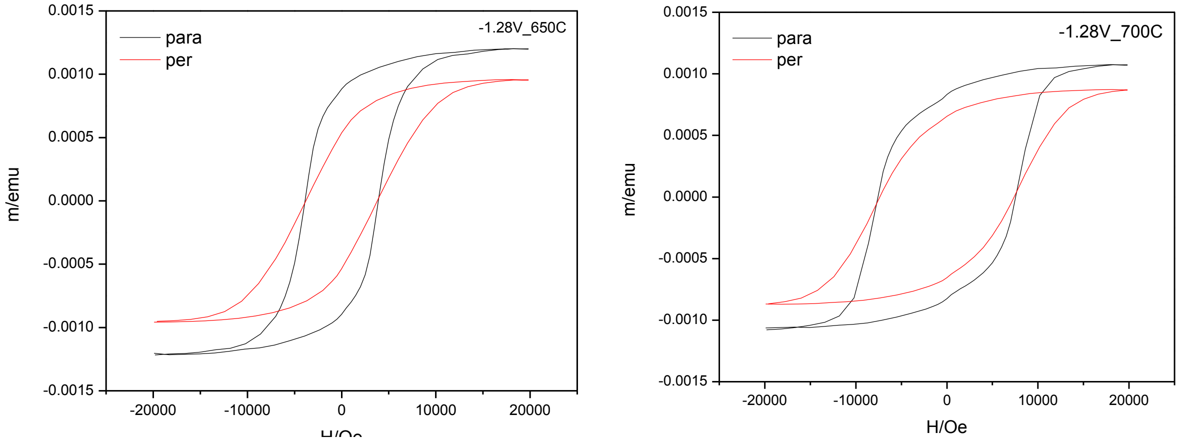

Fig 4. 36 Hysteresis loops for film $Fe_{39}Ni_{11}Pt_{50}$ after 650°C and 700°C annealing, respectively

By comparing sample $Fe_{32}Ni_{11}Pt_{57}$ and $Fe_{30}Ni_{13}Pt_{57}$, we can find that when the Pt content is fixed, coercivity is approximately the same after 650°C heat treatment for 1h. However, film $Fe_{32}Ni_{11}Pt_{57}$ with a lower Ni content shows significantly larger coercivity after 700°C annealing. Comparison of the samples $Fe_{32}Ni_{11}Pt_{57}$ and $Fe_{39}Ni_{11}Pt_{50}$ suggests that when Ni content is the same, a higher Fe/Pt ratio yields higher coercivity. Generally, we found that the coercivity tends to increase with increasing Fe/Pt ratio in annealed FeNiPt thin films; besides, with the Pt content closer to 50%, the coercivity becomes larger, consistent with results from other groups[125]; after 700°C annealing for 1h, coercivities are more than doubled compared to the annealing condition of 650°C for 1h (**Fig 4.37**).

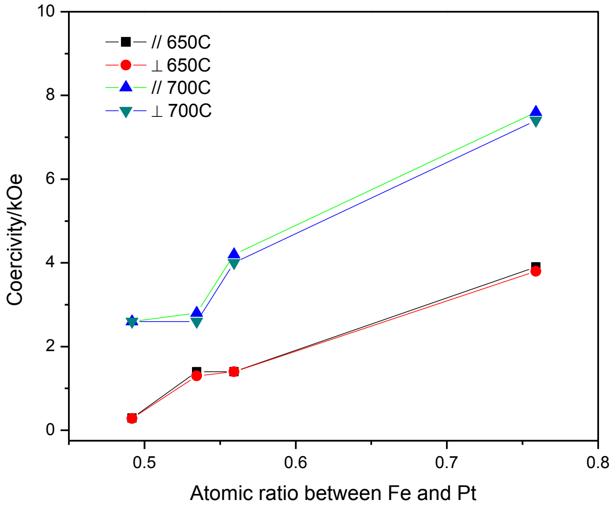

Fig 4. 37 Coercivity dependence on Fe/Pt ratio given Ni content is roughly around 10%

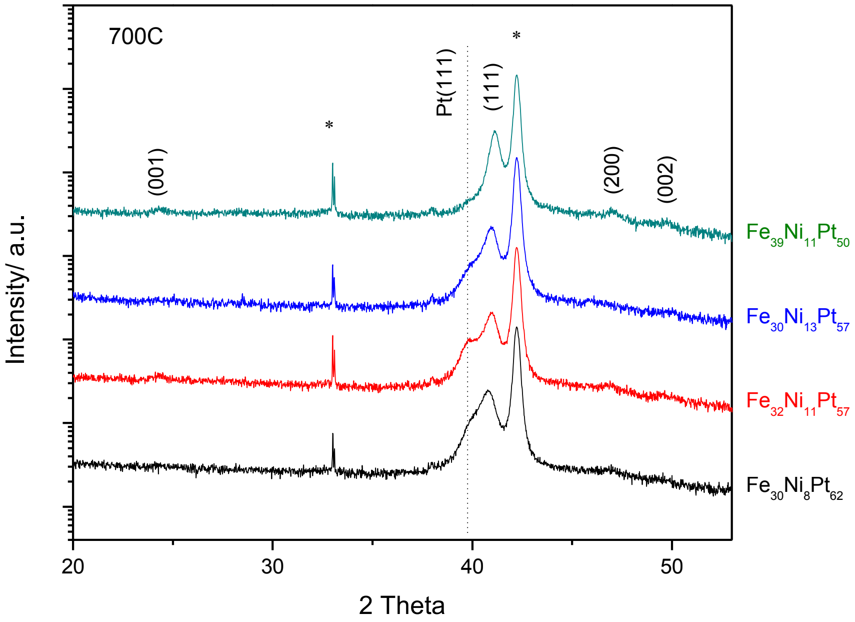

Fig 4. 38 XRD patterns for FeNiPt thin film annealed at 700°C for 1h

From XRD patterns for FeNiPt thin films annealed at 700°C for 1h (**Fig 4.38**), we can see that the FCC(111) peak of the alloy is present in all films; the absence or low intensity of other peaks from the FCT structure suggests that the main phase in the films is still the FCC phase[126]. The presence of the Pt(111) peak in samples $Fe_{32}Ni_{11}Pt_{57}$ and $Fe_{30}Ni_{13}Pt_{57}$ indicates that the addition of Ni into FePt films increases the ordering temperature, which may be attributed to the decrease of diffusivity of Fe and Pt atoms by alloying with Ni.

Among the above four samples, we further study the temperature dependence of coercivity and normalized magnetization m=M(T)/M(100K) for the $Fe_{39}Ni_{11}Pt_{50}$ film annealed at 700°C for 1h, with the magnetization M measured under an applied field of 25kOe in **Fig 4.39**.

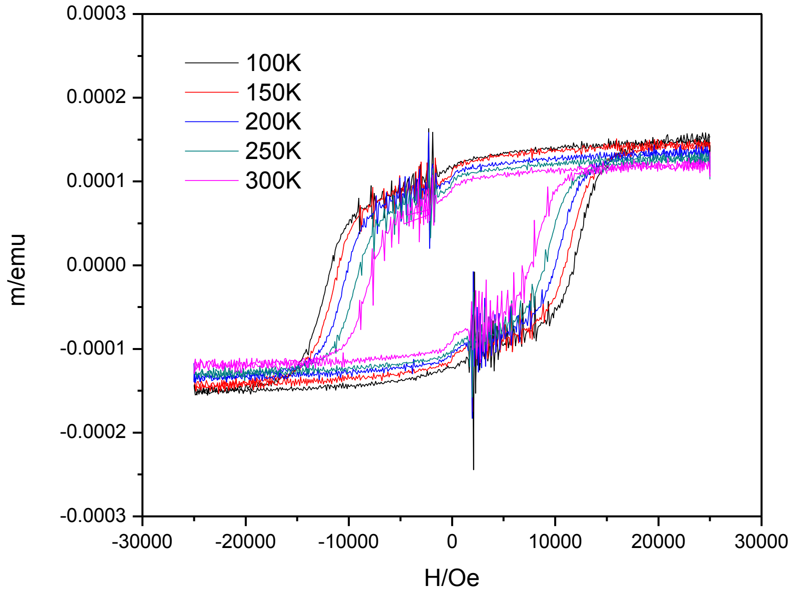

Fig 4. 39 M-H loops for $Fe_{39}Ni_{11}Pt_{50}$ (80nm) at different temperatures (courtsey of Linqiang Luo)

In **Fig 4.40**, coercivity drops steadily from 11.7kOe to 7.8kOe when temperature changes from 100K to 300K while magnetization drops around 20%. Similar behaviors have been observed by Thiele[63] *et al* and Yan *et al*[68].

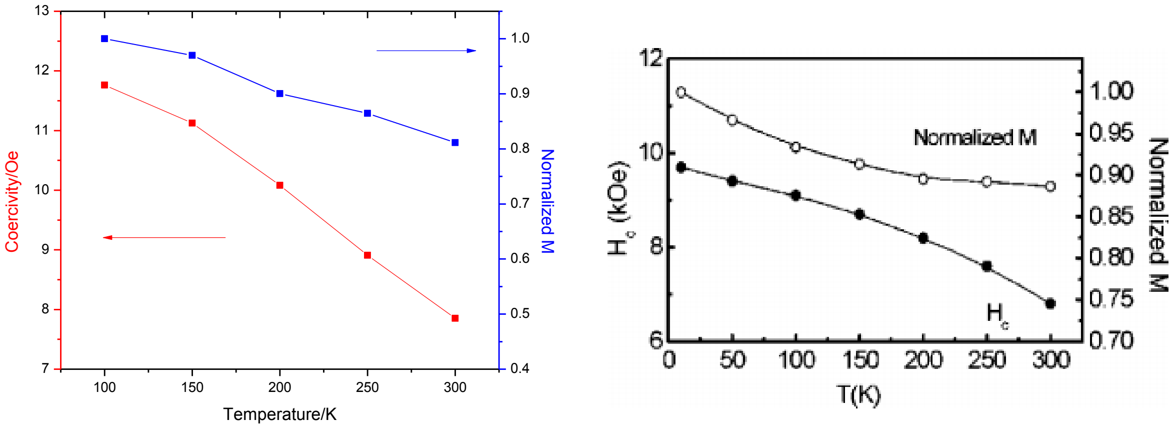

Fig 4. 40 Temperature dependence of normalized magnetization and coercivity for $Fe_{39}Ni_{11}Pt_{50}$ with our group (left), [Fe(0.38nm)/Ni(0.04nm)/Pt(0.4nm)]13 from Yan *et al* (right).

5. Electrodeposition and magnetic properties of high permeability permalloy

5.1. The development of electrolytes for $Fe_{19}Ni_{81}$ and Pt-doped $Fe_{19}Ni_{81}$

In this section we utilize an electrolyte chemistry similar to that used in prospective HAMR materials to target a different compositional range in the same ternary system, namely a composition close to permalloy, with small Pt addition. The reason for the study of this alloy is that the addition of rare earth and noble elements to Permalloy are capable to increase magnetization damping, possibly resulting in faster magnetization switching in magnetic heads. Shiny and continuous NiFe films were first obtained from the electrolyte discussed above; the composition of films vs. applied potential was studied using different Ni^{2+}/Fe^{3+} ratios in different solutions (**Fig 5.1**). The composition of specimens were examined by EDS attached to the JEOL 6700 SEM. We also tried to study the morphology of permalloy films by SEM, however, the super smooth surface makes the imaging process rather difficult, nearly impossible.

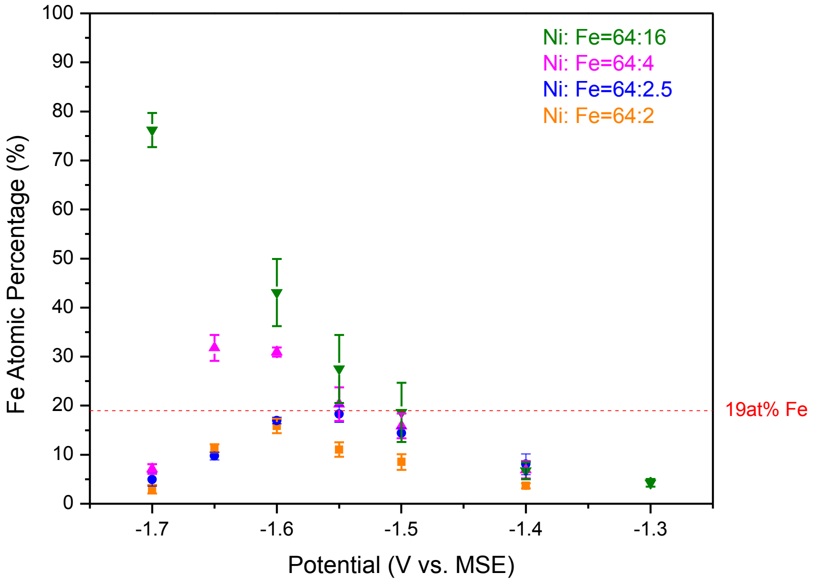

Fig 5. 1 Composition of FeNi alloys for solutions with varying Ni^{2+}/Fe^{3+}

For solutions with a large excess of nickel species in the electrolyte (factor of 32, 25.6 and 16), Fe content in the as-deposited films first increases and then decreases with the applied potential going more negative, and all films show a Fe atomic percentage below 35%. For the solution with a Ni^{2+}/Fe^{3+} ratio of 64:16, Fe content increases with more negative potential and reaches a percentage as high as 76.2±3.48 at.% in a film deposited at -1.7 (V v. MSE). In solutions with Ni^{2+}/Fe^{3+} ratio of 64:2.5, 64: 4 and 64:16, a $Ni_{81}Fe_{19}$ film is obtained at the potential of -1.55V, -1.55V and -1.5V respectively (**Fig 5.2**).

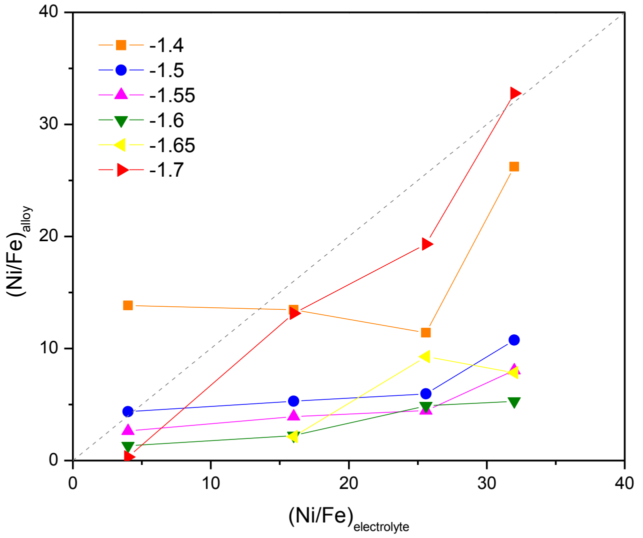

Fig 5. 2 Comparison of the (Ni/Fe) in electrolyte and that in the as-deposited films

Ni/Fe ratios in the as-deposited films are lower than that in the electrolyte, suggesting the well-known anomalous codeposition effect of NiFe codeposition[127].

After having obtained $Ni_{81}Fe_{19}$films from various solution, we add 0.1mM Pt-p-salt into a solution of Ni^{2+}/Fe^{3+} = 64:4 to produce Pt-doped permalloy. The results are shown in **Fig 5.3**: a composition plateau is found between -1.55V ~ -1.65V, with Fe content around

20at.% and Pt ~2 at.%. We further study the composition dependence on deposition time (**Fig 5.4**); though the average Fe content deposited at -1.6V for different deposition time still has a value roughly around 20 at%, a large composition deviation is found across the film (three spots are used to collect the composition information for each specimen: bottom, center and top, and we already avoided measuring the corners of the film in consideration of the edge effect[128, 129]).

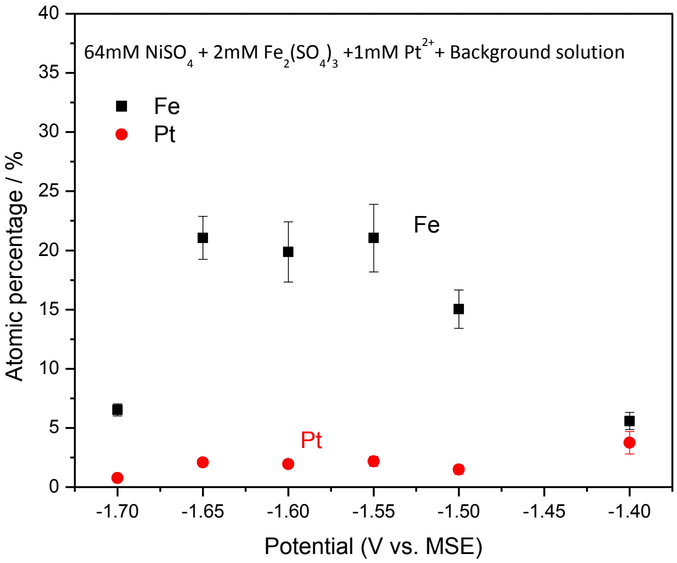

Fig 5. 3 Composition of Pt-doped permalloy from solution: 4mM Fe^{3+}+64mM Ni^{2+}+1mM Pt-p-salt.

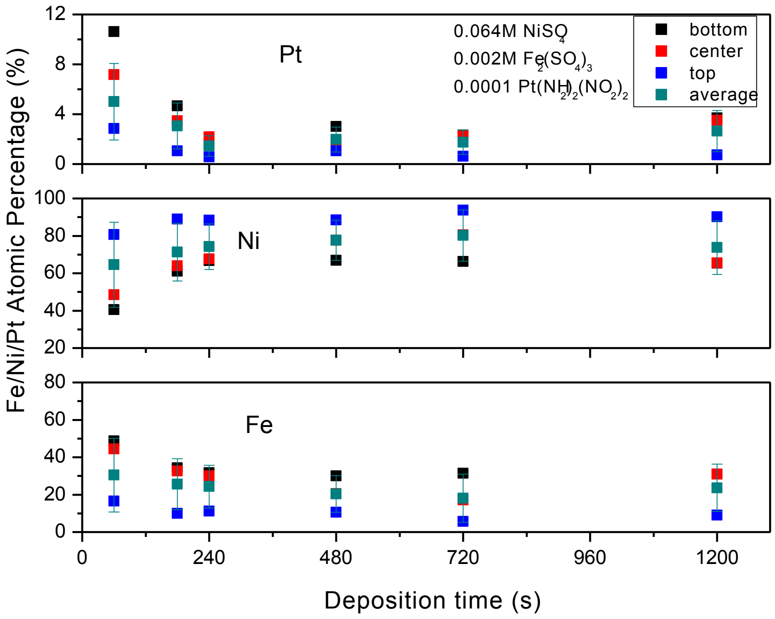

Fig 5. 4 Composition dependence on deposition time when applied potential is -1.6 V vs. MSE.

To improve the homogeneity of the thin films, we decided to change our three-electrodes with vertical configuration to horizontal configuration, and the composition variance was confirmed to be significantly reduced from around 30% to 7% or less:

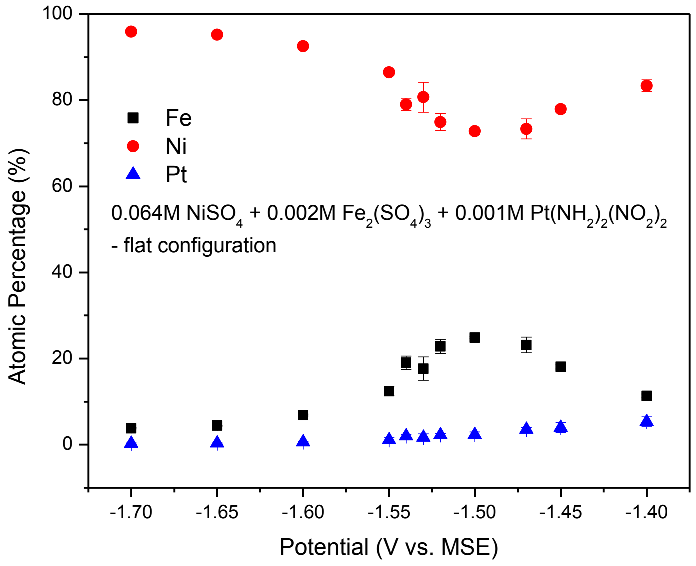

Fig 5. 5 Composition of FeNiPt films deposited from a cell with parallel configuration.

From the composition dependence on applied potential shown in **Fig 5.5**, we found that the Fe content reached a maximum of 25 at% at the potential of -1.50V vs. MSE, and desired FeNiPt films were obtained within the potential range of -1.45V~-1.54V; the relative deposition rates are calculated and compared in **Fig 5.6**; it is clear that with the potential going more negative, the deposition rate increases. More importantly, all the composition deviation is rather small compared to films we deposited from vertical cell configuration.

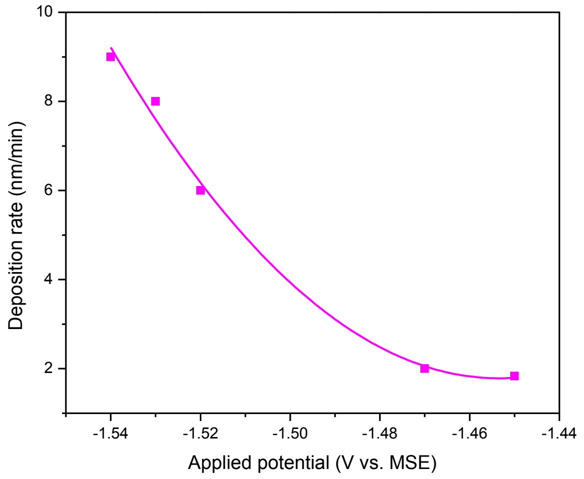

Fig 5. 6 Deposition rate for Pt-doped permalloy films within the deposition potential range (-1.45~-1.54V vs. MSE)

Composition (EDS) Fe: Ni: Pt	Applied Potentia/V	Deposition time/min	thickness /nm	Magnetization / emu·cc^{-1}	$H_{c,//}$/Oe	Mr/Ms	$H_{c,\perp}$/Oe
19:79:2	-1.45	30	55	180	6	0.963	98
18:80:2	-1.47	20	40	441	11	0.928	131
23:75:2	-1.52	10	60	354	14	0.985	214
23:73:4	-1.53	10	80	441	14	0.982	248
18:78:4	-1.54	10	90	358	20	0.984	238

Table 5. 1 Characterization of Pt-doped permalloy deposited from -1.45V ~-1.54V

In **Table 5.1**, all the films deposited within the potential range of -1.45V to -1.54V (**Fig 5.5**) were listed with corresponding deposition conditions and measured properties. All magnetization loops are given in **Fig 5.7 ~ 5.11** for both in-plane and out-of-plane directions. High M_r/M_s ratios (>0.92) were observed in in-plane magnetization curves for all films.

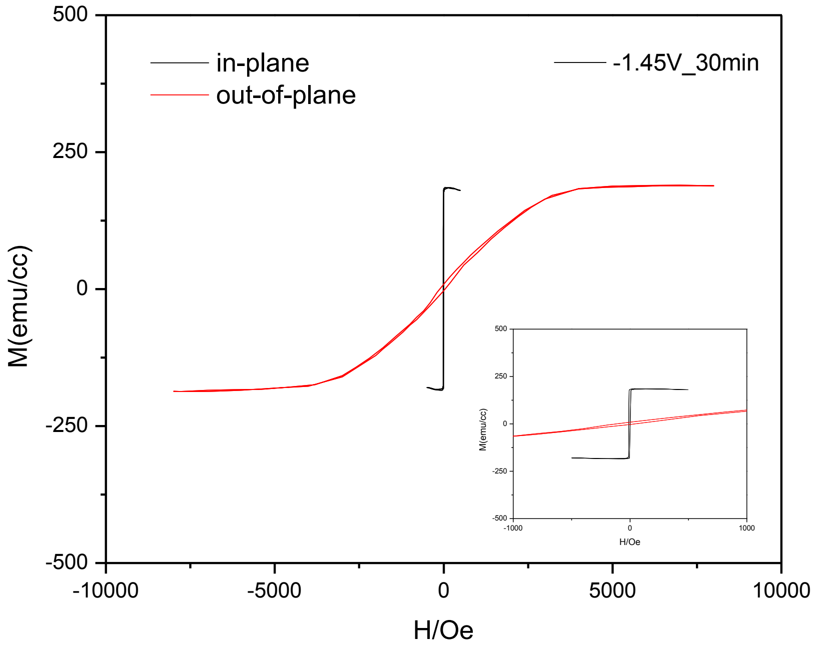

Fig 5. 7 Magnetization curves for sample deposited at -1.45V

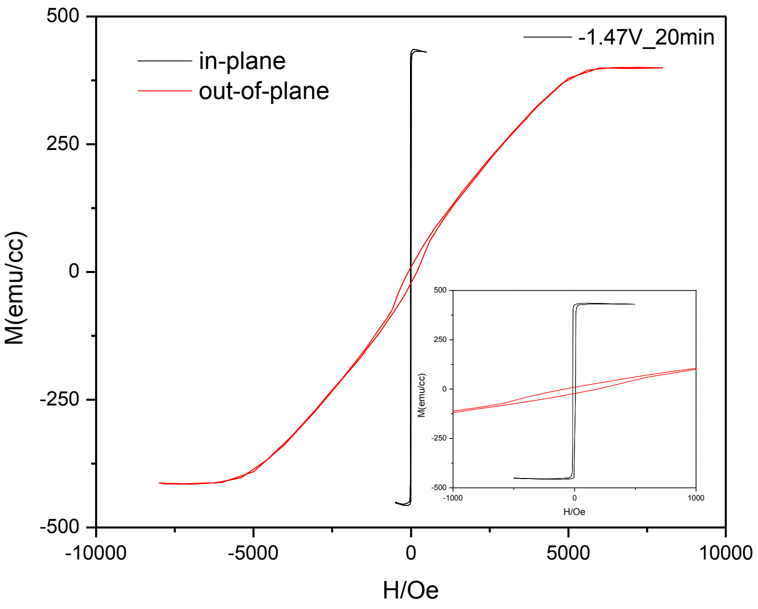

Fig 5. 8 Magnetization curves for sample deposited at -1.47V

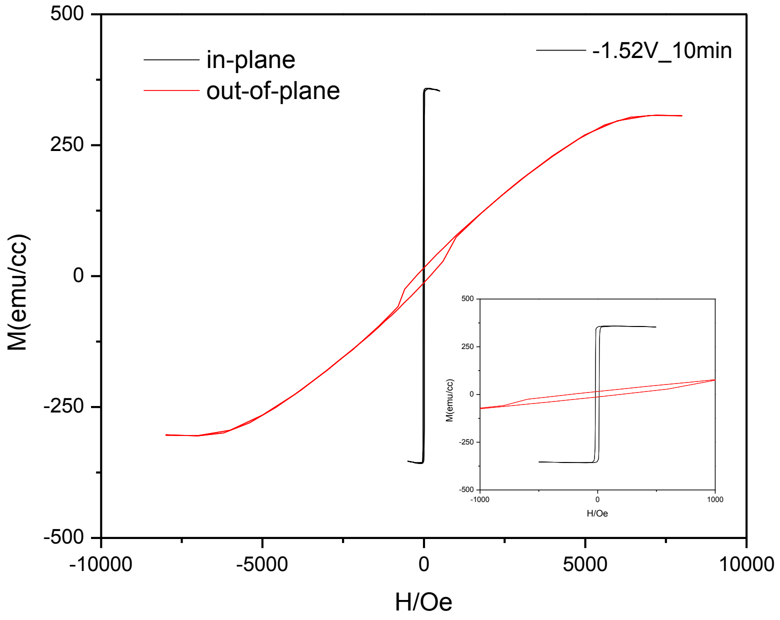

Fig 5. 9 Magnetization curves for sample deposited at -1.52V

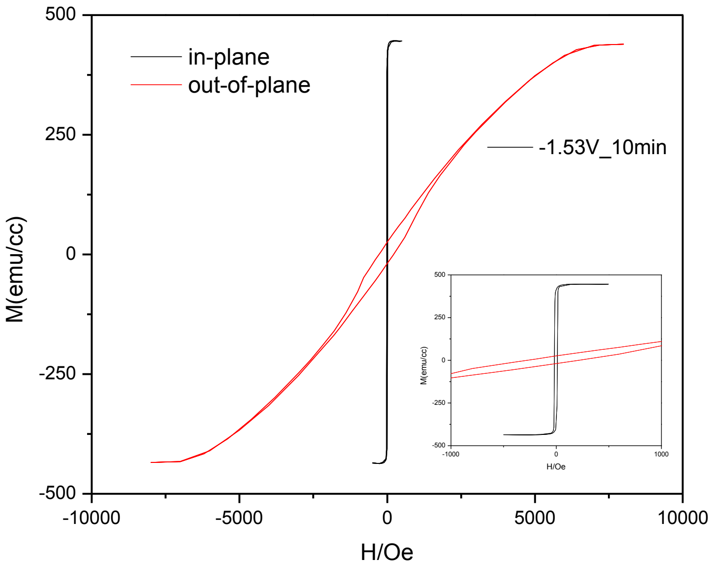

Fig 5. 10 Magnetization curves for sample deposited at -1.53V

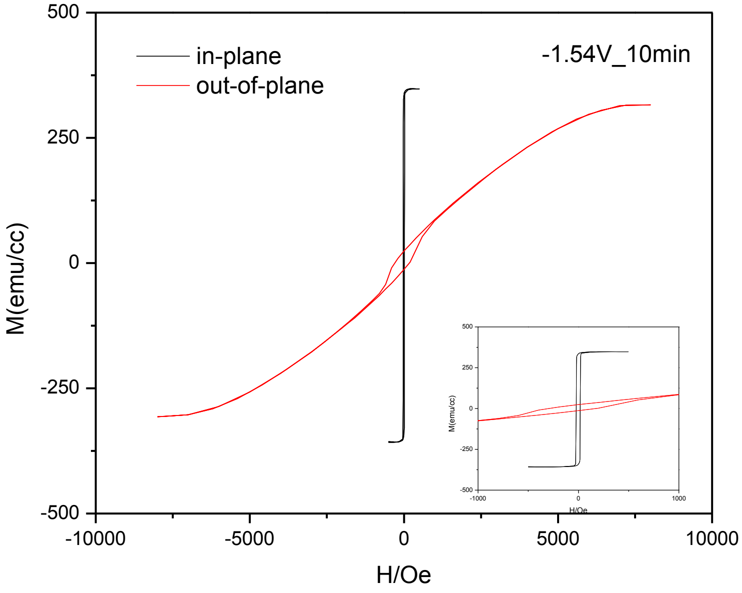

Fig 5. 11 Magnetization curves for sample deposited at -1.54V

Based on results above, one future plan of work is to anneal those films at moderate temperatures, which is expected to relieve stress in the film, therefore, decreasing the coercivity[130]. **Fig 5.12** shows another set of permalloy and Pt-doped permalloy thin film materials that can be adopted to study the influence of Pt addition on magnetic properties of permalloy.

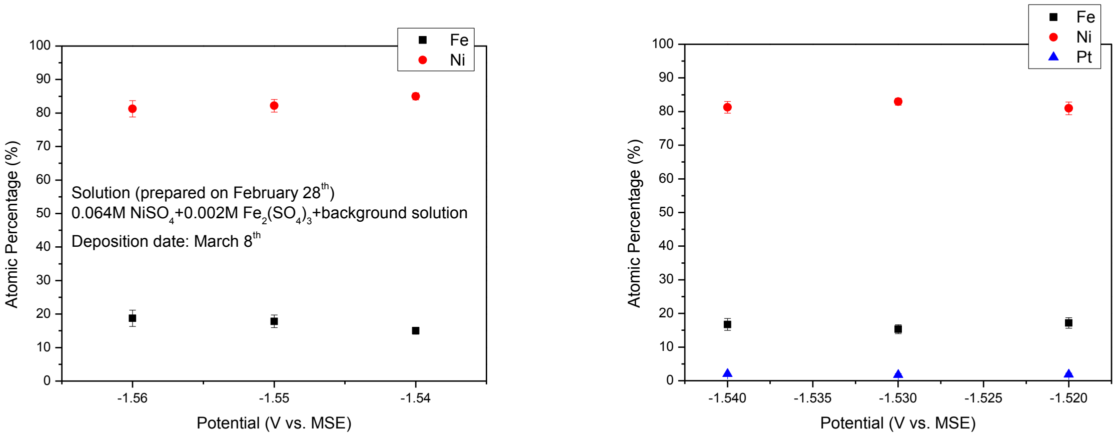

Fig 5. 12 FeNi and FeNiPt deposition from a parallel cell configuration

5.2. Properties of equiatomic FeNi

Equiatomic Fe-Ni was grown by using the same basic electrolyte as above, varying the relative concentration of Fe and Ni to target the desired composition.

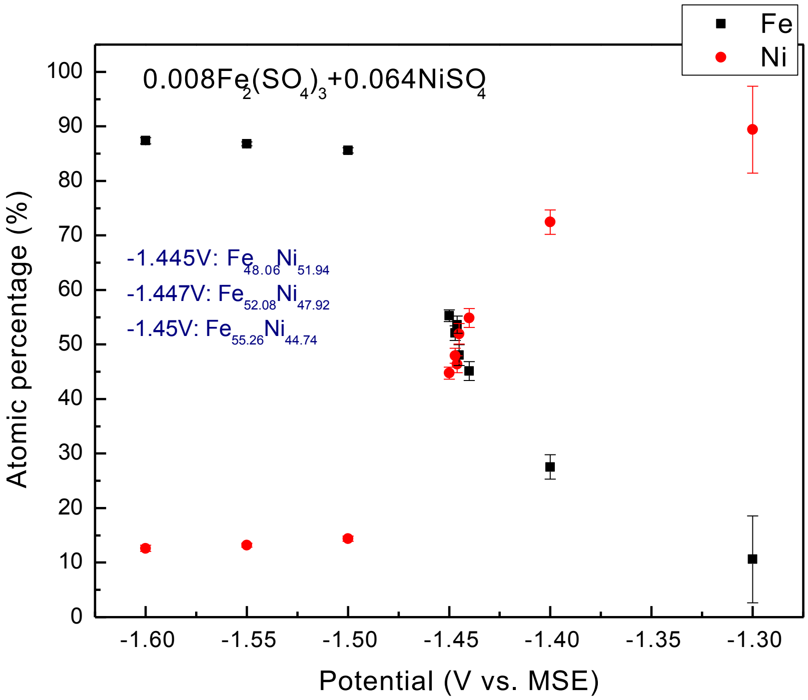

Fig 5. 13 Composition dependence on applied potential for FeNi electrodeposition

Fe content in the as-deposited films increases and Ni content decreases with the potential going more negative. Intermediate potentials yield composition close to the equiatomic value (**Fig 5.13**).

Table 5.2 shows the deposition conditions, composition and saturation magnetization (M_s) of three selected FeNi thin film alloys. Thickness of these as-deposited films were determined by SEM images, selected image showing the thickness of $Fe_{55}Ni_{45}$ is given in **Fig 5.14**.

	1	2	3
Potential	-1.44V	-1.443V	-1.446V
Composition	$Fe_{49.37}Ni_{50.63}$	$Fe_{49.41}Ni_{50.59}$	~ $Fe_{55}Ni_{45}$
Deposition time/min	15	10	10
Lattice parameter/nm, fcc(111) peak	0.3554	0.3545	0.3547
Lattice parameter(Vigard's law)	0.3555	0.3555	0.3559
Thickness	~120nm	~75nm	~80nm
Area/cm^2	0.2	0.4	0.39
Volume/cm^3	$2.4*10^{-7}$	$3*10^{-7}$	$3.12*10^{-7}$
M_s-para/emu	0.002687	0.004947	0.0047
M_s-para/V (emu/cm^3)	1120	1649	1506.4

Table 5. 2 Comparison of three FeNi samples

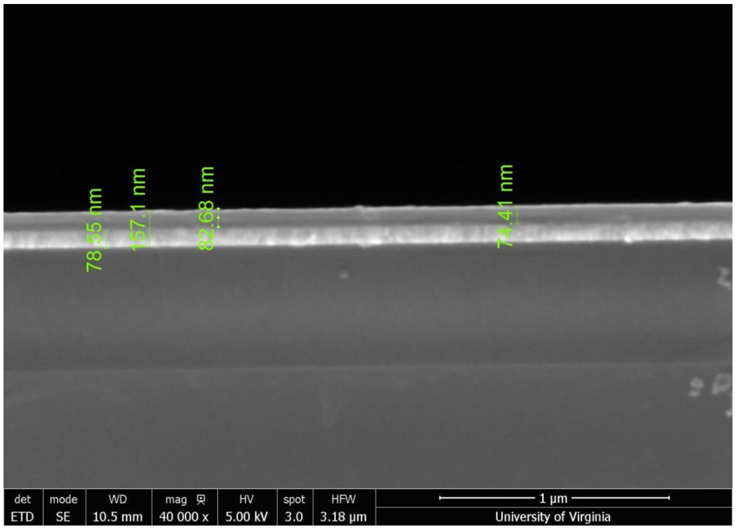

Fig 5. 14 Cross-section images of selected as-deposited $Fe_{55}Ni_{45}$ sample

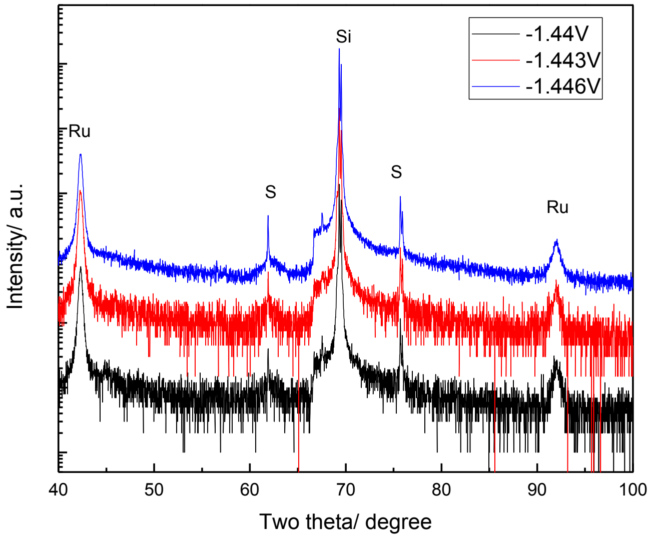

Fig 5. 15 XRD patterns for three as-deposited FeNi thin films

Fig 5.15 shows the XRD patterns for the selected equiatomic FeNi thin films, no apparent peak from FeNi is observed. However, after annealing at 400ºC in the forming gas for 1h, there appeared a peak around 43.8º in all three films (**Fig 5.16**); whether this represents the fct (110) reflection[94,131] is under examination.

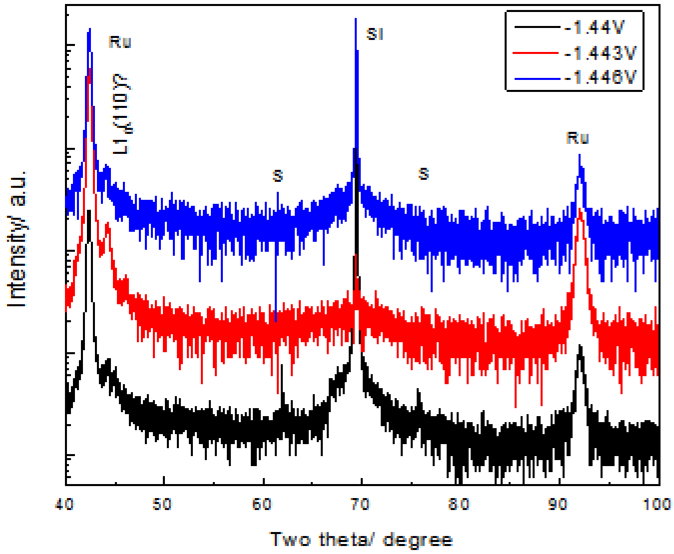

Fig 5. 16 XRD patterns for three FeNi thin films annealed at 400ºC for 1h

The magnetization curves for each FeNi sample before and after 400^{o}C annealing in the forming gas for 1h are shown in **Fig 5.17** to **Fig 5.19**. In each sample, coercivity grows after heat treatment at 400^{o}C, with a value ranging from 440 Oe to 680 Oe. The shape of the out-of-plane magnetization curves together with the coercivity are both similar to that reported in the natural formed meteorite NWA 6259**Error! Bookmark not defined.** measured at 295K.

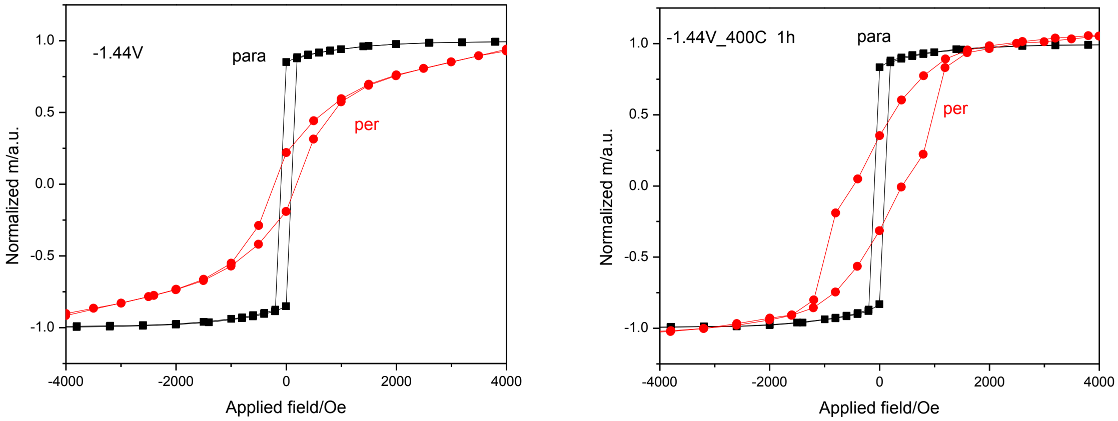

Fig 5. 17 VSM for Fe$_{49}$Ni$_{51}$ deposited at -1.44V vs. MSE before and after 400^{o}C annealing.

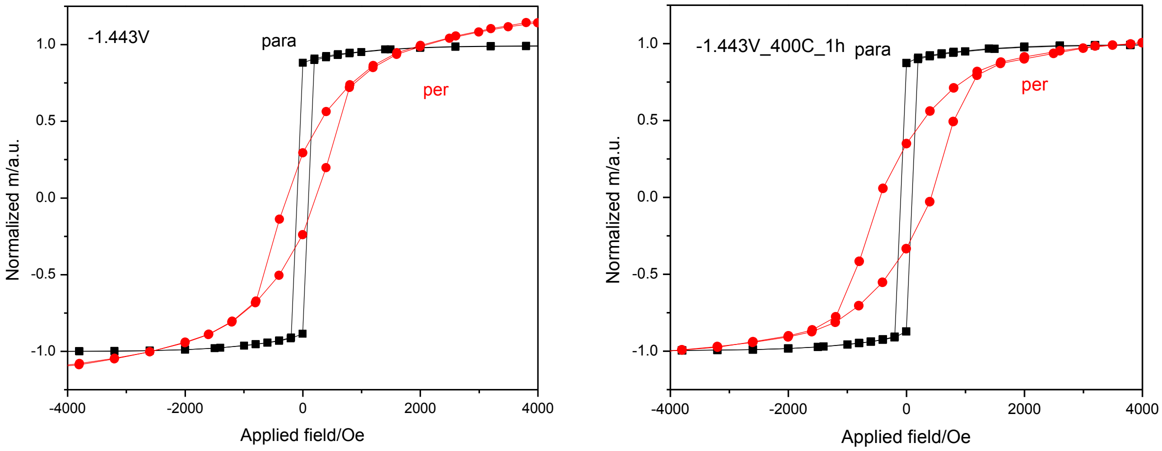

Fig 5. 18 VSM for Fe$_{49}$Ni$_{51}$ deposited at -1.443V vs. MSE

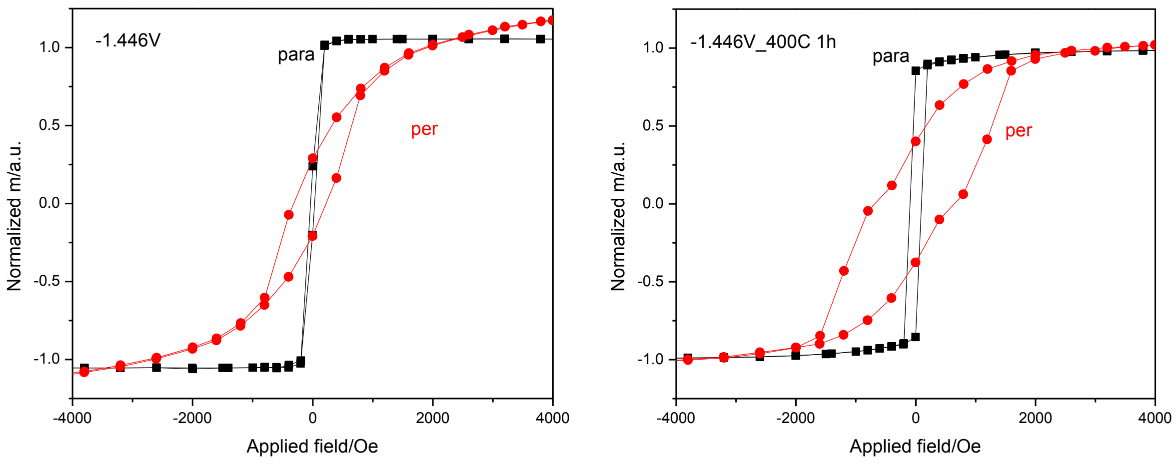

Fig 5. 19 VSM for $Fe_{55}Ni_{45}$ deposited at -1.446V vs. MSE

Another set of as-deposited FeNi thin films with thickness of around 500nm (**Fig 5.20**) were also deposited, see in **Table 5.3**.

sample	1	2	3
Potential	-1.46V	-1.463V	-1.465V
Composition	$Fe_{49}Ni_{51}$	$Fe_{55}Ni_{45}$	$Fe_{56}Ni_{44}$
Thickness/nm (Zygo)	484±15	476±24	453±20
Thickness/nm (SEM)	488	492	516
Coercivity/Oe	520	680	990

Table 5. 3 As-deposited FeNi thin films deposited for 45min

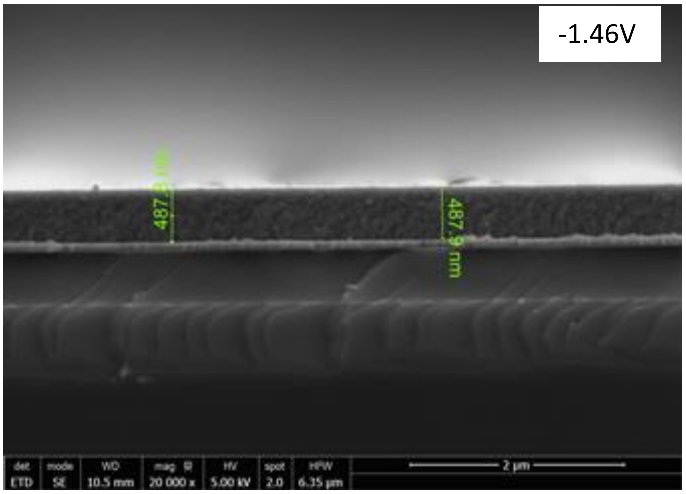

Fig 5. 20 Cross-sectional image of $Fe_{49}Ni_{51}$ thin film

Coercivity of these films reach values of 520 Oe, 680 Oe and 1kOe, respectively, even without further heat treatment (**Fig 5.20** and **Fig 5.21**). A shoulder peak from the as-deposited FeNi shows up in their XRD patterns (**Fig 5.22**), with a similar position- about 43-44 degrees –as that in annealed FeNi thin films (**Fig 5.16**). An important task in the future is to identify the phase related to this peak, which may ultimately help to explain the large coercivity observed.

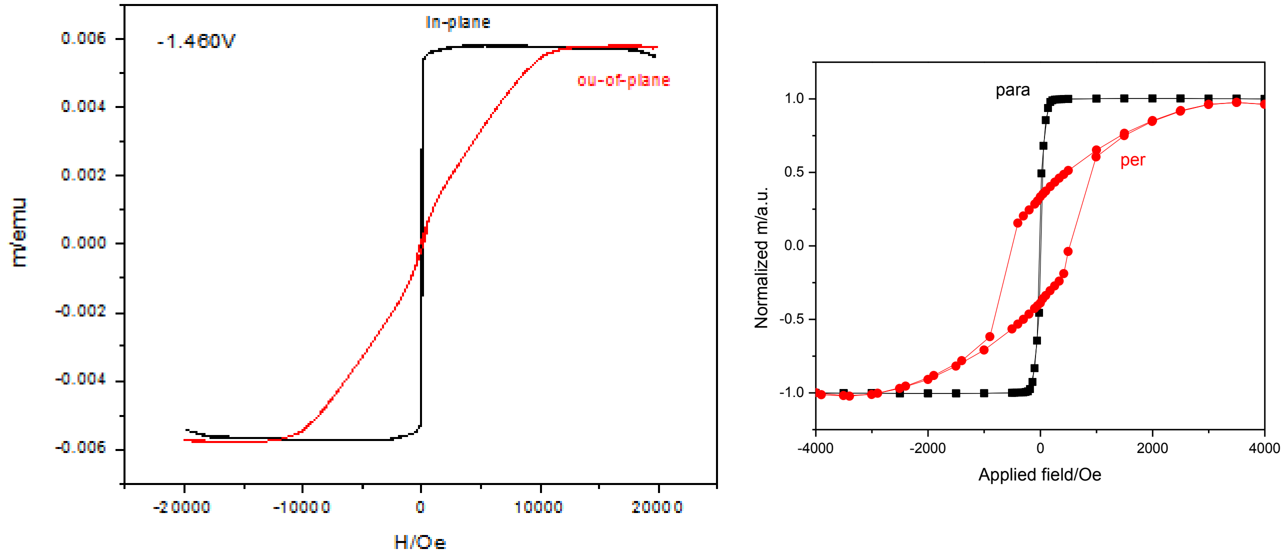

Fig 5. 21 Magnetization curves for as-deposited $Fe_{49}Ni_{51}$ with different applied field ranges (left: -20kOe~20kOe, right: 4kOe~4kOe)

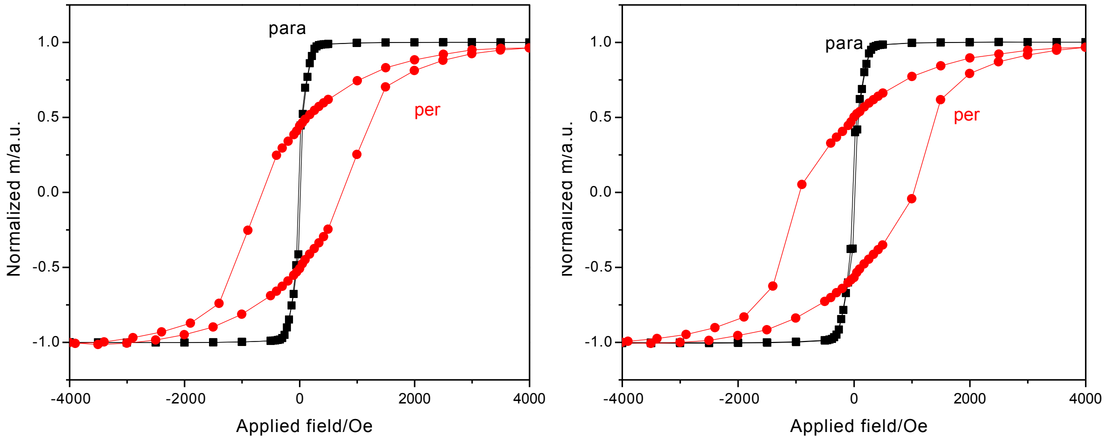

Fig 5. 22 Magnetization curves for as-deposited $Fe_{55}Ni_{49}$ (left) and $Fe_{56}Ni_{44}$ (right) thin films with applied field: -4kOe~4kOe

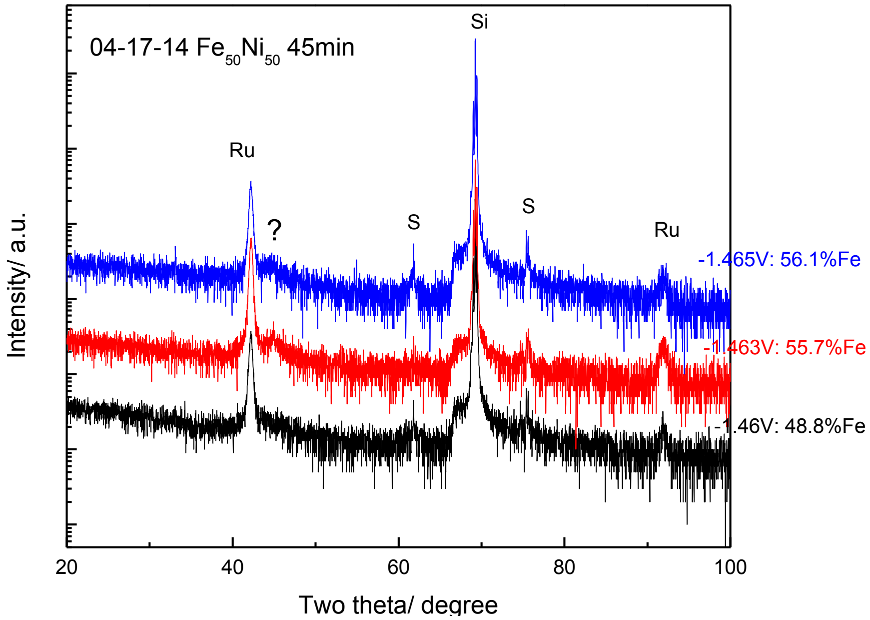

Fig 5. 23 XRD patterns for the as-deposited FeNi thin films with a thickenss of 500nm

Finally, a Fe47Ni53 thin film with a thickness of around 100nm was selected to study the structure and magnetic properties dependence on annealing temperatures. In **Fig 5.26**, it is clear that the peak around 44^{o} that we are interested in becomes more intense after annealing.

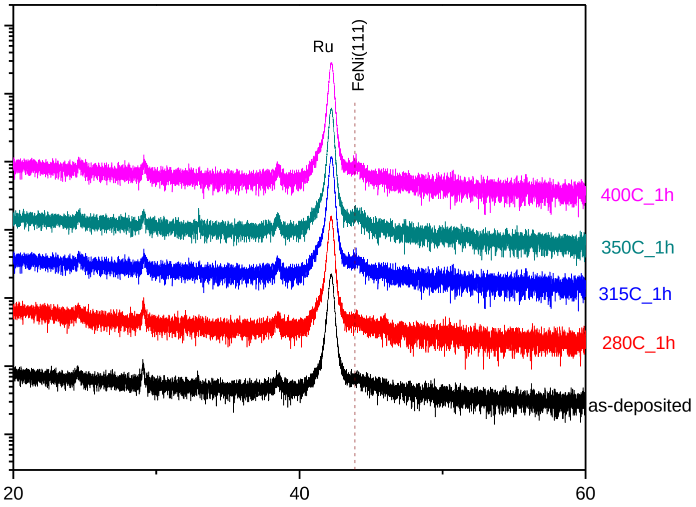

Fig 5. 24 XRD patterns for Fe51Ni49 before and after annealing at different temperatures

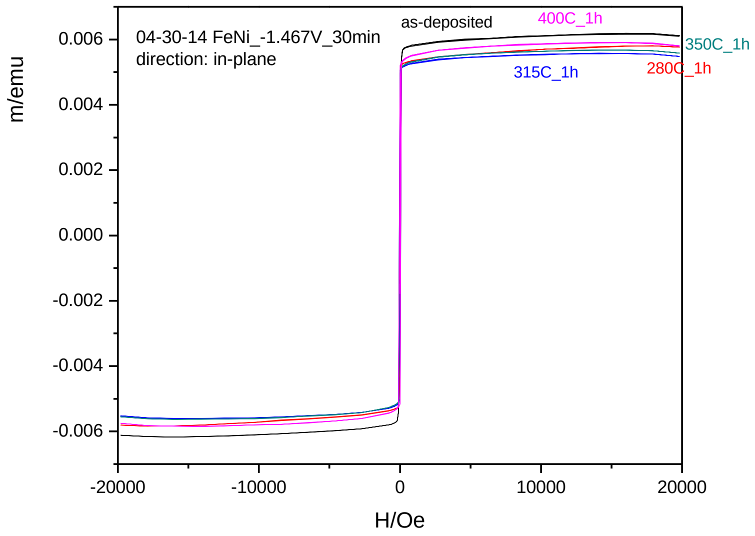

Fig 5. 25 In-plane magnetization curves before and after annealing.

The in-plane magnetization loops of as-deposited and 280^{o}C, 315^{o}C, 350^{o}C and 400^{o}C annealed $Fe_{47}Ni_{53}$ are shown in **Fig 5.27**. Both the in-plane and out-of-plane (**Fig 5.28**) magnetization decreased after annealing at 280^{o}C for 1h; in contrast, M_s increased after annealing at 350^{o}C and 400^{o}C for 1h, suggesting grain coarsening.

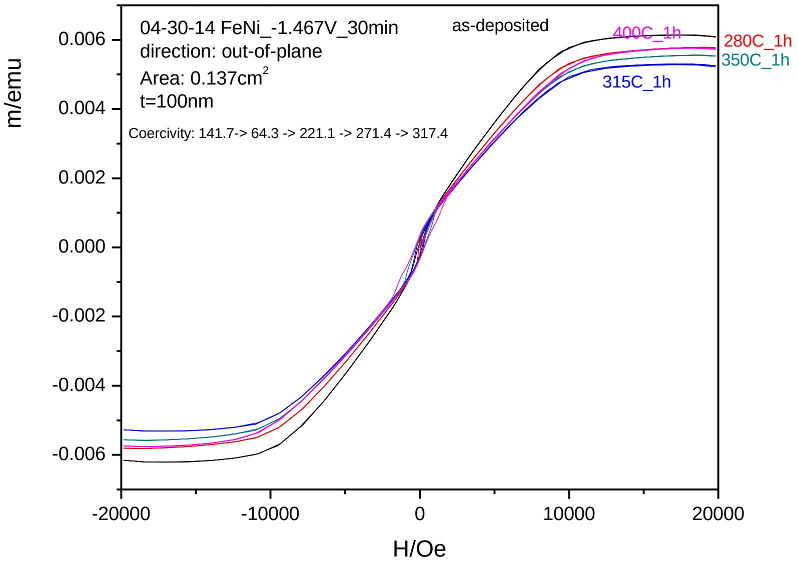

Fig 5. 26 Out-of-plane magnetization curves before and after annealing.

6. Conclusions

Significant magnetic hardening in FePt nanodot (150nm diameter) arrays was observed upon 550^{o}C annealing in the forming gas for 1h, and the volume of hard magnetic phase continued to grow with heat treatment at higher temperatures. Deposition conditions were explored and optimized based on a series of electrodeposited patterned samples, showing that a short deposition time of 10 min resulted in a FePt patterned sample with a thickness of around 30nm, which later exhibit a coercivity exceeding 8 kOe after 650^{o}C annealing for 1h. Uniformity of well-isolated nanodot arrays was examined and verified in AFM, SEM, and EDS mapping, with clear evidence that annealing process would not yield to delamination but result in a deviation from a cylindrical shape, due to the tendency for surface area minimization.

Electrolytes to generate $Fe_{50-x}Ni_xPt_{50}$ films with a wide range of Ni content ($0<x<30$) were selected after extensive experiments to determine the composition dependence on applied potential from solutions with varying metal ion concentrations. Anomalous codeposition was found during electrodeposition of FeNiPt thin film materials. For $Fe_{50-x}Ni_xPt_{50}$ ($18<x<30$) thin films with the thickness of 10nm, magnetization and coercivity were found to decrease with the increase of Ni content. Studies in $Fe_{50-x}Ni_xPt_{50}$ ($7<x<13$) thin films indicate that adding Ni to ordered FePt intermetallic compound results in a decrease in coercivity; when Ni content is fixed, a higher Fe/Pt ratio yields higher coercivity; the annealing temperature is optimized to be 700^{o}C, yielding a coercivity as high as 7.6 kOe, which is doubled compared to heat treatment at 650^{o}C for

1h. Temperature dependence of coercivity and normalized magnetization for FeNiPt films annealed at 700°C was studied, which clearly showed a steady coercivity drop from 100K to 300K while the decrease in magnetization is relatively small, suitable for HAMR application.

Electrodeposition from an alkaline solution was used for the first time to achieve permalloy and Pt doped permalloy. A horizontal three-electrode configuration was adopted instead of the usual vertical geometry, with the composition variance across the Pt doped permalloy reduced from around 30% to 7% or less. High Mr/Ms ratios (>0.92) were observed in in-plane magnetization curves and relatively low coercivity (<10 Oe) was obtained. Heat treatment at moderate temperature is proposed to relieve stress in these films, further decreasing the coercivity, with a goal of achieving a value less than 1Oe. Equiatomic FeNi was generated from the same solution used to produce permalloy. A relative large coercivity (~680 Oe) was found in annealed FeNi films with a thickness around 100nm; in thicker films without heat treatment (~500nm), coercivity up to 1kOe was obtained. From XRD patterns, a peak around 43.8° was associated with the relatively large coercivity, suggesting that partial ordering may have occurred. This important finding needs further examination and verification.

References

[1] V. Sivaprakasam, *Engineering Chemistry*, 2007, Laxmi Publications (P) LTD.

[2] Metrohm Autolab, “Basic overview of the working principle of a potentiostat/galvanostat (PGSTAT)”

[3] Y. Gamburg, G. Zangari, *Theory and Practice of Metal Electrodeposition*, 2011, Springer

[4] P. Marcus, *Corrosion Mechanisms in Theory and Practice*, 2011, CRD Press

[5] N. Kanani, *Electroplating – Basic Principles, Processes and Practise*, 2005, Elsevier Science

[6] http://guweb2.gonzaga.edu/faculty/cronk/biochem/W-index.cfm?definition=water

[7] K. M. Jeerage, D. T. Schwartz, The Electrochemical Society Interface, 2004, vol. 13, pp. 23-24

[8] M. Schlesinger, M. Paunovic, *Modern Electroplating (5th edition)*, 2010, John Wiley & Sons, Inc.

[9] S. Ichihara, M. Uedu and T. Den, IEEE Transactions on Magnetics, 2005, vol. 41, 3349

[10] L. Barbosa, G. Finazzi, P. Tulio, I. Carlos, J. Appl. Electrochem, 2008, vol. 38, pp. 115-125

[11] V. Kuznetsov, K. Golyanin, T. Pshenichkina, B. Lyakhov, S. Lyashenko, Mendeleev Commun, 2013, vol. 23, pp. 331-333

[12] S. Cherevko, J. Fu, K. Song, C. Chung, Korean J. Chem, Eng., 2009, vol. 26, pp. 1766-1769

[13] D. Liang, J. J. Mallett, G. Zangari, J. Electrochem. Soc, 2011, vol. 158, pp. 148-157

[14] Diamagnetism: http://www.irm.umn.edu/hg2m/hg2m_b/hg2m_b.html

[15] http://hydrogen.physik.uni-wuppertal.de/hyperphysics/hyperphysics/hbase/solids/hyst.html

[16] B. D. Cullity, C. D. Graham, *Introduction to Magnetic Materials*, 2009, IEEE Press

[17] http://www.ncnr.nist.gov/instruments/dcs/dcs_pdf_files/WERBcheatsheet.pdf

[18] Wikipedia: http://en.wikipedia.org/wiki/Valdemar_Poulsen

[19] J. M. D. Coey, *Magnetism and magnetic materials*, 2010, Cambridge University Press

[20] S. X. Wang, A. M. Taratorin, *Magnetic Information Storage Technology*, 1999, New York, Academic Press

[21] I. Mayergoyz, C. Tse, *Spin-stand Microscopy of Hard Disk Data*, 2007, Elsevier

[22] R. M. White, Magnetic recording - Pushing back the superparamagnetic barrier, Journal of Magnetism and Magnetic Materials, 2001, vol. 226-230, pp. 2042-2045

[23] M. Watanabe, M. Homma, Jpn. J. Appl. Phys., 1996, vol.35, pp. L1264

[24] Alexander Taratorin, *Magnetic Recording Systems and Measurements*, Chapter 6, 2004, Guzik Technical Enterprises

[25] Hitachi Global Storage Technologies, 2005

[26] D. Weller, A. Moser, L. Folks, M. E, L. Wen, M. F. Toney, M. Schwickert, J-U. Thiele, M. F. Doerner, IEEE Trans. Magn.,2000, vol. 36, pp. 10-15

[27] R. E. Rottmayer, S. Batra, D. Buechel, W. A. Challener, J. Hohlfeld, Y. Kubota, L. Li, L. Bin, C. Mihalcea, K. Mountfield, K. Pelhos, C. Peng, T. Rausch, M. A. Seigler, D. Weller, X. M. Yang, 2006, vol. 42, PP. 2417

[28] Edward Neville Da Costa Andrade: Endeavour, 1958, vol. 17, pp. 65; republished in R. J. Parket and R. J. Studder, *Permanent Magnets and Their Application*, Wiley, New York, NY, 1962.

[29] J.M.D. Coey: Endeavor, 1995, vol. 19, pp. 146–51.

[30] K. J. Strnat: Proc. IEEE, 1990, vol. 78, pp. 923 - 946

[31] J. Went, G.W. Rathenau, E.W. Gorter, and G.W. van Oosterhout: Philips Tech. Rev., 1952, vol. 13, pp. 194–208.

[32] M. H. Walmer, J. F. Liu, P. C. Dent: Proceedings of 20th International Workshop on rare earth permanent magnets and their applications, Crete, Greece, Sep. 8-10, 2008

[33] R. W. McCallum, L. H. Lewis, R. Skomski, M. J. Kramer, I. E. Anderson: Annu. Rev. Mater. Res, 2014, vol. 44, pp. 451-457

[34] UCDavis Chemwiki, “Powder X-ray Diffraction”

[35] Wikipedia, “Vibrating Sample Magnetometer”

[36] Bob Hafner, “Scanning Electron Microscopy Primer”

[37] Susan Swapp, University of Wyoming, Scanning Electron Microscopy (SEM)

[38] http://comp.uark.edu/~jchakhal/afm-draw-1-c-1.jpg

[39] J. K. W. Yang, Y. Chen, T. Huang, H. Duan, N. Thiyagarajah, H. K. Hui, S. H. Leong, V. Ng, Nanotechnology, 2011, vol. 22, 385301

[40] E. A. Dobisz, Z.Z. Bandic, T. Wu, T. Albrecht, Proceedings of the IEEE, 2008, Vol. 96, pp. 1836-1846

[41] B. D. Terris, J. Magn. Magn. Mater., 2009, vol. 321, pp. 512-517

[42] S. J. Greaves, H. Muraoka, Y. Kanai, J. Magn. Magn. Mater, 2012, vol. 324, pp. 314-320

[43] C. A. Ross, Annu. Rev. Mater. Res., 2001, vol. 31, pp. 203-235

[44] C. A. Ross, H. I. Smith, T. Savas, M. Schattenburg, M. Farhoud, M. Hwang, M. Walsh, M. C. Abraham, R. J. Ram, J. Vac. Sci. Technol. B, 1999, vol. 17, pp. 3168-3176

[45] M. Farhoud, M. Hwang, H. I. Smith, M. L. Schattenburg, J. M. Bae, K. Y. Toumi, C. A. Ross, IEEE Trans. On Magn., 1998, vol. 34, pp. 1087-1089

[46] D. Weller, J.E.E Baglin, A. J. Kellock, K. A. Hannibal, M. F. Toney, G. Kusinski, S. Lang, L. Folks, M. E. Best, B. D. Terris, J. Appl. Phys., 2000, vol. 87, pp. 5768-5770

[47] G. Hu, T. Thomson, M. Albrecht, M. E. Best, B. D. Terris, C. T. Rettner, S. Raoux, G. M. McClelland, M. W. Hart, J. Appl. Phys., 2004, vol. 95, pp. 7013-7015

[48] T. Aoyama, S. Okawa, K. Hattori, H. Hatate, Y. Wada, K. Uchiyama, T. Kagotani, H. Nishio, I. Sato, J. Magn. Magn. Mater, 2001, vol. 235, pp. 174-178

[49] D. H. Ping, M. Ohnuma, K. Hono, M. Watanabe, T. Iwasa, T. Masumoto, J. Appl. Phys., 2001, vol. 90, pp. 4708-4716

[50] C. T. Rettner, S. Anders, T. Thomson, M. Albrecht, Y. Ikeda, M. E. Best, B. D. Terris, IEEE Trans Magn., 2002, vol. 38, pp. 1725-1730

[51] JEE. Baglin, AJ Kellock, BD Terris, DK Weller, US 6331364 B1

[52] Binary Allloy Phase Diagrams, 2nd ed., edited by T. B. Massalski, H. Okamoto, P. R. Subramanian, and L. Kacprzak. ASM International, Materials Park, OH, 1990.

[53] B. Yao, "[Fe/Pt]n multilayer thin film reactions to form $L1_0$ FePt and exchange spring magnetis"

[54] D. Goll, T. Bublat, Phys. Status Solidi A, 2013, vol. 210, pp. 1261-1271

[55] G. Varvaro, S. Laureti, D. Fiorani, J. Magn. Magn. Mater., 2014, vol. 368, pp. 415-420

[56] http://mint.ua.edu/2007/11/adding-ag-to-fept-nanoparticles-lowers-the-temperature-for-l10-ordering/

[57] J. Tan, X. Qu, Q. Xie, Y. Zhou, G. Ru, Thin Solid Films, 2006, vol. 504, pp. 231-234

[58] C. Chen, J. Chen, J. Jeng, J. Electrochem. Soc., 2008, vol. 155, H1003-H1008

[59] T. N. Arunagitri, Y. Zhang, O. Chyan, M. El-Bouanani, M. J. Kim, K. H. Chen, C. T. Wu, L. C. Chen, Appl. Phys. Lett., 2005, vol. 86, 083104

[60] J. U. Thiele: “Heat Assisted Magnetic Recording (HAMR)”

[61] T. Rausch, J. D. Trantham, A. S. Chu, H. Dakroub, J. W. Riddering, C. P. Henry, J. D. Kiely, E. C. Gage, J. W. Dykes, IEEE Trans. Mag. 49 (2013) p.730

[62] A. Wu, Y. Kubota, T. Klemmer, T. Rausch, C. Peng, Y. Peng, D. Karns, X. Zhu, Y. Ding, E. Chang, Y. Zhao, H. Zhou, K. Gao, J.-U. Thiele, M. Siegler, G. Ju, E. Gage, IEEE Trans. Mag. 49 (2013) p. 779

[63] J. –U. Thiele, K. R. Coffey, M. F. Toney, J. A. Hedstrom, A. J. Kellock, J. Appl. Phys., 2002, vol. 91, pp. 6595-6600

[64] N. Li, B. Lairson, O. Kwon, J. Magn. Magn. Mater., 1999, vol. 205, pp. 1-6

[65] G. Stevens, M. Hatherly, J. Bowles, J. Mater. Sci., 1978, vol. 13, pp 499-504

[66] D. Berry, K. Barmak, J. Appl. Phys., 2007, vol. 102, 024912

[67] B. Wang, K. Barmak, J. Appl. Phys., 2011, vol. 109, 123916

[68] M. Yan, Y. Xu, X. Li, D. Sellmyer, J. Appl. Phys., 2005, vol. 97, 10H309

[69] H. Kim, E. J. Podlaha, 214th ECS meeting, Abstract #2598

[70] H. L. Seet, X. P. Li, J. B. Yi, W. Y. Ooi, K. S. Lee, J. Alloys. Compd., 2008, vol. 449, pp. 284-287

[71] N. N. Phuoe, W. T. Soh, G. Chai and C. K. Ong, Appl. Phys.,2013, vol. 113,073902

[72] H. J. Song, Z. H. Zhang, X. H. Men, Appl. Phys. A, 2008, vol. 91A, 73-76

[73] S. Sam, G. Fortas, A. Guittoum, N. Gabouze, S. Djebbar, Surf. Sci., 2007, vol. 601, pp. 4270-4273

[74] H. Yang, P. H. Pi, Z. Q. Cai, X. F. Wen, X. B. Wang, J. Cheng, Z. R. Yang, Appl. Surf. Sei. 2010, vol. 256, 4095-4102.

[75] B. Wu, M. Zhou, J. Li, X. Ye, G. Li, L. Cai, Appl. Surf. Sei., 2009, vol. 256, pp. 61-66

[76] S. D. Leith, S. Ramli, D. T. Schwartz, J. Electrochem. Soc., 1999, vol. 146, pp. 1431-1435

[77] L. H. Lewis, J. E. Shield, K. Barmak: US patent, 2014, Pub. no. US20140210581 A1

[78] T. Nagata: 13th Lunar and Planetary Science Conference, Houston, TX, March 15-19, 1982

[79] M. Kotsugi, H. Maruyama, N. Ishimatsu, N. Kawamura, M. Suzuki, M. Mizumaki, K. Osaka, T. Matsumoto, T. Ohkochi, T.Ohtsuki, T. Kojima, M. Mizuguchi, K. Takanashi, Y. Watanabe: J. Phys.: Condes. Matter, 2014, vol. 26, 064206

[80] T. Nagata, M. J. A., B. J. Carleton: Proc. Japan Acad., 1989, vol. 65, pp. 121-124

[81] L. Neel, J. Pauleve, R. Pauthenet, J. Laugier, D. Dautreppe,: J. Appl. Phys, 1964, vol. 35, pp. 873-876

[82] R. B. Scorzelli: Hyperfine Interact. 1997, vol. 110, pp. 143-150

[83] J. f. Petersen, M. Avdin, J. M. Knudsen: Phys. Lett. A, 1977, vol. 62, pp. 192-194

[84] E. R. D. Scott, R. S. Clarke Jr: Nature, 1980, vol. 287, pp. 255

[85] T. Nagata, M. Funaki, J. A. Danon: Mem. Natl. Inst. Polar Res, 1986, vol. 41, pp. 364-386

[86] T. Nagata, C. Kaito, Y. Saito, M. Funaki: Proc. Natl. Inst. Polar Res. Symp. Antarct. Meteorites, 1981, vol. 4, pp. 404-419

[87] T. Nagata, J. Danon, M. Funaki: Mem. Natl. Inst. Polar Res, 1987, vol. 46, pp. 263-282

[88] T. Nagata, M. Funaki: Mem. Natl. Inst. Polar Res., 1982, vol. 25, pp. 222-250

[89] A. Chamberod, J. Laugier, J. M. Penisson: J. Magn. Magn. Mater, 1979, vol. 10, pp. 139-144

[90] K. B. Reuter, D. B. Williams, J. I. Goldsten: Metall. Trans. A, 1989, vol. 20, pp. 719-725

[91] L. Amaral, R. B. Scorzelli, A. Paesano, M. E. Bruckman, A. B. Dominguez, T. Shinjo, T. Ono, N. Hosoito: Surf. Sci., 1997, vol. 389, pp. 103-108

[92] R. B. Scorzelli: Hyperfine Interact, 1997, vol. 110, pp. 143-150

[93] E. Lima Jr, V. Drago: Phys. Status Solidi. A, 2001, vol. 187, pp. 119-124

[94] T. Kojima, M. Ogiwara, M. Mizuguchi, M. Kotsugi, T. Koganezawa, T. Ohtsuki, T. Tashiro, K, Takanashi: J. Phys.: Condens. Matter, 2014, vol. 26, 064207(10pp)

[95] L. H. Lewis, F. Jimenez-Villacorta: Metall. Mater. Trans, 2013, vol. A44, pp. 2-20

[96]L. H. Lewis, F. E. Pinkerton, N. Bordeaux, A. Mubarok, E. Poirier, J. I. Goldstein, R. Skomski, K. Barmak: IEEE Magn. Lett., 2014, vol. 5, 5500104

[97] P. Manchanda, R. Skomski, N. Bordeaux, L. H. Lewis, A. Kashyap: J. Appl. Phys, 2014, vol. 115, no. 17A710

[98] G. Cacciamani, J. De Keyzer, R. Ferro, U. E. Klotz, J. Lacaze, P. Wollants: Intermetallics, 2006, vol. 14, pp. 1312-1325

[99] J. D. Keyzer, G. Cacciamani, N. Dupin, P. Wollants: Calphad, 2009, vol. 33, pp. 109-123

[100] P. L. Rossiter, R. A. Jago: Mat. Res. Soc. Symp. Proc., 1984, vol. 21, pp. 407-411

[101] C. W. Yang, D. B. Williams, J. I. Goldstein: J. Phase Equilib., 1996, vol. 17, pp. 522-531

[102] K. B. Reuter, D. B. Williams, J. I. Goldstein: Metall Trans A, 1989, vol. 20, pp. 719-725

[103] T. Ouchi, Y. Arikawa, T. Kuno, J. Mizuno, S. Shoji, T. Homma, IEEE Trans. Magn., 2010, vol. 46, pp. 2224-2227

[104] http://www.chem.ucla.edu/~bacher/CHEM174/equipment/CV1.html

[105] K. R. Hebert, G. E. Thompson, “Proceedings of the 7th International Symposium on Oxide Films on Metals and Alloys”, 1994

[106] G. Brauer, Handbook of Preparative Inorganic Chemistry, 1965, Academic Press New York, London

[107] R. Gupta, R. Medwal, N. Sehdev, S. Annapoorni, J. Magn. Magn. Mater., 2013, vol. 345, pp. 60-64

[108] C. P. Luo, D. J. Sellmyer, Appl. Phys. Lett., 1999, vol. 75, pp. 3162-3164

[109] M. Watanable, T. Masumoto, D. H. Ping, K. Hono, Appl. Phys. Lett, 2000, vol. 76, pp. 3971-3973

[110] R. F. C. Farrow, D. Weller, R. F. Marks, M. F. Toney, A. Cebollada, J. Appl. Phys., 1996, vol. 79, pp. 5967-5969

[111] M. Ghidini, G. Zangari, I. L. Prejbeanu, G. Pattanaik, L. D. Buda-Prejbeanu., J. Appl. Phys., 2006, vol. 100, pp. 103911-1~103911-10

[112] M. Ghidini, G. Zangari, I.L. Prejbeanu, G. Pattanaik, L. D. Buda-Prejbeanu et al., J. Appl. Phys., 2006, vol. 100, pp. 103911

[113] B. C. Dodrill, Lake Shore Cryotronics, Inc. "Low moment measurements with a Vibrating Sample Magnetometer"

http://www.lakeshore.com/Documents/Low%20Moment%20Measurements%20With%20a%20VSM.pdf

[114] A. Sun, P. C. Kuo, J. H, H. L. Huang, J. Sun, J. Appl. Phys., 2005, vol. 98, pp. 076109-1~3

[115] R. A. Ristau, K. Barmak, L. H. Lewis, K. R. Coffey, J. K. Howard, J. Appl. Phys., 1999, vol. 86, 4527

[116] D. Liang, J. J. Mallett, G. Zangari, Electochimica Acta, 2010, vol. 55, pp. 8100-8104

[117] D. Liang; J. J. Mallett; G. Zangari; *218th ECS meeting.* **2010**

[118] X. Liu, G. Zangari, J. Appl. Phys., 2001, vol. 90, pp. 5247-5252

[119] X. Liu, G. Zangari, J. Appl. Phys., 2001, vol. 90, pp. 5247-5252

[120] A. Cebollada, D. Weller, J. Sticht, G. R. Harp, R. F. C. Farrow, R. F. Marks, R. Savoy, J. C. Scott, Phys. Rev. B, 1994, vol. 50, pp. 3419

[121] Y. K. Takahashi, M. Ohnuma, K. Hono, J. Magn. Magn. Mater., 2002, vol. 246, pp. 259-265

[122] Y. Tamada, S. Yamamoto, M. Takano, S. Nasu, T. Ono, Appl. Phys. Lett., 2007, vol. 90, 162509

[123] Y. Liu, D. J. Sellmyer, D. Shindo, Handbook of Advanced Magnetic Materials: vol 1. Nanostructural Effect

[124] J. S. Chen, B. C. Lim, J. F. Hu, B. Liu, G. M. Chow, G. Ju, Appl. Phys. Lett., 2007, vol. 91, 132506

[125] J. P. Liu, Y. Liu, C. P. Luo, Z. S. Shan, D. J. Sellmyer, J. Appl. Phys., 1997, vol. 81, pp. 5644-5646

[126] W. B. Mi, H. Liu, Z. Q. Li, P. Wu, E. Y. Jiang, H. L. Bai, Appl. Surface. Sci., 2006, vol. 252, pp. 8688-8694

[127] A. Brenner, Electrodeposition of Alloys, Vol. 1, Academic Press, New York, 1963, p. 77

[128] R.V. Shenoy, M. Datta, J. Electrochem. Soc., 1996, vol. 143, pp. 544– 549

[129] K. Kondo, K. Fukui, J. Electrochem Soc., 1998, vol. 145, pp. 840–844

[130] L. J. Gao, P. Ma, K. M. Novogradecz, P. R. Norton, J. Appl. Phys., 1997, vol. 81, pp. 7595-7599

[131] JCPDS-International Centre of Diffraction Data (1999), No. 04-008-8265